Summer 8-15-2018

Robust Engineering of Dynamic Structures in Complex Networks

Walter Botongo Bomela
Washington University in St. Louis

WASHINGTON UNIVERSITY IN ST. LOUIS

School of Engineering and Applied Science
Department of Electrical and Systems Engineering

Dissertation Examination Committee:
Jr-Shin Li, Chair
ShiNung Ching
Zachary Feinstein
István Z. Kiss
Shen Zeng
Anatoly Zlotnik

Robust Engineering of Dynamic Structures in Complex Networks

by
Walter Botongo Bomela

A dissertation presented to
The Graduate School
of Washington University in
partial fulfillment of the
requirements for the degree
of Doctor of Philosophy

August 2018
Saint Louis, Missouri

Contents

List of Tables

List of Figures

Acknowledgments

I would like to seize this opportunity to express my sincere gratitude to my advisor, Professor Jr-Shin Li, for his invaluable guidance and support during my studies at Washington University in St. Louis. I am also grateful to Dr. István Kiss for interesting projects and his insightful comments that have been inspirational for my work. A special thanks goes to Dr. Anatoly Zlotnik for his mentoring and many fruitful discussions. I would also like to thank the members of my dissertation defense committee, Dr. ShiNung Ching, Dr. Zachary Feinstein and Dr. Shen Zeng, for their time and expertise.

I also wish to express my appreciation towards Dr. Jonathan Bird for introducing me to exciting research while at UNC Charlotte that since then has increased my enthusiasm for research. In addition, I would like to thank my colleagues and collaborators Shuo Wang, Wei Zhang, Pierre Urisanga, Liang Wang, Dr. Raphael Nagao, and Dr. Michael Sebek for many productive discussions.

Finally, I would like to express my gratitude to my family and my wife, who always provided me with their love, encouragement and support that made this work possible. Special thanks to the Chancellor's Graduate Fellowship program for their support over the course of my Ph.D. studies.

Walter Botongo Bomela

Washington University in Saint Louis
August 2018

Dedicated to my family.

ABSTRACT OF THE DISSERTATION

Robust Engineering of Dynamic Structures in Complex Networks

by

Walter Botongo Bomela

Doctor of Philosophy in Electrical Engineering

Washington University in St. Louis, August 2018

Research Advisor: Professor Jr-Shin Li

Populations of nearly identical dynamical systems are ubiquitous in natural and engineered systems, in which each unit plays a crucial role in determining the functioning of the ensemble. Robust and optimal control of such large collections of dynamical units remains a grand challenge, especially, when these units interact and form a complex network. Motivated by compelling practical problems in power systems, neural engineering and quantum control, where individual units often have to work in tandem to achieve a desired dynamic behavior, e.g., maintaining synchronization of generators in a power grid or conveying information in a neuronal network; in this dissertation, we focus on developing novel analytical tools and optimal control policies for large-scale ensembles and networks. To this end, we first formulate and solve an optimal tracking control problem for bilinear systems. We developed an iterative algorithm that synthesizes the optimal control input by solving a sequence of state-dependent differential equations that characterize the optimal solution. This iterative scheme is then extended to treat isolated population or networked systems. We demonstrate the robustness and versatility of the iterative control algorithm through diverse applications from different fields, involving nuclear magnetic resonance (NMR) spectroscopy and

imaging (MRI), electrochemistry, neuroscience, and neural engineering. For example, we design synchronization controls for optimal manipulation of spatiotemporal spike patterns in neuron ensembles. Such a task plays an important role in neural systems. Furthermore, we show that the formation of such spatiotemporal patterns is restricted when the network of neurons is only partially controllable. In neural circuitry, for instance, loss of controllability could imply loss of neural functions. In addition, we employ the phase reduction theory to leverage the development of novel control paradigms for cyclic deferrable loads, e.g., air conditioners, that are used to support grid stability through demand response (DR) programs. More importantly, we introduce novel theoretical tools for evaluating DR capacity and bandwidth. We also study pinning control of complex networks, where we establish a control-theoretic approach to identifying the most influential nodes in both undirected and directed complex networks. Such pinning strategies have extensive practical implications, e.g., identifying the most *influential spreaders* in epidemic and social networks, and lead to the discovery of degenerate networks, where the most influential node relocates depending on the coupling strength. This phenomenon had not been discovered until our recent study.

Chapter 1

Introduction

Naturally occurring biological, chemical, physical and also engineered systems exhibit a rich variety of complex dynamical behaviors that have always attracted the attention of the scientific community. The study of these systems helps us better understand how they work, and thus leads to the development of the technology that allow us to manipulate their dynamics as desired. For example, the understanding of how the auditory system processes sound has led to the development of the cochlear implants that partially restore hearing via direct electrical stimulation of spiral ganglion neurons [1, 2]; however, the spectral coding is limited by the spread of excitation from each electrode [1]. Inherent uncertainty of the physical systems and parameters dispersion, therefore, call for the development of robust control methodologies for the manipulation of complex ensemble systems that are often under-actuated, and in which feedback control laws are impractical or restricted due to the lack of access to the system internal states.

In this dissertation, we study control problems involving ensemble of interacting and non-interacting dynamical systems that are structurally identical, but with dispersion in their parameters. Furthermore, we consider collections of dynamical systems that are controlled by a common input signal (broadcast control), and those that are controlled by a single control directly applied on a small number of systems and whose effect propagates through the interactions between systems (pinning

control). This work is motivated by problems that naturally arise when manipulating ensembles of dynamical systems, e.g., nuclear spins in nuclear magnetic resonance (NMR) spectroscopy and imaging, neural networks, and even thermostatically controlled loads (TCLs) for demand response (DR) applications. In order to fulfill the expectations and needs of scientists and engineers dealing with these types of control problems, novel analytical methods, mathematical modeling and robust control-theoretic approaches are needed. This introductory chapter reviews the motivating applications, basic mathematical modeling and control approaches for the type of systems considered herein.

1.1 Iterative Control of Bilinear Systems

Bilinear systems represent a class of mathematical models that describe nonlinear physical systems more accurately than linear systems [3, 4]. With physical relevance in various scientific fields such as biology, socioeconomics, and engineering; bilinear systems are used to model various processes including chemical reaction, nuclear reaction, fluid dynamics [5, 3], and quantum systems [6, 7, 8, 9]. The conventional form of a deterministic bilinear system in state-space is given by

$$\frac{dx}{dt} = Ax + \sum_{j=1}^{m} u_j B_j x + \bar{B}u, \tag{1.1}$$

where $x \in \mathbb{R}^n$, $u \in \mathbb{R}^m$, A, $\bar{B}$, and B_j, with $j = 1, \cdots, m$, are matrices with appropriate dimensions. In some cases, the control input can be constrained, e.g., $|u(t)| \leq U_{\max}$, where $U_{\max}$ is the maximum allowable control amplitude.

Pioneering research on bilinear systems, initially supported by the Atomic Energy Commission (AEC) (currently the Department of Energy (DOE)) at Los Alamos, emerged from their natural

occurrence in nuclear reactor dynamics in which, open-loop processes for nuclear fission, poison buildup, heat transfer, and fluid dynamics are either bilinear or nearly bilinear [4, 3]. Since then, many research groups have studied the properties of this class of systems [10, 11], e.g., their controllability [12, 13], and various control procedures for manipulating the dynamics of bilinear systems have been proposed [14, 15, 5, 16, 8].

1.1.1 Literature Review of Iterative Control Methods

Optimal control problems for bilinear systems have been extensively studied over the past few decades, which led to the development of various control methodologies based on approximating procedures [15], direct solutions to the Hamilton-Jacobi-Bellman (HJB) equation [14] and iterative methods based on the solution of the Pontryangin's maximum principle [17, 18, 19, 20]. All of these control procedures found in the literature differ from one another based on how the optimal control problems are formulated and solved. For example, the finite and infinite-horizon free-endpoint optimal control problems for bilinear systems in [15] were solved iteratively by considering a sequence of linear problems that are then shown to uniformly converge to the desired solution, which agreed with a direct solution to the Hamilton-Jacobi (HJ) equation. Similar to the work presented in [15], with the main difference being the derivation of the optimal control law based on the Pontryangin's maximum principle, which led to coupled nonlinear equations, while the iterative procedure in [17] required a change of variables in order to stay in close proximity of the Riccati approach. This method increased the implementation complexity of the iterative procedure as the plant and the penalty matrices became state-dependent. However, this iterative procedure was shown to converge to a fixed point. Similar works were done in [18, 19, 20].

Methods for synthesizing suboptimal controls have also been treated. For example, one approach is to obtain the suboptimal control law based on the linear quadratic regulator (LQR) involving the steady-state solution of the state-dependent Riccati equation (SDRE) [21]. Similarly, a suboptimal solution to the bilinear quadratic regulator was studied in [5], where the proposed control law was based on the steady-state solution of the SDRE. The presented power series approach of the Riccati equation resulted in offline calculations of one Riccati equation and a sequence of Lyapunov equations. The work in [22] presented a method for synthesizing suboptimal feedback control laws for nonlinear systems. The proposed method allowed easy calculations of a second order approximation of the optimal control by obtaining approximate solutions to the HJB equation. Extending the work of [18] on optimal regulator of control-affine nonlinear systems, techniques for solving nonlinear-nonquadratic optimal tracking control problems were also developed [23]. It was shown that under mild conditions on each operator being locally Lipschitz, the method converged in the limit to the nonlinear system considered; however, a proof or conditions under which the converged solution will indeed be the optimal one was not provided.

1.1.2 Control of Bilinear Ensemble Systems

The control of a large number of structurally similar bilinear systems is of particular important in practical applications, e.g., NMR spectroscopy and imaging. This class of problems falls under a challenging area in mathematical control theory called *ensemble control* [6], which is concerned with the manipulation of the dynamics of a large collection of structurally identical systems indexed by a parameter set, and controlled by a common open-loop input signal [24, 8, 9]. Ensemble systems are described by a parametrized dynamical system of the form

$$\frac{d}{dt}x(t,s) = F(t,s,x(t,s),u(t)), \qquad x(0,s) = x_0(s), \tag{1.2}$$

where $x(t) \in \mathbb{R}^n$, $u(t) \in \mathbb{R}^m$, $s \in \mathcal{D} \subset \mathbb{R}^d$, with F and $x_0(s)$ smooth functions of their respective arguments [25]. The states of such an inhomogeneous population of dynamical systems (1.2) can be steered from an initial distribution $x(0,s)$, to a desired final distribution $x(T,s)$, over the corresponding function space, only if (1.2) is ensemble controllable.

Definition 1 (Ensemble controllability [6])**:** The family of dynamical systems (1.2) is said to be ensemble controllable on the function space $F(\mathcal{D})$ defined on some compact set $\mathcal{D} \subset \mathbb{R}^d$, if there exists a control $u(t)$ and a time $T > 0$ such that starting from any initial state $x(0,s)$, the system can be steered to within a ball of radius ε around the target state $g(s) \in F(\mathcal{D})$, i.e., $\|x(T,s) - g(s)\| < \varepsilon$. Here $\|\cdot\|$ denotes a desired norm, say L_2 norm, on $F(\mathcal{D})$.

It is important to note that ensemble controllability is defined in an approximate sense and that the final time T may depend on ε, in other words, the desired accuracy. The controllability of ensemble systems can be evaluated by computing the iterated Lie bracket [26, 27, 6].

1.2 Control of Large-Scale Rhythmic Systems

Large-scale rhythmic systems are ubiquitous in biology, physics and engineering. These systems often composed of ensembles of either interacting or non-interacting nonlinear oscillating units require a certain optimal organization of their dynamic structures for normal operation. The electrical power grid is a good example of a large-scale engineered system in which synchronization of generators is required for normal operation [28, 29, 30]. Various other examples of synchronization can be found in biological systems, e.g., metabolic synchronization of glycolytic in yeast cells [31, 32]. While synchronized dynamic structures might be required in some systems, in others, it is to be avoided for normal operation to be maintained. This is the case in control of TCLs ensembles

used to provide ancillary services in demand response programs [33, 34, 35]. Large-scale systems can be affected by external stimuli which can perturb their dynamic behaviors, with sometimes unintended consequences, e.g., cascading failures in the power grid [36, 37] or perturbation of information processing by neural networks [38, 39, 40]. These systems are more or less sensitive to external disturbances depending on the underlying network structure. However, it is often possible re-establish normal operation using an external control signal that has been carefully designed, e.g., narrow pulses in deep brain stimulation (DBS) [41, 42].

1.2.1 Engineering Spatiotemporal Patterns in Oscillator Ensembles

A wide variety of biological and engineered rhythmic systems rely on the internal oscillators following a given pattern of activities that is essential for these systems to perform their intended functions. Synchronization and desynchronization are certainly two of the most studied properties of oscillatory systems in physics, biology, neuroscience and engineering [43, 44, 45, 46]. Furthermore, some pathologies such as Parkinson's disease and epilepsy are linked to an excessive synchronization of neural activities [47, 48], however, the symptoms in most cases can be alleviated by high frequency stimulation of the ventral intermediate nucleus and stimulation of the vagus nerve [48, 49] that desynchronizes the neurons. Although synchronization is not desirable in these pathologies, it is however a desired property in other applications such as synchronization of the pacemaker in the heart [44, 50], suppression of jet-lag by re-synchronizing the circadian rhythm [51] and stability of the power grid [28, 30].

For decades, scientists have been investigating how the central nervous system (brain) interprets or processes information perceived from the environment through sense organs. There is sufficient evidence indicating that stimulus information is encoded in neural networks as spatiotemporal

spiking patterns, furthermore, it has been shown that all information about the spike pattern is lost if only mean firing rates (temporal) or ensemble activities (spatial average) are considered [52]. In animals, e.g., rats, it has been observed that the hippocampus uses timing in the spike activity of place cells, in addition to rate, to encode location in space [53]. Moreover, phase code (timing of a neuron spikes relative to the phase of the inhibitory theta rhythm) is used by the place cells to convey information [53, 54].

Understanding of how the brain processes information, while using so little energy, will have a tremendous impact on medical and engineering applications. For example, this could enable the improvement of neuro-inspired devices such as the IBM's TrueNorth [55] and the Intel's Loihi [56] neuromorphic chips, which are spiking neural networks tailored toward cognitive tasks such as patterns classification and objects recognition [57]. Thus far, there has been some success in bioengineering applications, for instance, the cochlear implant, a microelectrode array that directly stimulates the auditory nerve in patients with profound deafness, and hence restoring audition [2]. Though restoration of audition has been effective in most cases, the restoration of vision is a more complex task. Despite recent promising advances made in electrical retinal implants that have been tested in animal experiments, there are still several hurdles to overcome before testing on human subjects can be successfully undertaken [58]. In that regard, efforts have been made to develop a model for the mammalian retina [59] from which a silicon chip has been fabricated [60]. This is the first silicon retina to approach the spatial density of the retina, and that successfully models the inner retina circuitry. In light of the new advances in neuromorphic chips and computing, one can see that we are approaching fully integrated neuro-inspired systems with sensors that can perceive the outside world and encode the information into spatiotemporal spike patterns that can directly be used by neurocomputers for analysis or be interpreted by the central nervous system in humans.

What role can control theory play in the development of neuro-inspired devices and computing? This question is addressed in Chapter 3 where some key answers are provided. It is estimated that 130 million photo-receptors in the retina capture visual information that is then compressed into electrical signals carried by 1.2 million ganglion neurons, whose axons form the optic nerve [58]. This information is transmitted to the visual cortex of the brain in the form of spatiotemporal stimulation patterns of electrical impulses that can be interpreted by the brain. However, this transfer of visual information requires the stimulation of a large ensemble of sensory neurons simultaneously, and in the correct sequence to enable accurate encoding of three-dimensional objects [58]. This presents a challenge for retinal implants given that numerous electrodes are required for an accurate transmission of visual information to the visual cortex. Therefore, the development of control algorithms for manipulating spatiotemporal spike patterns of a large collection of neuron oscillators with a common (minimum energy) control signal is needed. This will enable accurate transfer of information from an implant with a relatively small number of required electrodes.

The control of either a single or an ensemble of neuron oscillators has been the focus of many research groups, which led to the development of various control techniques such as the charge-balanced and minimum-power controls that manipulate the spiking time of a neuron [61, 62]. Concurrently, others have developed methods for designing control waveforms for asymptotic entrainment of neural oscillators to a desired frequency [63, 64, 65, 66], or for phase assignment [67] as well as design of control inputs to desynchronize networks of coupled neurons [68]. The general problem of selective spiking of neurons, where a stimulus is used to induce firing of one neuron while inhibiting the rest of the population has also been considered [69]. Most control algorithms and techniques, thus far, tackle individual control objectives such as synchronization [49], desynchronization [70] or entrainment [71].

1.2.2 Control of Cyclic Loads for Demand Response Applications

In recent years, considerable efforts have been made to reduce the carbon footprint of fossil-fueled generators. In the United States, many states have been adopting or increasing their renewable energy generation portfolio standards [72]. However, the increasing penetration of renewable energy sources (RESs) and their intermittent generation affects power quality on electric distribution systems and complicates load balancing in power systems [73]. The development of new approaches to regulate the inherently fluctuating and uncontrollable power outputs of RESs [74, 75], is of the foremost importance in order to maintain grid stability.

Demand response (DR) programs enable electricity users to adjust their consumption in response to energy prices or incentive payments [76, 77], and thus provide significant capability to balance supply and demand on the power grid. However, the response to market price fluctuations of this approach is slow. Meanwhile, aggregated TCLs can be controlled to react faster to changes, and this flexibility can be used to provide balancing services in real-time retail electricity markets [76]. TCLs such as heating ventilation and cooling (HVAC) systems and electric water heaters have been shown to be suitable for providing ancillary services to the grid [78, 79], in addition, field experiments were conducted to demonstrate the ability of TCLs (refrigerators) to provide ancillary services [80, 33]. Furthermore, domestic refrigerators were used to quantify the flexibility of household TCLs, as well as the computational resource constraints on the control of large TCL populations. Certainly, one of the simplest way to control TCLs is to turn them off/on as needed. For example, the frequency controller in [80] switches the TCLs off one by one based on the ability of each refrigerator to stay off longer, while in [33] a delay is introduced to improve the controller performance and reduce power overshoots. It was then noted that abruptly withdrawing a large number of loads produced instability and caused the loads to synchronize their duty cycles.

The synchronization of TCLs, due to the control action, creates power fluctuations and limits the capacity of ancillary services (AS) that can be provided. So, in an effort to further the understanding of the oscillatory behavior of the aggregate power consumption, the damping of oscillations was characterized as a function of parameter heterogeneity by exploiting the similarities that exist between a population of mass-springs systems and an ensemble of TCLs [81]. Concurrently, the dependence of the mixing rate of the population on the model parameters was characterized in [82]. In Chapter 4, we introduce a phase model representation of TCLs that can be used to evaluate AS capacity of a TCL population and develop novel control policies. Furthermore, the phase sensitivity functions of the phase models can be used to compute the regions of entrainment (Arnold tongues) to an external forcing signal [83, 84], which provide insights into the phenomenon of temporary synchronization (unwanted power oscillations).

Various control schemes for modulating the aggregate power of TCLs in response to a power regulation signal have been proposed [34, 85, 78, 86]. Hence, enabling the compensation of power fluctuations of RESs, e.g., solar panels, using TCLs [87]. However, control induced synchronization of TCLs remains a factor that limits the time scale and capacity of AS that they can provide. This inspired the research and development of control policies that aim to minimize unwanted power oscillation in response to pulse-like changes of the set-point temperature [88, 89]. The control protocol proposed in [88] reduces power overshoots by allowing the TCL to stay in its current state until the temperature hits one of the transition points, then starts following a new pair of deadband limits. On the other hand, [89] introduces a delay of M-minutes before changing the status of the TCL. The development of control policies that reduce such synchronization of TCLs is therefore of fundamental important.

1.2.3 Optimal Placement of Driver Nodes in Complex Networks

Complex systems constituted by a network of coupled nonlinear systems are prevalent in nature and human society. In normal operations, such a complex network has a spatiotemporal pattern optimized for its functioning. When the pattern breaks down, malfunctioning of devices or dynamical diseases can develop. Under these circumstances, a control policy –intervention on dynamic properties using exogenous inputs– can be applied to re-establish the functioning of the system. For large networks, the application of control inputs is often limited to a single or a small number of sites. A prominent intervention task is to stabilize the network behavior at a certain state, e.g, the equilibrium. This can be achieved by stabilizing a single site and then propagating the control effect through couplings between nodes to the entire network. This feedback control strategy is referred to as pinning control and is illustrated in Figrure 1.1. One compelling application of such a pinning control strategy is to suppress wild fluctuations in a network in order to retrieve normal stationary behavior. Prominent examples include the use of neurostimulation to mediate epileptic seizures [90, 39, 91], and the application of medication to the infected nodes in a high-risk contact network to preclude the spread of disease, such as HIV [92].

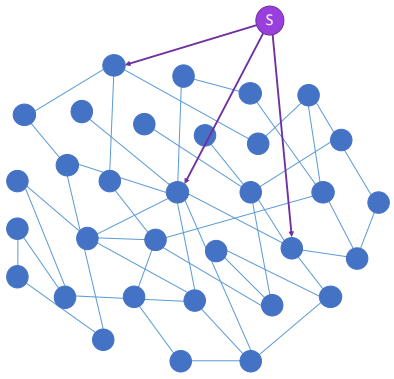

Figure 1.1: Illustration of pinning control. The virtual leader (also called *pinner*) is a virtual node S (the purple node) added to the network and which defines the desired trajectory.

Notions of pinning control, including pinning controllability [93] and effectiveness [94], have also been extensively introduced to analyze dynamic structures in a complex network, such as synchronization [95], stabilization [96] and consensus [97, 98]. A fundamental challenge of pinning control is to identify the most influential site for establishing stable behavior in the network and to unlock what this site is dependent upon. In Chapter 6, we address these problems by studying bidirectional networks consisting of n dynamical units and, without loss of generality, illustrate our findings through networks of Stuart-Landau (SL) oscillators, that are systems of identical dynamic units diffusively coupled, and in which each unit has an unstable fixed point.

1.3 Organization

The remainder of this dissertation is organized as follows. Chapter 2 formulates an optimal tracking control problem for bilinear systems, which is solved iteratively. A proof of convergence of the resulting algorithm and the necessary conditions for the existence of the optimal control are provided. Chapter 3 extends the iterative control algorithm, for bilinear systems presented in Chapter 2, to ensembles of limit-cycle oscillators by leveraging phase reduction theory. The controllability of oscillator networks, in particular neural networks, is also examined. The rest of the chapter is concerned with the control of phase model oscillators into forming complex spatiotemporal phase patterns. In Chapter 4, phase reduction theory is used to reduce thermostatically controlled loads to phase model representations that facilitate the analysis and control of TCL ensembles for demand response. Then in Chapter 5, using the phase model of the TCL developed in Chapter 4, an optimal control problem is formulated and solved using the Pontryagin's maximum principle. In Chapter 6, the pinning control problem of network of oscillators is examined. The conditions for stabilization of a network of oscillators are derived and a control-theoretic approach for identifying

the most influential control site is proposed. Furthermore, the dependence of the most influential control site on the network topology and size is also analyzed. Finally, the concluding remarks and future directions are given in Chapter 7.

Chapter 2

Iterative Control of Bilinear Systems

In this chapter, we develop an iterative method for synthesizing optimal controls for bilinear quadratic tracking problems. The developed control algorithm is easy to implement as the control law of the bilinear system is obtained iteratively by considering a sequence of linear systems. The minimizing control law is calculated iteratively by solving a set of coupled state-dependent differential equations derived from the Hamilton-Jacobi-Bellman equation. Furthermore, the proof of convergence of the iterative procedure is provided, and the convergence is demonstrated by numerical simulations for three example tracking problems.

To complete this chapter, we demonstrate the robustness and versatility of the control algorithm by applying it to relevant problems on open quantum systems that arise in NMR spectroscopy of proteins in liquids [99, 8]. Specifically, we consider coupled spin systems [100, 101, 7] and ensemble control of Bloch equations motivated by practical applications that arise in nuclear magnetic resonance (NMR) spectroscopy and imaging (MRI) [6, 7, 102, 9]. The basic Ideas of this chapter was published in [103].

2.1 Optimal Tracking of Bilinear Systems

Optimal control of bilinear systems has been the subject of investigations for at least six decades [3]. Since then, many control algorithms have been proposed for synthesizing optimal or suboptimal control with various objective functions being considered [5, 20, 14, 17, 15, 104]. In this chapter, we consider the optimal tracking problem for bilinear systems and solve for the optimal control iteratively. As we are going to show in the following, the versatility of the resulting control algorithm is a considerable advantage in the sense that one can easily use the same algorithm to solve for the free-endpoint, regulation and tracking problems.

2.1.1 Problem Formulation

Let us consider the tracking problem of the following time-varying bilinear system, assumed observable,

$$\begin{aligned} \dot{x}(t) &= A(t)x(t) + B(x)u(t), \\ y(t) &= C(t)x(t), \end{aligned} \tag{2.1}$$

where $x(t) \in \mathbb{R}^n$, $u(t) \in \mathbb{R}^m$, and $y(t) \in \mathbb{R}^r$. Let $z(t) \in \mathbb{R}^r$ be the desired output trajectory, and the various matrices $A(t)$, $B(t)$ and $C(t)$ be of appropriate dimensions. The input matrix $B(x) = \bar{B} + \sum_{j=1}^{n} x_j N_j$, with $\bar{B}$ and $\sum_{j=1}^{n} x_j N_j$ constant and state dependent matrices, respectively. The aim is to control the system (2.1) such that the output $y(t)$ tracks the desired trajectory $z(t)$ as close as possible in the time interval $[0, T]$ with minimum control effort. Let's define the error vector as

$$e(t) = z(t) - y(t), \tag{2.2}$$

and the performance index as

$$J(u) = \frac{1}{2}e'(T)Fe(T) + \frac{1}{2}\int_0^T e'(t)Q(t)e(t) + u'(t)R(t)u(t)dt, \tag{2.3}$$

where "$'$" denotes the transpose operation, T is specified and $x(T)$ free. In this way one is dealing with a free-final state problem. Moreover, $F \succeq 0$ and $Q(t) \succeq 0$ are $n \times n$ positive semidefinite matrices, and $R(t) \succ 0$ is $m \times m$ positive definite, $\forall t \in [0,T]$. Furthermore, it is assumed that the entries of the matrices A, B, C, Q, R are continuous functions over $[0,T]$.

2.1.2 Optimal Control Solution

Let $V(t,x)$ be the value function associated with the optimal control problem of the bilinear system in (2.1) with the cost functional $J(u)$ defined in (2.3), then $V(t,x) = \inf_{u \in \mathcal{U}_{(t,x)}} J(u)$ over all admissible controls $u : [0,T] \to \mathcal{U} \subseteq \mathbb{R}^m$. Furthermore, if V is differentiable with respect to (t,x), then by minimizing the Hamiltonian of the system over all admissible controls, one obtains the Hamilton-Jacobi-Bellman (HJB) equation [105, 106], given by

$$V_t + \min_{u \in \mathcal{U}} \left\{ V_x (Ax + B(x)u) + \frac{1}{2}(e'Qe + u'Ru) \right\} \equiv 0, \tag{2.4}$$

where $V_t = \frac{\partial V}{\partial t}$ and $V_x = \frac{\partial V}{\partial x}$. The necessary condition of optimality gives

$$u(t) = -R^{-1}B(x)'V_x'. \tag{2.5}$$

Substituting for $e(t)$ and $u(t)$ in (2.4) gives

$$V_t + \frac{1}{2}(V_xAx + x'A'V_x') - \frac{1}{2}V_xEV_x' + \frac{1}{2}(x'Dx) + \frac{1}{2}(z'Qz) - \frac{1}{2}(x'Wz + z'Wx) \equiv 0, \tag{2.6}$$

where $D(t) = C'(t)Q(t)C(t)$, $E(x) = B(x)R^{-1}(t)B'(x)$, and $W(t) = C'(t)Q(t)$. To emphasize the state dependence of the matrix E while, at the same time, simplifying the notations, we write $E(x)$ rather than $E(x(t))$.

Suppose that a candidate solution of (2.6) is of the form

$$V(t,x) = \frac{1}{2}x^{*\prime}P(t)x^* - x^{*\prime}g(t) + h(t), \tag{2.7}$$

where x^* is the optimal state trajectory, $P(t) \in \mathbb{R}^{n\times n}$, $g(t) \in \mathbb{R}^n$, and $h(t) \in \mathbb{R}$. Taking the partial derivatives of (2.7) with respect to x and t, one obtains

$$\begin{aligned} V_x &= P(t)x^* - g(t), \\ V_t &= \frac{1}{2}x^{*\prime}\dot{P}(t)x^* - x^{*\prime}\dot{g}(t) + \dot{h}(t). \end{aligned} \tag{2.8}$$

Substituting (2.8) into (2.6), and after some algebraic manipulations, yields

$$\frac{1}{2}x^{*\prime}\{\dot{P} + PA + A'P - PEP + D\}x^* + x^{*\prime}\{-\dot{g} - A'g + PEg - Wz\} + \dot{h} + \frac{1}{2}z'Qz - \frac{1}{2}gEg \equiv 0. \tag{2.9}$$

Since (2.9) must be satisfied for all $x^*(t)$, $z(t)$ and $t \in [0,T]$, one obtains the following set of coupled state-dependent equations that characterize the optimal solution of the tracking problem,

$$\dot{P}(t) = -P(t)A - A'P(t) + P(t)E(x)P(t) - D(t), \tag{2.10}$$

$$\dot{g}(t) = -\left[A' - P(t)E(x)\right]g(t) - W(t)z(t), \tag{2.11}$$

$$\dot{h}(t) = -\frac{1}{2}z'(t)Q(t)z(t) + \frac{1}{2}g'(t)E(x)g(t), \tag{2.12}$$

with boundary conditions, $P(T) = C'(T)FC(T)$, $g(T) = C'(T)Fz(T)$ and $h(T) = z'(T)Fz(T)$, respectively. In addition, the optimal feedback control law is of the form

$$u^*(t) = -R^{-1}B'(x^*)\left[P(t)x^*(t) - g(t)\right], \tag{2.13}$$

with the optimal trajectory given by

$$\dot{x}^*(t) = \left[A - E(x^*)P(t)\right]x^*(t) + E(x^*)g(t), \tag{2.14}$$

and the optimal cost is $J^* = J(u^*) = \frac{1}{2}x^{*\prime}(0)P(0,x(0))x^*(0) - x^*(0)g(0,x(0)) + h(0,x(0))$.

2.2 Iterative Algorithm and its Convergence

Computing the optimal solution, i.e., (u^*, x^*), for the tracking problem described in Section 2.1.2 requires solving a system of coupled equations (2.10)-(2.14), which, however, is in general analytically and numerically intractable. In this section, we introduce an iterative method to resolve the plight and, furthermore, show the convergence of the proposed iterative procedure converging to an optimal solution.

2.2.1 Iterative Algorithm for Optimal Bilinear Tracking Problems

Treating (2.10)-(2.14) as iteration equations (see Theorem 1) with $k \in \mathbb{N}$ denoting the iteration, u_k and x_k denoting the control and the trajectory obtained at the k^{th} iteration, respectively, the iterative method for the synthesis of optimal bilinear tracking control is described in the following algorithm.

Data: $A(t)$, $B(x)$, $C(t)$, $Q(t)$, $R(t)$, F, $x(t_0)$, $z(t)$, T
Initialization ;
$k = 0$;
$x_0(t) = z(t)$, $x_0(0) = z(0)$;
while $||x_k(t) - x_{k-1}(t)|| > \varepsilon$ **do**
    compute $P_k(t)$ and $g_k(t)$ using $B(x_k(t))$;
    $u_k(t) = -R^{-1}B'(x_k(t))[P_k(t)x_{k+1}(t) - g_k(t)]$;
    $\dot{x}_{k+1}(t) = Ax_{k+1}(t) + B(x_k(t))u_k(t)$;
    $k = k + 1$;
end

Algorithm 1: Algorithmic description of the iterative method.

2.2.2 Convergence of the Iterative Algorithm

In this section, we show that Algorithm 1 generates convergent sequences that converge uniformly to the optimal solution defined in (2.13) and (2.14), i.e., $x_k \to x^*$ and $u_k \to u^*$.

Theorem 1: Consider the iteration equations

$$\dot{P}_k(t) = -P_k(t)A - A'P_k(t) + P_k(t)E_k(x)P_k(t) - D(t), \tag{2.15}$$

$$\dot{g}_k(t) = -\left[A' - P_k(t)E_k(x)\right] g_k(t) - W(t)z(t), \tag{2.16}$$

$$u_k(t) = -R^{-1}B_k'(x)[P_k(t)x_{k+1}(t) - g_k(t)], \tag{2.17}$$

$$\dot{x}_{k+1}(t) = [A - E_k(x)P_k(t)]x_{k+1} + E_k(x)g_k(t), \tag{2.18}$$

with the boundary conditions $P_k(T) = C'(T)FC(T)$ and $g_k(T) = C'(T)Fz(T)$, where $E_k(x) = B(x_k)R^{-1}B'(x_k)$, $D(t) = C'(t)Q(t)C(t)$, and $C(t)$ and F are defined in (2.1) and (2.3), respectively. If $R(t) \succ 0$, $D(t) \succeq 0$ for all $t \in [0,T]$ and $F \succeq 0$, then the sequences $\{x_k\}$ and $\{u_k\}$ converge uniformly to x^* and u^* satisfying (2.14) and (2.13), respectively, with the initial condition $x_k(0) = \hat{x}(0)$.

Proof: By the variation of constants formula, the solution to (2.18) is given as

$$x_{k+1}(t) = \Phi_k(t,0)\hat{x}(0) + \int_0^t \Phi_k(t,\sigma)E_k(x(\sigma))g_k(\sigma)d\sigma, \tag{2.19}$$

where $\Phi_k(t,t_0)$ is the transition matrix for the homogeneous system $\dot{x}_{k+1} = [A - E_k(x)P_k(t)]x_{k+1}$. Let's now consider the difference $x_{k+1} - x_k$, which satisfies

$$\frac{d}{dt}[x_{k+1} - x_k] = [A - E_kP_k]x_{k+1} - [A - E_{k-1}P_{k-1}]x_k + E_kg_k - E_{k-1}g_{k-1}. \tag{2.20}$$

Adding and subtracting $[A - E_kP_k]x_k + E_{k-1}g_k$ to (2.20) yields

$$\begin{aligned}\frac{d}{dt}[x_{k+1} - x_k] = &[A - E_kP_k](x_{k+1} - x_k) + [E_{k-1}P_{k-1} - E_kP_k]x_k \\ &+ E_{k-1}(g_k - g_{k-1}) + [E_k - E_{k-1}]g_{k-1},\end{aligned} \tag{2.21}$$

and then we have the solution

$$\begin{aligned}x_{k+1} - x_k = \int_0^t \Phi_k(t,\sigma)\{&[E_{k-1}P_{k-1} - E_kP_k]x_k \\ &+ E_{k-1}(g_k - g_{k-1}) + [E_k - E_{k-1}]g_{k-1}\}(\sigma)d\sigma,\end{aligned} \tag{2.22}$$

since $x_{k+1}(0) - x_k(0) = 0$. It follows that

$$\|x_{k+1}(t) - x_k(t)\| \leq \int_0^t \left\{\beta_1\|E_k - E_{k-1}\| + \beta_2\|P_k - P_{k-1}\| + \beta_3\|g_k - g_{k-1}\|\right\}(\sigma)d\sigma, \tag{2.23}$$

where

$$\begin{aligned}\beta_1 &= \|\Phi_k(t,\sigma)\|\left(\|P_k\|\|x_k\| + \|g_{k-1}\|\right),\\ \beta_2 &= \|\Phi_k(t,\sigma)\|\|E_{k-1}\|\|x_k\|,\\ \beta_3 &= \|\Phi_k(t,\sigma)\|\|E_{k-1}\|,\end{aligned} \tag{2.24}$$

(see Appendix A) with the norm defined by $\|v(t)\| = \sup_{t\in[0,T]} \|v(t)\|$ in which $\|v\| = \max_i |v_i|$ for $v \in \mathbb{R}^n$ and $\|D\| = \max_{1\le j\le n} \sum_{i=1}^{n} |D_{ij}|$ for $D \in \mathbb{R}^{n\times n}$. Note that the conditions $R(t) \succ 0$, $D(t) \succeq 0$, and $F \succeq 0$ guarantee the boundedness of $\|P_k\|$ in β_1.

Now, let $\xi_k(t) \equiv \|x_{k+1}(t) - x_k(t)\|$, it can be shown that all the norms of the differences in (2.23) are bounded as follows (see Appendix A.0.2):

$$\begin{aligned}\|E_k(x) - E_{k-1}(x)\| &\le \alpha_1 \xi_{k-1}(t),\\ \|P_k(t) - P_{k-1}(t)\| &\le \alpha_2 \xi_{k-1}(t),\\ \|g_k(t) - g_{k-1}(t)\| &\le \alpha_3 \xi_{k-1}(t).\end{aligned} \tag{2.25}$$

Substituting the bounds in (2.25) into (2.23) yields $\xi_k(t) \le \int_0^t M\xi_{k-1}(\sigma)d\sigma$, where $M = \beta_1\alpha_1 + \beta_2\alpha_2 + \beta_3\alpha_3$. Since M can be chosen independently of the iteration index k, by recursion it follows that

$$\xi_k(t) \le M^k \int_0^t \int_0^{\sigma_1} \cdots \int_0^{\sigma_{k-1}} \xi_0(\sigma_k) d\sigma_k \cdots d\sigma_1. \tag{2.26}$$

Because $\xi_0(t)$ is bounded for all $t \in [0,T]$, one can choose the upper bound to be Γ, then (2.26) becomes

$$\xi_k(t) \le \frac{(MT)^k}{k!}\Gamma, \quad \forall t \in [0,T]. \tag{2.27}$$

Clearly, as $k \to \infty$, $\xi_k(t) \to 0$, which implies $\lim_{k\to\infty} \|x_{k+1}(t) - x_k(t)\| = 0$. Therefore, (2.18) becomes equivalent to (2.14), and the sequence $\{x_k\}$ converges uniformly to the solution $x^*(t)$. Consequently, given (2.17) and (2.13), $\{u_k\}$ converges to $u^*(t)$ as well. □

Note that the proof of convergence presented in this chapter has some similarities with the proof in [15], where the infinite-time regulator problem was dealt with. Herein, aside from dealing with the finite-time problem, it was required to show that the solution $P(t)$ to the Riccati equation (2.10) is bounded $\forall t \in [0,T]$ and the vector-valued function $g(t)$ introduced by the tracking command is bounded as well $\forall t \in [0,T]$.

2.2.3 Existence and Optimality of the Convergent Solution

In Section 2.2.2, we showed that the iterative algorithm will find a convergent solution, provided the solution to the system of ordinary differential equations (2.10)-(2.12) exists. In this section, we will construct the conditions under which the optimal solution for the tracking problem described in Section 2.1.1 exists and is a global optimal. The following theorem is essential to our construction.

Theorem 2: If there exists a solution $V(t,x)$ of class C^2 of the HJB equation, which satisfies the boundary condition $V(T,x) = \varphi(T,x)$, and if $L_{uu}(t,x,u) = \frac{\partial^2 L}{\partial u^2} \succ 0$ for all t,x,u, where $L = e'(t)Q(t)e(t) + u'(t)R(t)u(t)$ is the Lagrangian of the performance index in (2.3), then V is the optimal performance index for the bilinear tracking problem defined in Section 2.1.1 and the corresponding optimal control law is given by (2.13) [107].

Theorem 3: Consider the value function $V(t,x)$ defined in (2.7) for the optimal tracking problem presented in Section 2.1.1. If

$$\begin{aligned}
&\text{(i)} \quad R(t) \succ 0, \ \ \forall t \in [0,T], \\
&\text{(ii)} \quad D(t) \succeq 0, \ \ \forall t \in [0,T], \\
&\text{(iii)} \quad F \succeq 0, \\
&\text{(iv)} \quad E(x) \text{ is Lipschitz continuous on } [0,T],
\end{aligned}$$

then $V(t,x)$ is well-defined and satisfies the HJB equation as in (2.4). Furthermore, if $V \in C^2(\mathbb{R} \times \mathbb{R}^n)$, then V is the optimal performance index.

Proof: The conditions in (i)-(iii) (usually referred to as the Kalman conditions [107, 108]) guarantee the existence of a unique bounded solution $\Pi(t;x,F,T)$ to the Riccati equation (2.10), while the Lipschitz condition in (iv) together with the solution $\Pi(t;x,F,T)$ guarantee the existence and uniqueness of a solution to (2.11). The same argument applies to (2.12). Hence, $P(t)$, $g(t)$ and $h(t)$ exist, and they are unique and bounded, which implies $V(t,x)$ exists and satisfies the HJB equation. Moreover, if V is twice continuously differentiable, then, by Theorem 2, $V(t,x)$ is the optimal performance index for the bilinear tracking problem, since $R(t) \succ 0$, for all $t \in [0,T]$, offers convexity for L, i.e., $\frac{\partial^2 L}{\partial u^2} \succ 0$. □

Note that in situations where either condition (ii) or (iii) is not met, one may refer to [109] for the sufficiency conditions for the finite escape times and to [110] on how to compute the upper bound on the escape time. In addition, previous studies for the infinite-time regulator have shown that the pair of system matrices, $(A, B(x))$ as in (2.1), needed to be point-wise stabilizable in order to obtain a valid solution of the algebraic state-dependent Riccati equation [111]; moreover, for the existence of a unique stabilizing solution, the point-wise detectability of the pair $(A, \sqrt{Q})$ is necessary [111,

14]. For tracking problems in general, controllability of the system plays an important role. For example, it is known that for linear systems if the plant is completely controllable, then the solution to the algebraic Riccati equation exists [107], provided conditions (i) and (ii) hold. However, for the LQR problems, the systems need not be controllable for an optimal control to exist [105].

By Theorem 2 and 3, one can establish the existence of an optimal control further with controllability. Moreover, by the Mangasarian sufficient condition [112] if the dynamics of (2.1) and the Lagrangian $L(t,x,u)$ are (strictly) jointly convex in x and u, $\forall (t,x,u) \in [0,T] \times \mathbb{R}^n \times \mathbb{R}^m$, then the optimal control $u^*(t)$ is the global minimizer of the performance index in (2.3). A less restrictive condition is given by the Arrow sufficient condition, which only requires $\min_{u \in \mathcal{U}} \mathcal{H}(t,x,u,V_x)$ be convex in x (where $\mathcal{H}$ is the Hamiltonian). If the states that are to track a reference trajectory are controllable and observable (if output feedback), then the optimal tracking control exists and is unique. Note that it would not be very meaningful to talk about optimal tracking without having controllability of the state(s) tracking a reference trajectory.

2.3 Numerical Simulations

We demonstrate the effectiveness and applicability of the iterative method through three examples. The first one involves tracking a one-dimensional bilinear system, for which a closed-form solution is available and is used as a benchmark for the iterative method. The second example involves a two-dimensional bilinear system proposed in [14], which allows a comparison of our method to the method presented in [14] using the cost data, while the third example demonstrates the tracking capability by tracking a spin trajectory on a sphere.

Example 1 (Tracking a Scalar Bilinear System)**:** Consider the tracking problem for a one-dimensional bilinear system, given by

$$\begin{aligned} \min_{u\in\mathcal{U}} \quad & J = \frac{1}{2}F(x-z) + \frac{1}{2}\int_0^T Q(x-z)^2 + Ru^2 dt \\ \text{s.t.} \quad & \dot{x} = -x + (x+2)u, \quad x(0) = 1, \end{aligned} \tag{2.28}$$

where we wish to track a constant function $z(t) \equiv 0$. In this case, we have $A = -1$, $B(x) = x+2$, $Q = 1$, $F = 0$ and $R = 2$, and the Kalman conditions are satisfied. Therefore, a bounded solution $P(t)$ of (2.10) exists for all $t \in [0,T]$. In particular, an analytic expression of the optimal control law can be obtained by solving (2.10) and (2.11), given by

$$P(t) = \sqrt{R^2 + B(x)^2 QR}\frac{\tanh[-\sqrt{1 + B(x)^2 QR^{-1}}(t+c)] - R}{B(x)^2}, \tag{2.29}$$

where

$$c = -\tanh^{-1}\left(\frac{R + B(x)^2 F}{\sqrt{R^2 + B(x)^2 QR}}\right) / \sqrt{1 + B(x)^2 QR^{-1}} - T, \tag{2.30}$$

and

$$g(t) = \left(\frac{Wz}{A - EP} + g(T)\right) e^{(A-EP)(T-t)} - \frac{Wz}{A - EP}. \tag{2.31}$$

In this particular example, given that the desired state is zero for all t, the bilinear tracking problem is reduced to a bilinear quadratic regulator, and the optimal control is given by $u(t) = -R^{-1}B(x)P(t)x(t)$, which is plugged in (2.28) to obtain the optimal trajectory. The optimal control and trajectory obtained by the analytical expression and the iterative algorithm are displayed in Figure 2.1, which show great agreement between the two solutions.

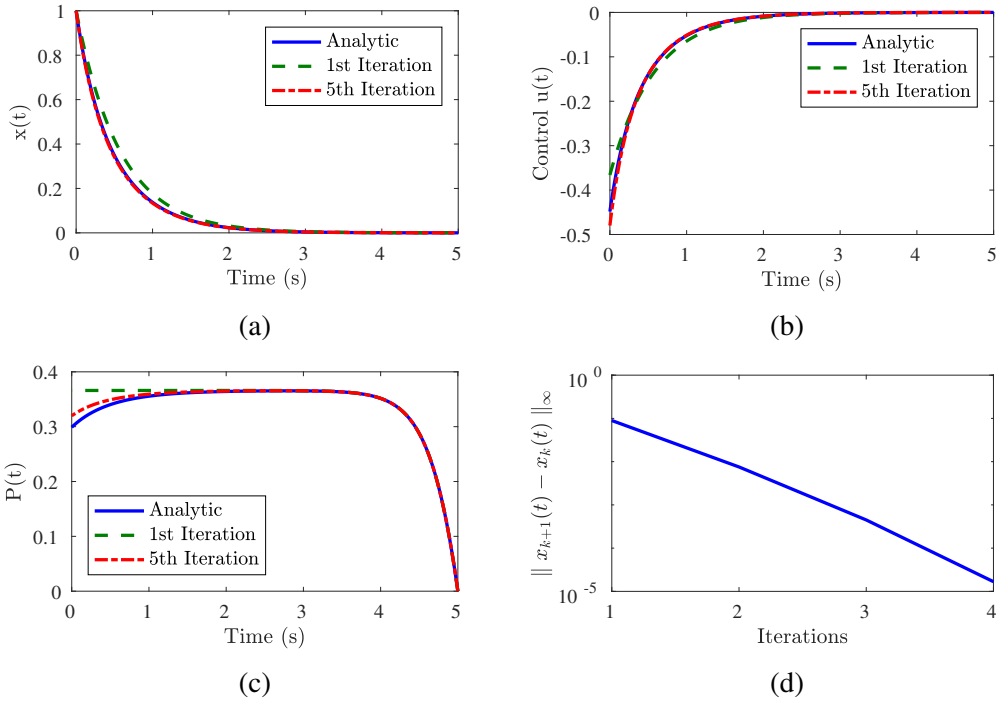

Figure 2.1: Simulation results for the tracking problem in Example 1. (a) Optimal state trajectories. (b) Optimal controls. (c) Riccati coefficient. (d) State convergence behavior.

There is a small difference in the Riccati coefficient $P(t)$ between the analytical and iterative solutions due to numerical errors. This small difference is reflected in the optimal cost values, that is, $J^*(u) = 0.1596$ and 0.1597 from the analytical solution and the iterative method, respectively.

Example 2 (Tracking a Two-Dimensional Bilinear System)**:** Consider the following bilinear system with the cost functional taken from [14],

$$\begin{aligned} \min_{u,v\in\mathcal{U}} \quad & J = \frac{1}{2}\int_0^T (2x^2 + y^2 + u^2 + 2uv + 4v^2)dt \\ \text{s.t.} \quad & \dot{x} = -x + 4y + (3 + x + y)u + v, \\ & \dot{y} = -4x - y + (x + y)u + (2 + x + y)v, \end{aligned} \tag{2.32}$$

with initial conditions $x(0) = 4$ and $y(0) = 0$, and the desired state to track is $z(t) \equiv 0$. Note that the final time is finite as opposed to the examples in [15] and [14], where the infinite time regulator problems were considered. Since the system (2.32) reaches the zero states in approximately 2 seconds as observed in [15] and [14], a final time of $T = 4$ seconds was chosen for simulation purposes. In [14] the authors compared the performance criterion per iterations obtained with their algorithm to that obtained by the algorithm presented in [15], and came to the conclusion that the two approaches agree once the solutions had converged.

In Figure 2.2, we provide the simulation results for this bilinear system, and in particular, Figure 2.2(c) shows a comparison of the data on performance criterion provided in [14] and the one obtained with our algorithm. Evidently, our method performs better as it attains the lowest cost and converges after two iterations. Figures 2.2(a)-(b) show the state trajectories $x_k(t)$ and $y_k(t)$ at the first, second and fifth iterations. The convergence of the states measured as $\|\xi_k(t)\| = \|x_{k+1} - x_k\|_\infty$ is shown in Figure 2.2(d), which shows that the states converge logarithmically. Furthermore, we computed the supremum norms of the HJB equation at each iteration; and as one can see from Figure 2.2(d), the norm $\|HJB\|_\infty$ approaches zero which means that the converged solution is optimal.

Example 3 (Tracking a Spin Trajectory)**:** In this example, we consider tracking a reference trajectory on a sphere for a bilinear system described by the Bloch system [16], while minimizing the cost function in (2.3). The dynamic of the system are described by $\dot{x_1} = -\omega x_2 + x_3 u_1$, $\dot{x_2} = \omega x_1 - x_3 u_2$, $\dot{x_3} = -x_1 u_2 + x_2 u_2$.

As it can be seen from Figure 2.3, our iterative method closely track the reference trajectory while minimizing the control effort. If one wished to reduce the tracking error, one needs to penalize more the states by increasing the values of $Q(t)$ matrix entries, while penalizing less the control energy with the matrix R.

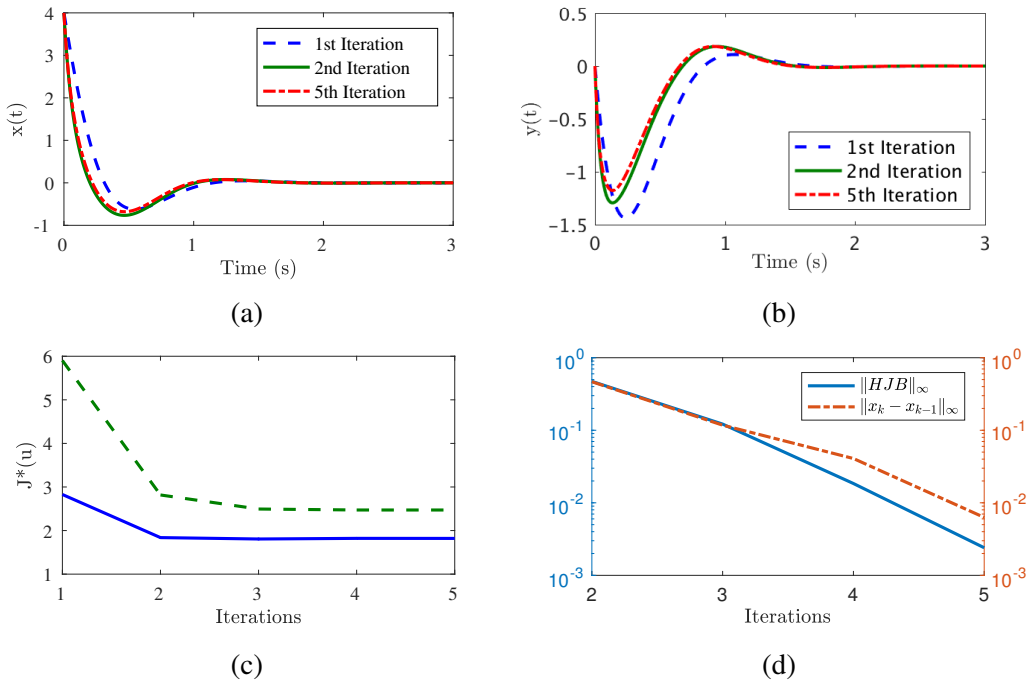

Figure 2.2: Simulation results for the 1-D bilinear system in Example 2. (a)-(b) State trajectories of $x(t)$ and y, respectively. (c) Comparison of the performance index obtained by our algorithm (blue) and the one presented in [14] (green). (d) Peak values of the HJB equation for the first five iterations and the convergence behavior of the states.

2.4 Application to Nuclear Magnetic Resonance Spectroscopy

Experiments in nuclear magnetic resonance (NMR) spectroscopy consist of controlling quantum systems from initial to final target states by applying appropriate pulse sequences (controls) [100]. However, in the presence of relaxation i.e., dissipation and decoherence, the performance of the control can be diminished which can result in loss of information [101]. Hence, the design of optimal controls that minimize the effect of relaxation and improve the sensitivity of the quantum systems is of fundamental importance. This problem has been investigated extensively in literature [99, 100, 101, 7, 8].

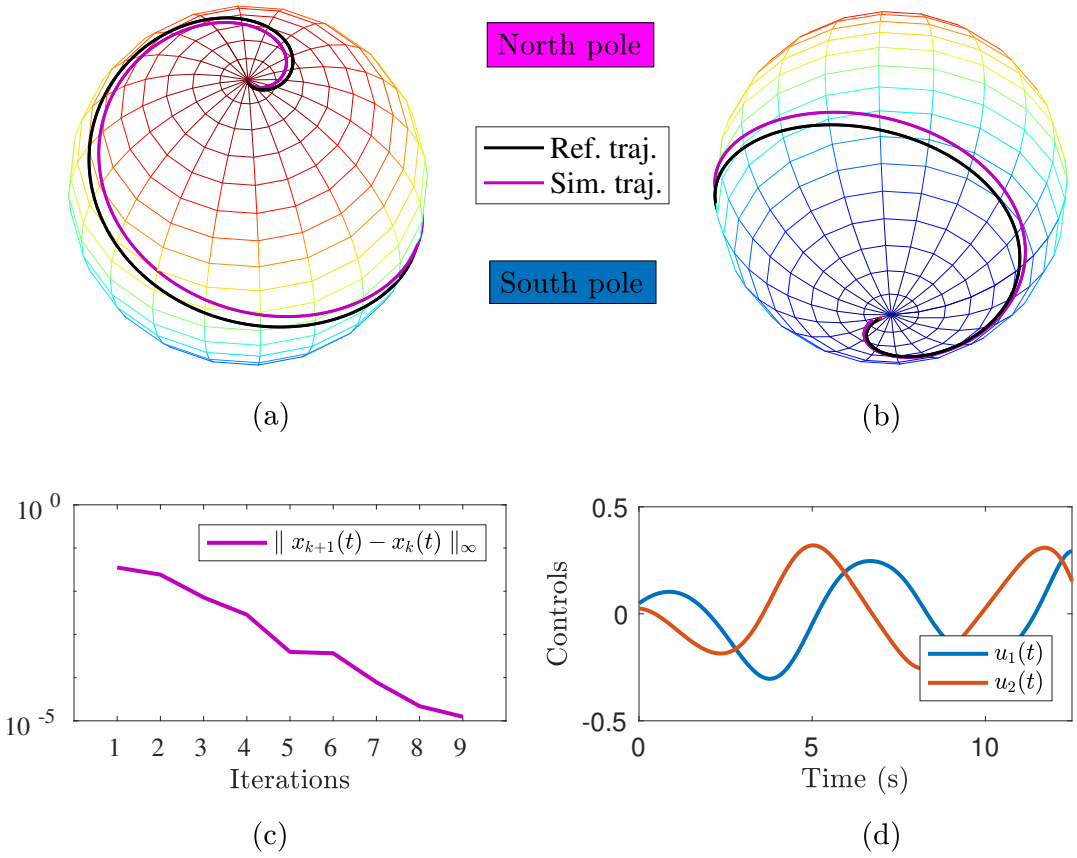

Figure 2.3: Tracking a trajectory on a Bloch sphere. (a) and (b) show the reference and simulated trajectories from the north to the south pole. (c) shows the convergence behavior of the trajectory. (d) Optimal control inputs.

In this section, we consider three examples optimal control problems on open quantum systems that arise in NMR spectroscopy of proteins in liquids. These problems have been treated in literature [7, 8, 101], and analytical solutions have been provided [99, 100], which will be taken as benchmarks for testing the performance of our control algorithm. The systems considered in the following sections are described in details in [113, 7].

2.4.1 Coupled Spin Pair without Cross-correlated Relaxation

Here we consider the open quantum system of large molecules in the spin-diffusion limit, where the longitudinal relaxation rates are negligible compared to transverse [8]. In particular, we ignore the cross-correlated relaxation and only consider the dipole-dipole (DD) and chemical shift anisotropy (CSA) relaxation. For a pair of isolated heteronuclear spins 1/2, we then consider the optimal control problem for designing relaxation pulses or controls $[u(t), v(t)]$ that maximize the coherent transfer. The dynamical system representing the time evolution of the expectations of the operators, is given by the following differential equation [7]

$$\begin{bmatrix} \dot{x}_1 \\ \dot{x}_2 \\ \dot{x}_3 \\ \dot{x}_4 \end{bmatrix} = \begin{bmatrix} 0 & -u & 0 & 0 \\ u & -\xi & -J & 0 \\ 0 & J & -\xi & -v \\ 0 & 0 & v & 0 \end{bmatrix} \begin{bmatrix} x_1 \\ x_2 \\ x_3 \\ x_4 \end{bmatrix}, \tag{2.33}$$

where x_i's are the expectation values of the spin operators, and $J = 1$, is the scalar coupling constant [114]. The aim here is to maximize the final value of x_4. It was shown that the maximum achievable value of x_4, also referred to as efficiency, η_1, of the transfer is a function of the parameter ξ, and is given by

$$\eta_1 = \sqrt{\xi^2 + 1} - \xi, \tag{2.34}$$

and the optimal pulse that achieved this transfer was denoted ROPE [100].

Using our proposed iterative control method described in Algorithm 1, we designed the controls $u(t)$ and $v(t)$ for various values of the parameter $\xi \in [0, 1]$ to maximize the final value of $x_4(T)$, i.e., at the final time T. In Figure 2.4, for comparison we plot the theoretical results computed with (2.34) for various values of ξ, the results obtained by the INEPT (insensitive nuclei enhanced by

polarization transfer) method [115, 99] and our method (denoted optimal), respectively. Our low amplitude and minimum energy controls (see Figure 2.5) achieved very good performance when compared to the theoretical results in [100] and the pseudospectral method in [7].

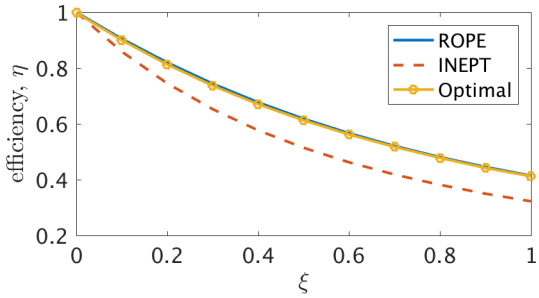

Figure 2.4: Transfer efficiency, η_1, for the system (2.33) with $\xi \in [0,1]$.

To design the controls (Figure 2.5(b)) that achieve the transfer $(1,0,0,0)'$ to $(0,0,0,\eta_1)'$ at time $T = \pi$, we set the final states as $(0,0,0,1)'$ then the algorithm find the feasible solution that minimizes the energy of the controls while maximizing η_1. The maximum efficiency reached was within 2×10^{-3} of the theoretical value given by (2.34).

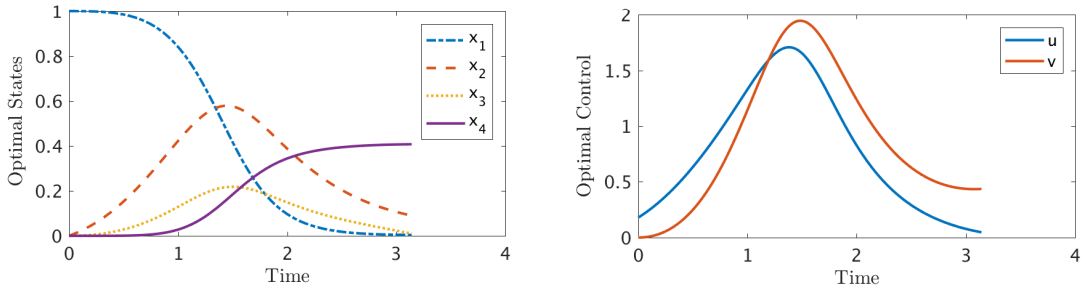

(a) (b)

Figure 2.5: Optimized trajectories and the control signals for the system (2.33). (a) State trajectories for the transfer $(1,0,0,0)'$ to $(0,0,0,\eta_1)'$ with $\xi = 1$ and $T = \pi$. The maximum efficiency achieved is $\eta_1 = 0.4122$. (b) Minimum energy control inputs.

2.4.2 Coupled Spin Pair with Cross-correlated Relaxation

We now consider the situation where DD-CSA cross-correlated relaxation is not negligible. In this case, the system is described by the following equation for the ensemble averages [7]:

$$\begin{bmatrix} \dot{x}_1 \\ \dot{x}_2 \\ \dot{x}_3 \\ \dot{x}_4 \\ \dot{x}_5 \\ \dot{x}_6 \end{bmatrix} = \begin{bmatrix} 0 & -u & v & 0 & 0 & 0 \\ u & -\xi_a & 0 & -1 & -\xi_c & 0 \\ -v & 0 & -\xi_a & -\xi_c & 1 & 0 \\ 0 & 1 & -\xi_c & -\xi_a & 0 & -v \\ 0 & -\xi_c & -1 & 0 & -\xi_a & u \\ 0 & 0 & 0 & v & -u & 0 \end{bmatrix} \begin{bmatrix} x_1 \\ x_2 \\ x_3 \\ x_4 \\ x_5 \\ x_6 \end{bmatrix}, \tag{2.35}$$

where $u(t)$ and $v(t)$ are the controls. In this case, starting with the initial states $x(0) = (1,0,0,0,0,0)'$, and we want to maximize the final value of $x_6(T)$ while minimizing the control effort.

As in the previous case, this problem has been solved analytically and the control was denoted CROP [99]. It was shown as well that the maximum achievable value of x_6, i.e., the efficiency η_2 of the transfer, is given by

$$\eta_2 = \sqrt{\xi^2 + 1} - \xi, \tag{2.36}$$

where $\xi = \sqrt{(\xi_a^2 - \xi_c^2)/(1+\xi_c^2)}$. Similar to the previous case, we consider that ξ_a takes values in $[0,1]$ and $\xi_c = 0.75\xi_a$. In Figure 2.6, we compare the performances of CROP, INEPT and our method (denoted optimal). As one can see, the efficiency achieved using the optimal control is very close to the theoretical limit obtained with CROP. The states trajectories of the system for the case $\xi_a = 1$ are shown in Figure 2.7(a) and the corresponding controls in Figure 2.7(b). The maximum efficiency achieved is $\eta_2 = 0.5991$, which is just half a percent lower than the theoretical value.

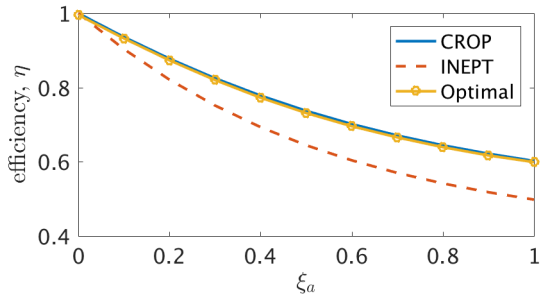

Figure 2.6: Transfer efficiency, η_2, for the system (2.35) with $\xi_a \in [0,1]$ and $\xi_c = 0.75\xi_a$.

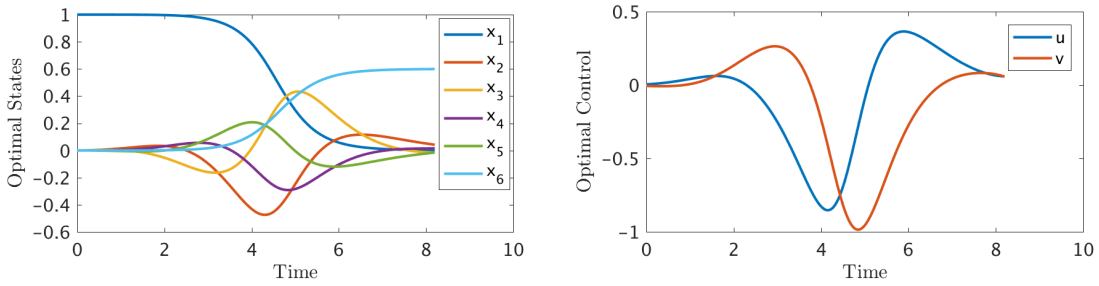

(a) (b)

Figure 2.7: Optimized trajectories and the control signals for the system (2.35). (a) State trajectories for the transfer $(1,0,0,0,0,0)'$ to $(0,0,0,0,0,\eta)'$ with $\xi_a = 1$ and $T = 8.2$. The maximized efficiency $\eta_2 = 0.5991$. (b) Minimum energy control inputs.

2.4.3 Three Spin Chain

The last open quantum system that we consider here, consists of three spin chain with equal couplings between nearest neighbors. However, we neglect cross-correlated relaxation and focus our attention on slowly tumbling molecules in the spin diffusion limit. The corresponding master equation is given in [7], and the associated differential equation describing the time evolution of

the expectation values of the operators participating in the transfer, is given as

$$\begin{bmatrix} \dot{x}_1 \\ \dot{x}_2 \\ \dot{x}_3 \\ \dot{x}_4 \\ \dot{x}_5 \end{bmatrix} = \begin{bmatrix} 0 & -u & 0 & 0 & 0 \\ u & -\xi & -1 & 0 & 0 \\ 0 & 1 & -\xi & -1 & 0 \\ 0 & 0 & 1 & -\xi & -u \\ 0 & 0 & 0 & u & 0 \end{bmatrix} \begin{bmatrix} x_1 \\ x_2 \\ x_3 \\ x_4 \\ x_5 \end{bmatrix}. \tag{2.37}$$

In this case, the goal is to design a single control $u(t)$ that, starting from $x(0) = (1,0,0,0,0)'$ will maximize the final value of $x_5(T)$ while minimizing the control energy. The theoretical upper bound of the achievable efficiency η_3, i.e., the maximum value of x_5 was determined in [101], and is given by,

$$\eta_3 = \frac{(\sqrt{\xi^2+2}-\xi)^2}{2}. \tag{2.38}$$

The performance of our iterative control algorithm denoted optimal, is shown in Figure 2.8. These results are consistent with previous methods as shown in [7] for the gradient and pseudospectral methods, respectively, or in [101] for the Gaussian pulse and the steepest descent.

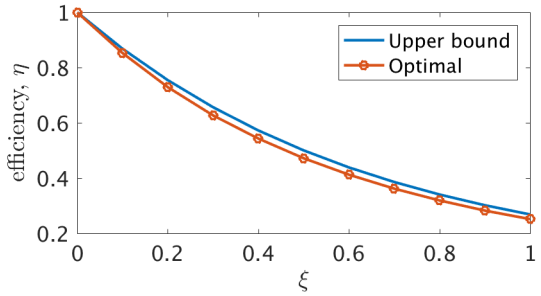

Figure 2.8: Transfer efficiency, η_3, for the system (2.37) with $\xi \in [0,1]$.

For the case when $\xi = 1$, we plot the states trajectories in Figure 2.9(a), while the minimum energy control is given in Figure 2.9(b) together with the Gaussian control [101]. Furthermore, we compare the power of the optimal control obtained with Algorithm 1 to the power of the Gaussian pulse given in [101] that achieved the same transfer efficiency; our control algorithm designed a pulse that uses 2.82% less power than the Gaussian pulse.

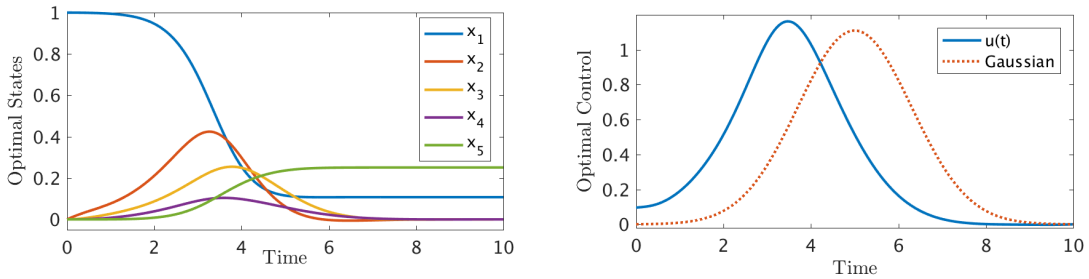

(a) (b)

Figure 2.9: Optimized trajectories and the control signals for the system in (2.37). (a) State trajectories for the transfer $(1,0,0,0,0)'$ to $(0,0,0,0,\eta_3)'$ with $\xi = 1$ and $T = 10$. The maximized efficiency is $\eta_3 = 0.2510$. (b) Minimum energy control (blue) and the Gaussian control signal (red). The powers of the two controls were $P_u = 0.276$ and $P_g = 0.284$, respectively.

2.5 Ensemble Control of Bloch Systems

In this section, we demonstrate the application of Algorithm 1 to a class of control problems, called ensemble control, that involves the manipulation of a large number dynamical systems with parameters dispersion, using a common input signal [6]. Here, we consider the control of Bloch system ensembles, which is a collection of bilinear systems evolving on SO(3) that exhibit dispersion in their natural frequencies ω (Larmor dispersion) and rf inhomogeneity ε. It has been shown that the Bloch system is ensemble controllable with respect to the parameters ω and ε [6, 24, 16].

Consider the family of Bloch equations

$$\begin{bmatrix} \dot{x}(t,\varepsilon,\omega) \\ \dot{y}(t,\varepsilon,\omega) \\ \dot{z}(t,\varepsilon,\omega) \end{bmatrix} = \begin{bmatrix} 0 & -\omega & \varepsilon u(t) \\ \omega & 0 & -\varepsilon v(t) \\ -\varepsilon u(t) & \varepsilon v(t) & 0 \end{bmatrix} \begin{bmatrix} x(t,\varepsilon,\omega) \\ y(t,\varepsilon,\omega) \\ z(t,\varepsilon,\omega) \end{bmatrix}, \tag{2.39}$$

indexed by the parameters $\omega \in \mathcal{K} \subset \mathbb{R}^d$ and $\varepsilon \in \mathcal{D} \subset \mathbb{R}^q$, and controlled using the same control input vector $U(t) = (u(t), v(t))' \in \mathbb{R}^2$. The family of systems in (2.39) is ensemble controllable if there exists a control law $U(t)$ that can steer the system from any initial condition $X(0,\varepsilon,\omega)$ to neighborhood of the final target state $X(T,\varepsilon,\omega)$, in time T.

2.5.1 Broadband Compensating Control for Uniform Transfer

In practical applications, we encounter systems that have dispersions in their parameter values. This is, for example, the case in magnetic resonance applications where the systems can experience both Larmor dispersion and rf inhomogeneity. The latter implies that the intensity of the rf field received by different samples depends on their spatial position, while the former simply means samples have different natural frequencies [6]. If not properly compensated for, these phenomenon can degrade the accuracy of measurements. It is therefore, necessary to devise algorithms that can synthesize compensating control signals that, at the same time, minimize the control energy.

For this application, we consider the Bloch equation in (2.39) that we rewrite in the familiar form, $\dot{x} = Ax + B(x)u$, given in (2.1), as

$$\begin{bmatrix} \dot{x}(t) \\ \dot{y}(t) \\ \dot{z}(t) \end{bmatrix} = \begin{bmatrix} 0 & -\omega & 0 \\ \omega & 0 & 0 \\ 0 & 0 & 0 \end{bmatrix} \begin{bmatrix} x(t) \\ y(t) \\ z(t) \end{bmatrix} + \varepsilon \begin{bmatrix} z(t) & 0 \\ 0 & -z(t) \\ -x(t) & y(t) \end{bmatrix} \begin{bmatrix} u(t) \\ v(t) \end{bmatrix}, \tag{2.40}$$

were $\omega \in [-1,1]$ and $\varepsilon \in [0.9,1.1]$. Here, we wish to uniformly steer the ensemble from the initial condition, $X(0,\varepsilon,\omega) = (0,0,-1)'$, to the final state, $X(T,\varepsilon,\omega) = (0,0,1)'$, while compensating for the dispersion in ε and ω. Using the control Algorithm 1 with the dynamics in (2.40), we design the compensating controls that steer a collection of 100 Bloch systems from the initial states to the desired final state as shown in Figure 2.10.

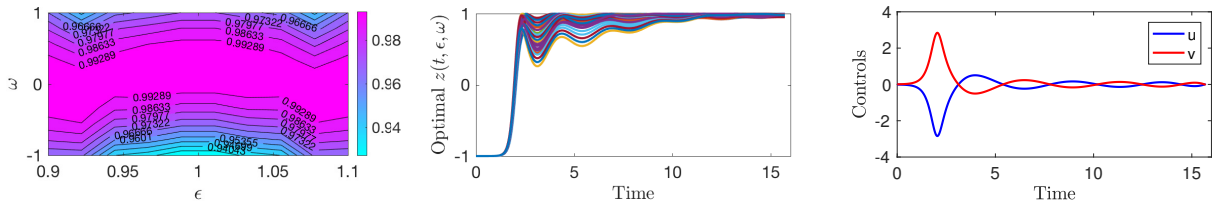

(a) (b) (c)

Figure 2.10: Uniform π-transfer with compensation of Larmor frequency dispersion and rf inhomogeneity. (a) Distribution of the final states $z(T,\varepsilon,\omega)$, with $T = 5\pi$, $\varepsilon \in [0.9,1.1]$ and $\omega \in [-1,1]$. (b) Sample trajectories of the z-states. (c) Compensating control inputs.

2.5.2 Selective Transfer

In some NMR and magnetic resonance imaging (MRI) applications, it is desirable to design controls that steer nuclear spins to different desired final states based on their parameters [116, 117, 6]. Here, we now consider the selective transfer problem of a Bloch system ensemble with $\varepsilon = 1$ and the frequencies $\omega \in \mathcal{K}$, where $\mathcal{K} = [-1,-0.3] \cup [0.3,1]$. Starting with the initial states $X(0,\omega) =$

$(1,0,0)'$, we synthesize the control inputs $(u(t),v(t))$ that transfer the systems to two different final states i.e., $X(T,\omega^-) = (0,0,-1)'$ for $\omega^- \in [-1,-0.3]$ and $X(T,\omega^+) = (0,0,1)'$ for $\omega^+ \in [0.3,1]$. We then apply the designed control to an ensemble with frequencies $\omega \in [-1,1]$, and as it can be seen from Figure 2.11, we achieved the desired transfer for the systems with frequencies $\omega \in \mathcal{K}$ and we observe a transition region for $\omega \notin \mathcal{K}$ (see Figure 2.11(b)). This transition region can be made small, however, it will require stronger rf fields.

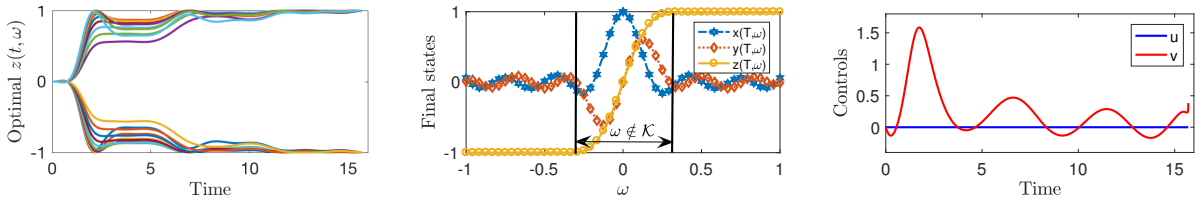

(a) (b) (c)

Figure 2.11: Selective transfer of Bloch ensembles with Larmor frequencies $\omega \in \omega_d$. (a) Sample trajectories of the z-states. (b) Distribution of final states of the Bloch ensemble comprised of 50 systems with frequencies uniformly distributed $\omega \in [-1,1]$.(b) Control signals that transfered the ensemble from the initial state $(1,0,0)'$ to $(0,0,-1)'$ for $\omega \in [-1,-0.3]$ and to $(0,0,1)'$ for $\omega \in [0.3,1]$.

Chapter 3

Control of Spatiotemporal Patterns in Neural Networks

In this chapter, we present a unified control framework for engineering weak stimuli that can dynamically steer the phases or frequencies of either interacting or non-interacting collections of structurally identical oscillators, with variation in system parameters, to some desired target values. Our control algorithm enables the design of open-loop, minimum energy, signals that can steer the phase of an oscillator along a desired trajectory. By being able to steer the phases along desired trajectories, this control algorithm hence allows us to accomplish diverse control objectives such as synchronization, phase assignment and entrainment. We also show that for ensemble controllable systems, complex synchronization patterns can be generated, and hence meaningful spatiotemporal patterns can be obtained. However, when an ensemble of limit-cycle oscillators is only partially controllable, we show that the number of different spatiotemporal patterns that can be generated is greatly reduced, which reduces the information capacity of the network.

3.1 Controlling Rhythmic Systems

Encoding information using a neural network would require controlling the spiking trains of neuron ensembles. In order to take full advantage of the tools developed in control theory, we use mathematical models describing the physical or biological process to be controlled. Next we introduce phase reduction theory which allows us to reduce the dimensionality and complexity of nonlinear oscillators and hence, facilitates the analysis and control design. We then proceed with a brief presentation of controllability theory of nonlinear systems that provides us with the tools for evaluating the controllability of phase model ensembles. We end this section with the presentation of an innovative control technique that can manipulate complex spatiotemporal phase patterns in oscillator networks.

3.1.1 Phase Reduction Theory

The dynamics of nonlinear oscillators such as the Hodgkin-Huxley (HH) neuron model [118] are often described by a set of coupled ordinary differential equations (ODE) exhibiting a stable limit cycle. Consider a time-invariant dynamical model of an oscillating system, described by

$$\dot{x} = f(x,u),\ x(0) = x_0, \tag{3.1}$$

where $x(t) \in \mathbb{R}^n$ is the states vector and $u(t) \in \mathbb{R}$ is a control input. For a system exhibiting an attractive and non-constant limit cycle $\gamma(t) = \gamma(t+T)$, satisfying $\dot{\gamma}(t) = f(\gamma,0)$, on the periodic orbit $\Gamma = \{y \in \mathbb{R}^n : y = \gamma(t) \text{ for } 0 \leq t \leq T\} \subset \mathbb{R}^n$, one can reduce the system to a one-dimensional

phase equation [119, 120, 66, 121],

$$\dot{\theta} = f(\theta) + Z(\theta)u(t), \tag{3.2}$$

where $\theta \in [0, 2\pi)$ is the phase variable, f and Z are real-valued functions, and $u \in \mathcal{U} \subset \mathbb{R}$ is the external control [122, 123, 124]. The function f, also referred to as the instantaneous frequency, represents the baseline dynamics of the oscillator in the absence of the control u, while Z describes the response of the phase to an external stimulus, u, applied at a given phase θ and is referred to as the phase response curve (PRC) [125, 126, 127]. For oscillating systems with known dynamical models, the PRC can be computed numerically, and in this thesis, we employ the adjoint method [128, 127] to efficiently compute the PRCs of nonlinear oscillating systems, namely, the Hodgkin-Huxley and Morris-Lecar (ML) models. A comprehensive review of phase reduction theory is given in Appendix C.2.

In this chapter, we consider various phase oscillator models with different $f(\theta)$ and $Z(\theta)$ functions, to demonstrate the robustness and generality of the control method. Most systems herein are characterized by a constant baseline dynamics, $f(\theta) = \omega$, where $\omega = 2\pi/T_0$ is the natural frequency, however, in the case of oscillator networks, the baseline dynamics $f(\theta)$ will be a nonlinear function due to the coupling function $h(\theta_i, \theta_j)$ with $i \neq j$ and $i = 1, \cdots, n$.

3.1.2 Controllability of Oscillator Ensembles

In order to design an external stimulus that drives either a single or an ensemble of neurons to the desired final state $x(T)$ in time T, it is necessary that the state $x(T)$ be reachable from the initial state $x(0)$ in time T sufficiently large. The collection of points that can be reached from the initial state form the reachable set, which can be determined by computing the recursive Lie

bracket $ad_f^k g(x) = [f, ad_f^{k-1} g](x)$ of the vector fields f and g defined on an open subset Ω of $\mathbb{R}^n$, with $x = (x_1, \cdots, x_n)' \in \Omega \subset \mathbb{R}^n$. For $k = 0$, we have $ad_f^0 g(x) = g(x)$. To compute the reachable set, consider the nonlinear system of the form,

$$\dot{x}(t) = f(x(t)) + u(t)g(x(t)), \;\; x(0) = x_0, \tag{3.3}$$

where f and g are smooth vector fields on a manifold M. Note that since the free evolution of the phase model state is periodic, the drift term f causes no difficulty in analyzing controllability (see theorem 5 in Appendix B.4). Thus, if $\{f, ad_f^k g\}$, $k \in \mathbb{Z}^+$, spans $\mathbb{R}^n$ at all points $x \in \Omega$, any point in $\mathbb{R}^n$ can be reached from any initial condition $x(0)$. With the assumption that the control $u(t)$ is unbounded, this implies that the system is controllable [129]. Ample discussions on the reachability and controllability of nonlinear systems can be found in [27, 130].

Given that the phase model (3.2) is only valid for weak forcing [131], the amplitude of the control signal is therefore bounded. Although theoretically the phase model (3.2) can be shown to be controllable with an unbounded control input $u(t)$ by computing the recursive Lie brackets, large stimuli that steer (3.2) to the desired state will not produce the same result when applied to the full state model or the actual physical system. As a result, arbitrary phase assignment or frequency entrainment of a neuron oscillator is not always feasible in a short period of time ($t \ll T$) with weak external forcing signals, but can be achieved in time $t \gg T$ as long as the desired state is in the reachable set. With the weak forcing restriction in place, which is equivalent to a bounded control input constraint $|u(t)| \leq A$, where A is a constant, only transfers from a point $\theta(0) = p$ to a point $\theta(t) = q$ that lies in the small-time reachable set are feasible. The small-time reachable set

is formally defined as

$$\mathcal{R}_{\Sigma,\leq T}(p) = \{x(t) \in \mathbb{R}^n : \text{there exists a control } u(\cdot) \in \mathcal{U} \text{ defined on an interval } [0,t] \text{ with } t \leq T$$
$$\text{such that } (x(\cdot),u(\cdot)) \text{ is a controlled trajectory defined over } [0,t] \text{ satisfying } x(0) = p\},$$

with the overall time T small [106].

3.1.3 Dynamic Control of Phase Patterns

When a collection of phase model descriptions of oscillating systems is controlled, the design of external inputs that can steer the phase trajectories to any desired target states in T units of time becomes feasible. The general problem of controlling the phase trajectories, or equivalently the frequencies, of oscillators is formulated in a similar way as the tracking problem for bilinear systems in Chapter 2, and it is presented in Appendix B.1.1. Given that bilinear systems and phase models are structurally different, this results in a different solutions of the optimal control problem for phase models as presented in Appendix B.1.2, however, the iterative algorithm given in Appendix B.2 retains the same structure.

In this section, we present a novel and innovative approach to dynamic control of the phase relationships in an ensemble of heterogeneous phase oscillators using a common input. The algorithm presented here can synthesize a tracking control input that assigns a desired, non-constant, phase relationship between oscillators. This design technique allows the formation of various synchronization patterns with a single continuous control input, instead of switching between many different input waveforms in order to achieve different patterns [83]. To demonstrate the capabilities of our control algorithm, in Figure 3.1 we illustrate the problem of assigning a phase difference of $\Delta\theta_{i,j} = \pi/2$ rad between adjacent oscillators at the final time $t = T_f$, while following

a prescribed phase difference trajectory, $\Delta\theta_{\text{ref}}(t)$ (black dashed-line in Figure 3.1(b)-(c)). In this example, we considered a system of four HH neurons with natural frequencies uniformly sampled in $[0.98\omega, 1.02\omega]$, and the neurons were ordered from the slowest (neuron 1, red circle in Figure 3.1(a)), to the fastest (neuron 4, purple circle in Figure 3.1(a)). Tracking a phase trajectory while minimizing the control energy is an important feature of our algorithm that makes it particularly suitable for control of spatiotemporal patterns in neuronal networks, where application of powerful stimuli could harm neurons.

In the tracking example shown in Figure 3.1(c) we defined a linear phase reference trajectory for the slowest neuron as $\theta_{1,\text{ref}}(t) = \omega_1 t$, with $t \in [0, T_f]$. In order to obtained the desired phase difference trajectories, we define the reference trajectories of the subsequent oscillators as $\theta_{j,\text{ref}}(t) = \theta_{i,\text{ref}}(t) + \Delta\theta_{\text{ref}}(t)$, with $i = j-1$ and $j \in [2,4]$. In this case, the algorithm had to design a control input, u_g, that maintains a linear trajectory for the phase of neuron 1, while at the same time imposing the desired phase differences between neurons at every time $t \in [0, T_f]$. However, when we only wish to track or assign relative phase differences between heterogeneous oscillators, it is best to consider the system of phase differences as follow

$$\Delta\dot{\theta}_{ij} = \Delta f_{ij}(\theta_i, \theta_j) + \Delta Z_{ij}(\theta_i, \theta_j)u(t), \tag{3.4}$$

where $\Delta\theta_{ij} = \theta_i - \theta_j$, $\Delta f_{ij}(\theta_i, \theta_j) = f_i(\theta_i) - f_j(\theta_j)$ and $\Delta Z_{ij}(\theta_i, \theta_j) = Z_i(\theta_i) - Z_j(\theta_j)$, with $i = 1, 2, \cdots, n-1$. We may then define the vector of reference trajectories as

$$\Delta\Theta_{\text{ref}}(t) = (\Delta\theta_{1,\text{ref}}, \cdots, \Delta\theta_{n-1,\text{ref}})' \in \mathbb{R}^{n-1}, \tag{3.5}$$

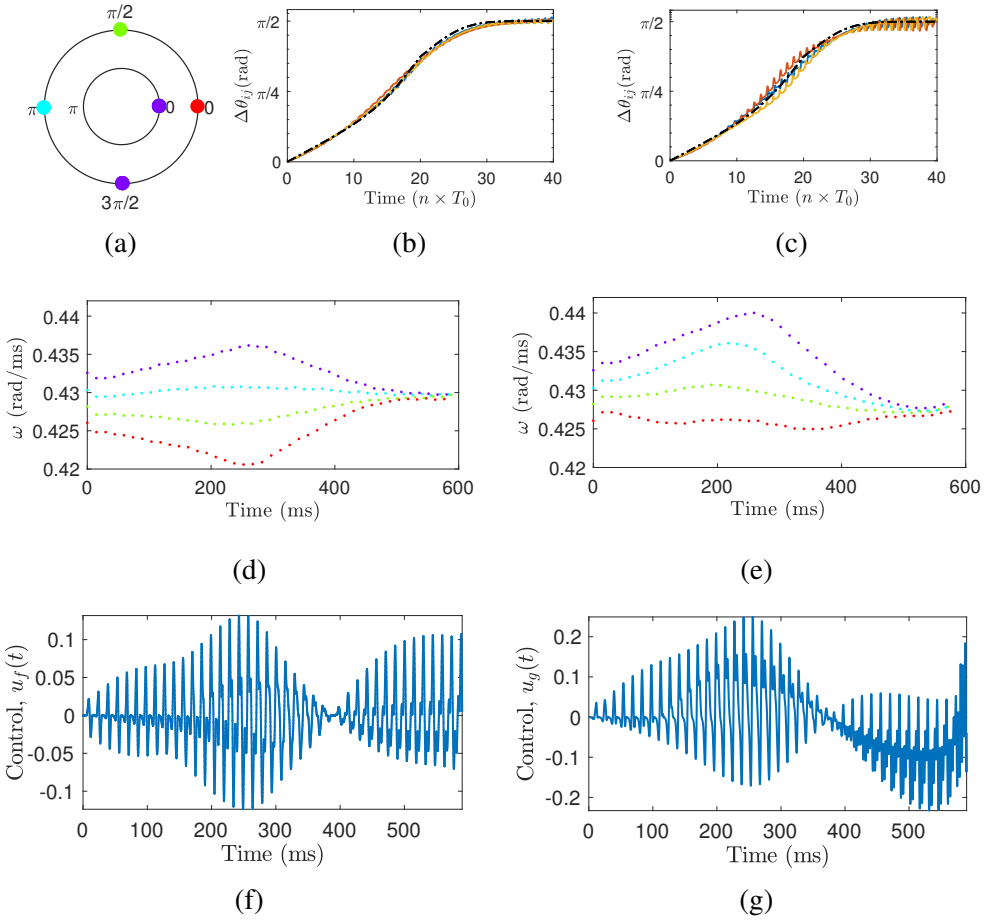

Figure 3.1: Evaluation of the control performances when tracking the phase differences $\Delta\theta_{ij}(t)$ *vs.* the phase trajectories $\theta_i(t)$. (a) Initial and final phases (inner and outer circles, respectively). (b) Phase differences when the control algorithm is tracking a desired phase difference (black), in the time interval $t \in [0, 40 \times T_0]$, where $T_0 = 14.75$ ms. (c) Phase differences when tracking defined phase trajectories with the same phase differences as in (b). (d)-(e) Neurons' spike frequencies during the control interval, and corresponding to the trajectories in (b) and (c), respectively. Each colored dot represents one neuron. (f)-(g) Control signals that generated the trajectories in (b) and (c), respectively. Energy of the control u_f is $\mathcal{E}n = 0.98$ and energy for u_g is $\mathcal{E}n = 4.19$.

where $\Delta\theta_{i,\text{ref}}$ is the reference trajectory of the phase difference between the i^{th} and j^{th} oscillators. Figure 3.1(b) shows an example where we defined identical reference phase difference trajectories for all the adjacent oscillators as $\Delta\theta_{i,\text{ref}}(t) = \Delta\theta_{\text{ref}}(t)$. The initial and final conditions are $\Delta\Theta_{\text{ref}}(0) = 0 \cdot \mathbb{1}$ and $\Delta\Theta_{\text{ref}}(T_f) = \pi/2 \cdot \mathbb{1}$, respectively, where $\mathbb{1} \in \mathbb{R}^{n-1}$ is a vector of ones. With

the desired trajectory defined, we then use the control algorithm in Appendix B.2 with the dynamics in (3.4) to design the control input u_f shown in Figure 3.1(f).

The formulation of the tracking problem using the phase difference (3.4) is advantageous in terms of minimizing the control energy and improving the tracking accuracy. Indeed, as shown in Figures 3.1(f) and (g), the control u_f that was designed using (3.4) has lower amplitude than the control u_g. Furthermore, the energy expanded by u_g was 4.28 times higher than the energy of u_f. The control u_f steered the phases to within 5×10^{-3} of the final target phase difference $\Delta\theta_{ij} = \pi/2$, whereas u_g achieved this goal to within 16×10^{-3}. These two control inputs were applied to the full-states Hodgkin-Huxley neuron models, from which we measured the instantaneous frequencies of the membrane voltages shown in Figures 3.1(d) and (e).

In order to fully understand why one control expanded more energy than the other while accomplishing the same phase pattern, one has to start by observing the instantaneous frequencies of the membrane voltages in Figures 3.1(d) and (e). Note that since we defined a linear reference phase trajectory $\theta_{1,\text{ref}}(t)$ for the slow neuron and that $d\theta/dt = \omega$, this implies that the frequency of this neuron should remain constant during the controlled period. Indeed, this can be seen from the red dots in Figure 3.1(e), whereas in Figure 3.1(d) one can see that the frequency of the slow neuron (in red), first decreased before increasing and settling around the mean frequency of the four neurons considered. Given that in Figure 3.1(e) we kept the frequency of the first neuron constant, the remaining neurons had to speed up much more than in Figure 3.1(d) in order to get into the right phase configuration in the allocated time $T_f = 590$ ms. As it turns out, for the HH model increasing the spiking frequency requires more control energy than reducing the frequency. This is because the PRCs of the HH neurons are not symmetric with respect to the zero axis (see Figure B.1(a) in Appendix B.3.1); this makes it more difficult to increase the spiking rate. As the control examples in Figure B.1(b) show, the control amplitude for reducing the spiking period from 14.6 ms to 13.8

ms is almost double of the control amplitude that increased the period from 14.6 ms to 15.6 ms. So, when only the relative phase difference between oscillators is relevant, it is best to use (3.4) and let the algorithm find the optimal phase trajectories, θ_i's, that minimize the control energy. However, this approach is limited to heterogeneous phase model ensembles.

3.2 Information Processing and Neural Coding

It is rather a general consensus that neuronal networks encode information about the environment into firing patterns [132, 133], e.g., the scent cues processed by the olfactory system are encoded in complex spatiotemporal patterns [134] or the speech evoked spatiotemporal response which has a distribution of the relative phases of the synchronized activity that reflects the stimulus spectral parameters [135]. Certainly, sequential patterns play a role in brain functions such as memory and information processing [136, 71]. It has been argued that synchrony determines the form of the neural code, and its regulation through control of microcircuits is critical in writing the neural code [137]. Hence, control algorithms that can synthesize stimuli (see Figure 3.1, for example) capable of creating arbitrary spatiotemporal firing patterns will play a crucial role in neural coding and information processing, and neuromorphic systems [138] can be used for testing the neural code.

Computation with spikes has gain traction in recent years [139, 140], especially with neuromorphic chips that consume order of magnitude less energy than traditional silicon chips [138, 141]. To maintain this advantage, the development of algorithms minimizing the control energy for these chips will play an important role. Using the Kuramoto model, it was shown that a neurocomputer with dynamic connectivity has oscillatory associative properties [142]. The main function of these types of computers, however, is pattern recognition via associative memory, where the memorized patterns correspond to synchronized states [142, 143].

The prospect of controlling spatiotemporal patterns of spiking neuron populations has implications beyond neuromorphic computing, with potential applications in the medical and entertainment industries. Envision being able to stimulate the neurons in the olfactory system to mimic scents, in the era of 3D videography, this addition could provide a full entertainment experience. The perception of scents accompanying the visualization of 3D scenes will definitely enrich the virtual experience. In medical applications on the other hand, pattern recognition can play a crucial role for people with severe vision impairment. A sensor implant can capture the image and in turn, the neurons associated with vision can be stimulated accordingly to transfer visual information to the brain [58, 60]. However, the success of these types of applications rely on a better understanding of how the brain process information received from the sensory neurons, and on the technology that will allow transduce this information into electrical signal or spiking patterns that the brain can interpret. In that optic, we have developed a control algorithm that can synthesize a global control input, i.e., a single signal that can control an ensemble of neurons or structurally similar oscillators in desired coherent fashion.

Being able control spatiotemporal firing patterns of neurons implies that we could also control them to encode or transfer information. In Figure 3.2, we portray two different ways information could hypothetically be encoded into firing patterns of a neuronal network. Observe for example the encoding presented in the second panel of Figure 3.2, which resembles a colored barcode. This type of encoding can be used to encrypt information as patterns of different colors corresponding to different relative phases of the oscillators. Given the large number of distinct phase difference patterns that can be achieved in neuronal network, this encoding scheme could provide an efficient way of encoding information, furthermore, the encoding or storage capacity of such network could be huge, even with a small number of neurons as in Figure 3.2. The encoding patterns in the second and third panels of Figure 3.2 were generated by a common broadcast control that stimulated all the oscillators simultaneously.

Such global inputs that can generate complex spatiotemporal patterns are of particular importance for bioengineering applications such as retinal implants. This can, for example, lead to a significant reduction of the number of electrodes necessary for a retinal implant to transmit visual information to the visual cortex. It will then be possible to use one electrode to control a large number of neurons in its region of influence. However, such arbitrary control of spiking patterns is only feasible if the neural population is controllable as we are going to show next.

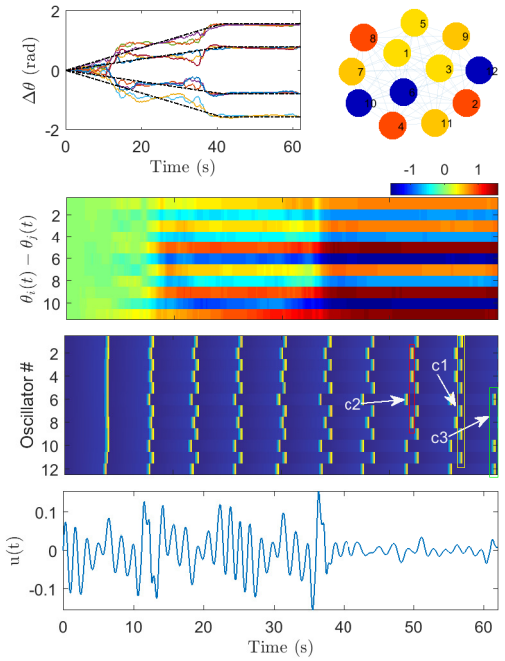

Figure 3.2: Spiking patterns for information coding. Top left plot: phase difference trajectories. Top right plot: phase distribution of the twelve sinusoidal PRC oscillators on the network. Second panel: encoding information as a colored barcode representing the relative phase between oscillators. Third panel: encoding information into firing patterns. The labels c_1, c_2 and c_3 delineate the oscillators in the same cluster. Bottom panel: global control that generated the spiking pattern. The twelve oscillators network was simulated with the following parameters: $\omega_i \in [0.99, 1.01]$, $z_i \in [1.82, 2]$ and $\sigma = 0.0035$.

3.2.1 Controllable Oscillator Networks

The information encoding capacity of a neuronal network, using either of the schemes in Figure 3.2, greatly depends on the ability to control all the ensemble of oscillators, and to some extent, on the number of neurons. In order to generate a large number of distinct spike patterns using a broadcast control, the neuronal system must be controllable. In this section, we consider three neuron models, namely, the SNIPER and sinusoidal PRC models as well as the Hodgkin-Huxley model that we use to demonstrate how one can verify the controllability of such phase models by computing the Lie brackets. In the next section, we will present a case of a partially controllable network and show how the information capacity is affected.

The phase models considered here have constant baseline dynamics $f(\theta) = \omega$, but different phase response functions, e.g., $Z = z(1-\cos\theta)$ for the SNIPER PRC, and $Z = z\sin(\theta)$ for the sinusoidal PRC, respectively, where the constant parameter z is model-dependent [144]. The SNIPER PRC describes neurons near a SNIPER bifurcation –a saddle-node bifurcation on a periodic orbit– which characterize the type I neurons like the Hindmarsh-Rose model [129]. The sinusoidal PRC model has a phase sensitivity function with both positive and negative parts due to proximity to a Hopf or a Bautin bifurcation [123].

The controllability analysis of the SNIPER and sinusoidal PRC phase models has been previously treated in [129]. Here, we reproduce the computed Lie brackets for a finite collection of SNIPER neurons with $f(\Theta) = (\omega_1, \cdots, \omega_n)'$ and $Z(\Theta) = (z_1(1-\cos\theta_1), \cdots, z_n(1-\cos\theta_n))'$. The iterated brackets for $k = 1, \cdots, n$ are given by

$$ad_f^{2k-1} Z = (-1)^{k-1} \left(z_1 \omega_1^{2k-1} \sin\theta_1, \cdots, z_n \omega_n^{2k-1} \sin\theta_n \right)', \tag{3.6}$$

$$ad_f^{2k} Z = (-1)^{k-1} \left(z_1 \omega_1^{2k} \cos\theta_1, \cdots, z_n \omega_n^{2k} \cos\theta_n \right)', \tag{3.7}$$

with $\omega_i \neq \omega_j$, for $i \neq j$. Thus $\mathcal{M} = \{f, ad_f^k g\}$ spans $\mathbb{R}^n$, and therefore, the collection of uncoupled SNIPER neurons is controllable. One can verify by computing the Lie bracket in the same manner that the case of weakly coupled networks of SNIPER neurons remains controllable. However, in this case $f(\Theta) = (\omega_1, \cdots, \omega_n)' + (h_1(\Theta), \cdots, h_n(\Theta))'$ and the calculations can be more involved. For the sinusoidal PRC model, the iterated brackets for $k = 1, \cdots, n$ are given by

$$ad_f^{2k-1} Z = (-1)^{k-1} \left(z_1 \omega_1^{2k-1} \cos\theta_1, \cdots, z_n \omega_n^{2k-1} \cos\theta_n \right)', \tag{3.8}$$

$$ad_f^{2k} Z = (-1)^{k} \left(z_1 \omega_1^{2k} \sin\theta_1, \cdots, z_n \omega_n^{2k} \sin\theta_n \right)', \tag{3.9}$$

and for $\omega_i \neq \omega_j$, $i \neq j$, $\mathcal{M} = \{f, ad_f^k g\}$ spans $\mathbb{R}^n$. Thus this population neurons is controllable.

Given that the collection of sinusoidal PRC phase models is controllable, it is then possible to design a control input that can steer the phases into any desired cluster configuration, and that without requiring any particular ordering of oscillators a priori. This is demonstrated by creating six clusters non-uniformly distributed as shown in Figure 3.3. In this illustration, we consider a collection of 12 weakly coupled oscillators with sinusoidal PRCs (and with sinusoidal coupling as in (3.12)), the frequencies $\omega_i \in [0.99, 1.01]$ and the parameters $z_i \in [1.82, 2]$, for $i = 1, 2, \cdots, 12$. The following clusters $\{1,7\}, \{2,8\}, \{3,9\}, \{4,10\}, \{5,11\}$ and $\{6,12\}$ were formed with phases between consecutive clusters in the following order: $\pi/4$, $\pi/4$, $\pi/2$, $\pi/4$, and $\pi/2$. The first cluster $\{1,7\}$ is shown in Figure 3.3, on the unit circle at zero.

The SNIPER and sinusoidal PRC phase models have PRCs that are represented with just one cosine or sine term, which facilitates the computation of Lie brackets. However, in practice we found rhythmic systems with highly nonlinear PRCs that are often obtained experimentally. In order to check their controllability properties, one could fit the PRC with Fourier coefficients, for example, and then compute the iterated Lie brackets as shown for the two previous models. A

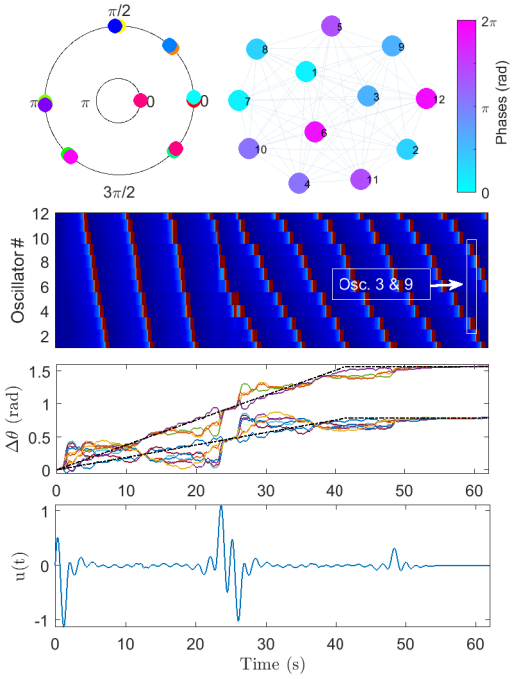

Figure 3.3: Nonuniform phase assignment with sinusoidal PRC oscillators. Top plots: oscillator's phase distributions, on the unit circle and the network. The left panel shows the initial phases (inner circle) and the final phases (outer circle). The right panel shows the phases on the network where each cluster of two oscillators is identified with the same color (phase). The slowest and the fastest oscillators are labeled '1' and '12', respectively. Second panel: time evolution of the oscillator's phase patterns. Third panel: phase differences between oscillators (the dash lines show the desired phase differences). Bottom panel: control signal.

good choice of the fitting method could significantly simplify the computation of the Lie Brackets. To fix the idea, consider the PRCs of the HH neurons shown in Figure B.1(a). A good fit of the PRC using Fourier, $Z(\theta) = \frac{a_0}{2} + \sum_{j=1}^{m}[a_j \cos(j\omega\theta) + b_j \sin(j\omega\theta)]$ requires at least four sine and cosine terms, i.e., $m = 4$. However, this PRC can also be accurately fitted with only the sum of four sine terms, $Z(\theta) = \sum_{j=1}^{m} a_j \sin(b_j\theta + c_j)$, which is more compact and increase the readability

of the Lie brackets shown here,

$$ad_f^{2k-1}Z = \begin{bmatrix} (-1)^{k-1}\omega_1^{2k-1}\sum_j^m a_{j,1}b_{j,1}^{2k-1}\cos(b_{j,1}\theta_1 + c_{j,1}) \\ (-1)^{k-1}\omega_2^{2k-1}\sum_j^m a_{j,2}b_{j,2}^{2k-1}\cos(b_{j,2}\theta_2 + c_{j,2}) \\ \vdots \\ (-1)^{k-1}\omega_n^{2k-1}\sum_j^m a_{j,n}b_{j,n}^{2k-1}\cos(b_{j,n}\theta_n + c_{j,n}) \end{bmatrix}, \tag{3.10}$$

$$ad_f^{2k}Z = \begin{bmatrix} (-1)^{k}\omega_1^{2k}\sum_j^m a_{j,1}b_{j,1}^{2k}\sin(b_{j,1}\theta_1 + c_{j,1}) \\ (-1)^{k}\omega_1^{2k}\sum_j^m a_{j,2}b_{j,2}^{2k}\sin(b_{j,2}\theta_1 + c_{j,2}) \\ \vdots \\ (-1)^{k}\omega_n^{2k}\sum_j^m a_{j,n}b_{j,n}^{2k}\sin(b_{j,n}\theta_n + c_{j,n}) \end{bmatrix}. \tag{3.11}$$

Similar to the other two cases, for $\omega_i \neq \omega_j$, $i \neq j$, the population of HH neurons is controllable. We then demonstrate the control of an ensemble of 100 heterogeneous neurons, with frequencies $\omega_i \in [0.42605, 0.432831]$ rad/ms. In Figure 3.4, we present uniform desynchronization where the phase difference between two adjacent neurons is $2\pi/100$ rad. The control input was designed to track a ramping phase difference between adjacent neuron for 400 ms, then maintain the phase difference constant for 190 ms. This explains why the frequencies of each neurons in the third panel of Figure 3.4 remains nearly constant during those two time intervals. Figure 3.5 on the other hand shows a more challenging application, that is, clustering neurons with nearly identical frequencies in three different clusters. In this example, we designed a control signal that, starting with the oscillators uniformly distributed as in Figure 3.4, steers the neurons into three clusters based on their natural frequencies. The first, second and third clusters contained neurons with the following frequencies $(\omega_{1l}, \omega_{1h}) = (0.42605, 0.42825)$ rad/ms, $(\omega_{2l}, \omega_{2h}) = (0.42831, 0.43011)$ rad/ms and $(\omega_{3l}, \omega_{3h}) = (0.43017, 0.43258)$ rad/ms, respectively.

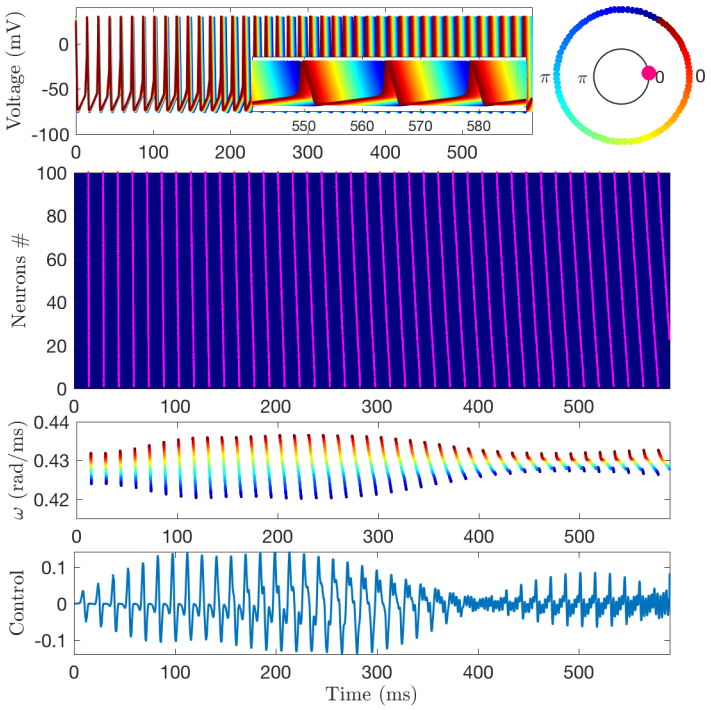

Figure 3.4: Uniform phase distribution of 100 HH neurons. Top left panel: membrane voltages. Top right panel: initial and final phase distributions of the membrane voltage phases. The inner circle shows the initial phases and the outer circle shows the final phases. Second panel: spiking patterns of the neurons. Third panel: instantaneous measured frequencies of each neurons during the control interval. Each colored dot represents one neuron. Fourth panel: control signal.

The ability to control oscillators into forming complex clustering patterns will facilitate information processing or encoding using networks of oscillators or neurons. We demonstrate this in Figure 3.6, where starting from slightly different phases, a weakly coupled network of 25 heterogeneous SNIPER oscillators is controlled with the input $u_w(t)$ to form the patterns "W" (Figure 3.6(b)), then starting with "W" as initial condition, another control signal $u_u(t)$ is applied to form the pattern "U" (these two letters are the initials for Washington University). The phases and frequency differences between adjacent oscillators are shown in Figure 3.6. The letter patterns were obtained by assigning the same phase, e.g., 0 rad, to all the oscillators forming the letter pattern and the remaining oscillators were assigned a phase equal to π rad. The phase difference

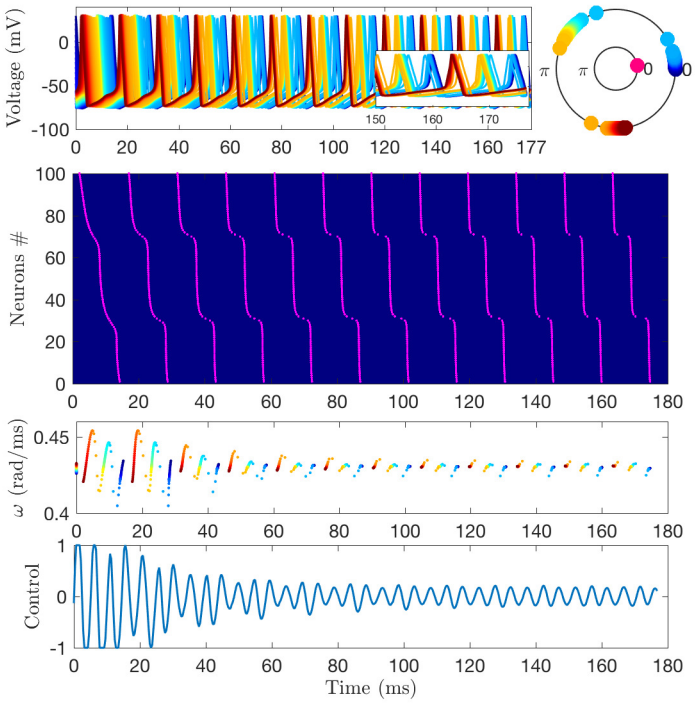

Figure 3.5: Clusters formation with 100 HH neurons. Top left panel: membrane voltages. Top right panel: initial and final phase distributions of the membrane voltage phases. The inner circle shows the initial phases and the outer circle shows the final phases. Second panel: spiking patterns of the neurons. Third panel: instantaneous measured frequencies of each neurons during the control interval. Each colored dot represents one neuron. Bottom panel: control signal. The three clusters contain neurons with frequencies in $(\omega_{1l}, \omega_{1h}) = (0.42605, 0.42825)$ rad/ms, $(\omega_{2l}, \omega_{2h}) = (0.42831, 0.43011)$ rad/ms and $(\omega_{3l}, \omega_{3h}) = (0.43017, 0.43258)$ rad/ms, respectively.

trajectories in the middle right panel of Figure 3.6(a) show how the π phase difference between different oscillators was assigned following a linear reference trajectory for 23 seconds, then once the oscillators in the right configuration, the phase differences were maintained for 8 seconds.

The proposed control algorithm can be used to design stimuli that generate complex spatiotemporal phase or spike patterns that encode the information. This control technique could, for example, be integrated in retinal implants to stimulate the optic nerves according to the image captured by the implant. It is however, important that the oscillator system be controllable for the algorithm to be able to synthesis controls capable of generating diverse spatiotemporal patterns. In the case where

the system is not fully controllable, only limited phase patterns can be generated as we show in the next section, and this limited controllability reduces the information capacity of a neuronal network and impair information processing in neuronal networks.

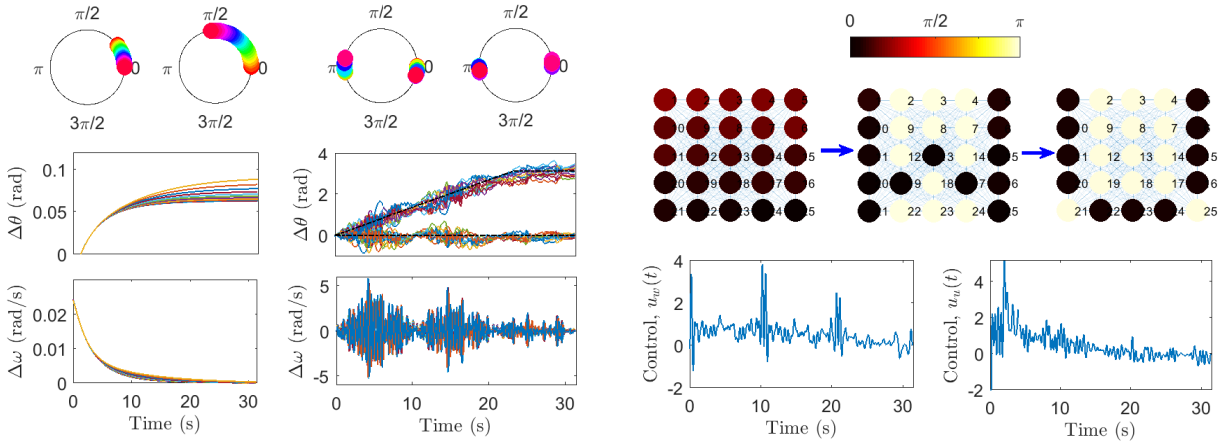

(a) (b)

Figure 3.6: Pattern formation in a globally coupled network of SNIPER PRC oscillators. (a) Oscillators phase distributions on the unit circle (top plots). From left to write: initial phases, final phases for the uncontrolled network, final phases of the pattern "W" and final phases of the pattern "U". Middle panels: trajectories of the phase differences and bottom panels: frequency differences trajectories during the formation of the letter "W". (b) Formation of letter patterns on a 5×5 grid of oscillators. Starting with oscillators phases, $\theta_i \in [0, \pi/4]$ rad, the pattern of the letter "W" was formed by applying the control $u_w(t)$, then starting with the letter "W" as initial states the control $u_u(t)$ was applied to form the letter "U". The parameters of the oscillators are $\omega_i \in [0.8, 1.2]$ and $z_i \in [1, 2]$ and the coupling $\sigma = 0.3$.

3.2.2 Partially Controllable Networks

In Section 3.2.1, we have shown that when an ensemble of neural oscillators is controllable, by applying an appropriate control signal, complex spatiotemporal patterns can be created. It is then possible to encode a significant amount of information using different phase patterns or precise firing pattern of neurons. However, what happens when a network loses controllability, or it is only partially controllable, is an interesting question worth exploring. In this section, we discuss

the control of coupled oscillators with constant PRCs, furthermore, we analyze the controllability of such networks and show that they are only partially controllable which limits the number of spatiotemporal patterns that can be achieved. In this thesis, a system is said to be partially controllable when only a small subset of points in the state-space are reachable from the initial states.

To fix the idea, we consider a network of coupled limit-cycle oscillators described by the Kuramoto model, as follows

$$\frac{d\theta_i}{dt} = \omega_i + \frac{\sigma}{n}\sum_{j=1}^{n}\sin(\theta_j - \theta_i) + b_i u(t), \quad i = 1\cdots n, \tag{3.12}$$

where θ_i is the phase of the i^{th} oscillator and ω_i its natural frequency. We consider uniform coupling strength σ and $u(t)$ is an external control applied to all the oscillators through an input vector $B = (b_1, \cdots, b_n)'$, with $b_i \neq b_j$ constant values. The design of the control input in this section is carried out using the same iterative algorithm as in previous examples, however, the baseline dynamic is now a nonlinear function of the form

$$f(\theta_i) = \omega_i + \frac{\sigma}{n}\sum_{j=1}^{n}\sin(\theta_j - \theta_i), \tag{3.13}$$

due to the coupling function $h(\Theta) = (h_1, \cdots, h_n)'$, where $h_i(\Theta) = \frac{\sigma}{n}\sum_{j=1}^{n}\sin(\theta_j - \theta_i)$ [122].

We first consider a globally coupled network of ten oscillators with coupling strength $\sigma = 0.7 > \sigma_c$, where σ_c is the critical coupling of the network. In Figure 3.7 we show both the controlled and uncontrolled network. By selecting a coupling $\sigma > \sigma_c$, the uncontrolled network synchronizes in the absence of any external forcing inputs (see the left panels in Figure 3.7(a)). The phase of each oscillator in the network are shown on the graph in Figure 3.7(a). We then designed a control input $u(t)$ to track a desired phase difference of $\Delta\theta = 2\pi/5$ between adjacent oscillators i and j $(j = i+1)$ in the time interval $[0, T]$. Applying the designed forcing input $u(t)$ (bottom right in Figure 3.7(b)) to the network generates five distinct clusters (see the right panel of Figure 3.7(a)),

and it prevents synchronization (see Figure 3.7(b)) by overcoming the influence of coupling. However, the clustering is not perfect due to the interaction forces that tend to pull the oscillators to a synchronized state.

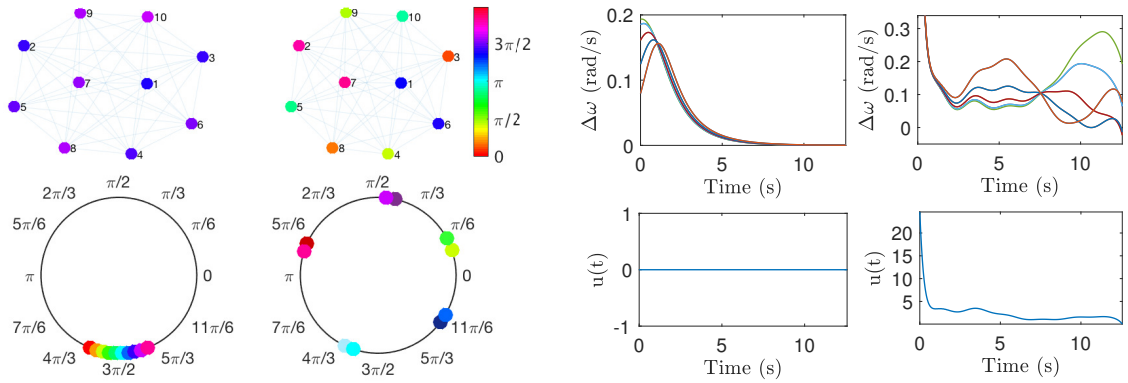

(a) (b)

Figure 3.7: Phase clustering in a globally coupled network of Kuramoto oscillators. (a) Phase distributions on shown on the networks and the unit circles. The top and bottom figures on the left panel show the phase of the uncontrolled network (phase lock), whereas in the right panel a control signal was applied (phase clustering). (b) The left panel shows the frequency differences between oscillators with no control is applied, $u(t) = 0$. The top right figure shows the frequency differences when the control signal in the bottom right is applied.

Even though the proposed algorithm can synthesize control inputs to create an arbitrary number of clusters in a network of n oscillators governed by (3.12), there are some phase assignments that are not feasible. In the following, we analyze the controllability properties of (3.12) and give the set of points that can be reached in T unit of time. To fix the idea, we consider a chain network of three Kuramoto oscillators. The dynamics are described by

$$\begin{aligned}
\dot{\theta}_1 &= \omega_1 + \sigma[\sin(\theta_2 - \theta_1)] + b_1 u(t), \\
\dot{\theta}_2 &= \omega_2 + \sigma[\sin(\theta_1 - \theta_2) + \sin(\theta_3 - \theta_2)] + b_2 u(t), \\
\dot{\theta}_3 &= \omega_3 + \sigma[\sin(\theta_2 - \theta_3)] + b_3 u(t),
\end{aligned} \tag{3.14}$$

where σ represents the coupling strength and $u(t)$ is the control input. If the input gains b_1, b_2 and b_3 are equal, and furthermore, the natural frequencies ω_1, ω_2 and ω_3 are equal, this network is not controllable. Therefore, we will consider the case where these parameters are not equal and assign them numerical values to simplify and increase the readability of the Lie brackets.

Let, for example, $b_1 = 0.8, b_2 = 1, b_3 = 1.2$ and $\omega_1 = 1, \omega_2 = 1.1, \omega_3 = 1.2$. We can show by computing the Lie brackets of the vector fields $f(\Theta)$ and $g = (b_1, b_2, b_3)'$ that there exist some points, $\Theta = (\theta_1, \theta_2, \theta_3)' \in \mathbb{R}^3$, at which $\mathcal{M} = \{f, ad_f^k g\}$, $k \in \mathbb{Z}^+$, does not span $\mathbb{R}^3$. In fact, for every point $\Theta^* = (\theta_1, \theta_2, \theta_3)'$, such that $\theta_2 = \theta_1 + qk\pi$ and $\theta_3 = \theta_2 + qk\pi$, $q \in \mathbb{Q}$, the rank of $\mathcal{M}$ is $2 < n = 3$. In other words, $\text{rank}(\mathcal{M}) = 2$ for every $\Theta \in \mathcal{S} = \{\Theta = (\theta_1, \theta_2, \theta_3)' : (\theta_2 - \theta_1) = (\theta_3 - \theta_2), \mod 2\pi\}$. On the other hand, the rank of $\mathcal{M}$ is 3 at every points $\Theta \notin \mathcal{S}$. To illustrate this calculation, here we compute the first and second Lie brackets, where the first one is defined as $ad_f^1 g(\Theta) = [f, g](\Theta) = \frac{\partial g}{\partial x} f - \frac{\partial f}{\partial x} g$. With the vector field f and g given in (3.14), we obtain

$$ad_f^1 g = \frac{\sigma}{5} \begin{bmatrix} -\cos(\theta_1 - \theta_2) \\ \cos(\theta_1 - \theta_2) - \cos(\theta_2 - \theta_3) \\ \cos(\theta_2 - \theta_3) \end{bmatrix}, \tag{3.15}$$

and

$$ad_f^2 g = \begin{bmatrix} \frac{\sigma^2 \cos(\theta_1 - 2\theta_2 + \theta_3)}{5} - \frac{2\sigma^2}{5} - \frac{\sigma \sin(\theta_1 - \theta_2)}{50} \\ \frac{\sigma(\sin(\theta_1 - \theta_2) - \sin(\theta_2 - \theta_3))}{50} \\ \frac{2\sigma^2}{5} - \frac{\sigma^2 \cos(\theta_1 - 2\theta_2 + \theta_3)}{5} + \frac{\sigma \sin(\theta_2 - \theta_3)}{50} \end{bmatrix}. \tag{3.16}$$

Let $\mathcal{M} = \{f, [f,g], [f,[f,g]]\}$ and take the coupling $\sigma = 1$. Evaluating this matrix at $\Theta^* = (\theta_1, \theta_1 + \pi, \theta_1)'$, where $\theta_1 = 2k\pi$, $k \in \mathbb{N}$, yields

$$\mathcal{M} = \begin{bmatrix} 1.0 & 0.2 & -0.2 \\ 1.1 & 0 & 0 \\ 1.2 & -0.2 & 0.2 \end{bmatrix}, \tag{3.17}$$

which is a matrix with rank = 2, hence the point Θ^* is not reachable from every initial condition $\Theta(0) = \Theta_0$ in arbitrarily small time $T > 0$. A similar calculation for the point $\Theta_0 = (\theta_1, \theta_2, \theta_3)'$, where $\theta_1 = \theta_2 = \theta_3$, results in a matrix $\mathcal{M}_0$ that has rank = 2 as well. Given that the Lie brackets generated by the vector fields f and g do not span $\mathbb{R}^3$ at generic points, we cannot conclude that this network is controllable. We did not show the higher order brackets here given that they do not generate new directions in which the solution can move. Despite the drift term $f(\Theta)$ being recurrent, and rank$(\mathcal{M})$ = 3 at points $\Theta \notin \mathcal{S}$, this system is not even locally exact time controllable [145] at every point satisfying the Lie algebra rank condition [26].

Indeed, we can further show that for the system in (3.14), when the coupling strength $\sigma = 0$, any solution $\Theta(t) = (\theta_1(t), \theta_2(t), \theta_3(t))$ of the differential equation system must satisfy

$$\psi_{32}(T) - \frac{\beta_{32}}{\beta_{21}}\psi_{21}(T) = \psi_{32}(0) - \frac{\beta_{32}}{\beta_{21}}\psi_{21}(0) + \left(\Omega_{32} - \frac{\beta_{32}}{\beta_{21}}\Omega_{21}\right)T, \tag{3.18}$$

where $\psi_{ji} = \theta_j - \theta_i$, $\Omega_{ji} = \omega_j - \omega_i$ and $\beta_{ji} = b_j - b_i$. Considering the same numerical values as before, this equation further simplifies to

$$\psi_{32}(T) - \psi_{21}(T) = \psi_{32}(0) - \psi_{21}(0). \tag{3.19}$$

Equation (3.19) implies that there are points that cannot be reached in exactly time T, whether or not these points satisfy the Lie algebra rank condition. As a matter of fact, starting from the initial condition $\Theta(0) = (0,0,0)'$ only phase assignments corresponding to equal phase differences ($\psi_{32} = \psi_{21}$) can be achieved. Hence, only points in $\mathcal{S}$ are reachable from the origin. For any other desired phase difference, the initial and final states need to satisfy (3.19). The condition given by (3.19) also holds for the weakly coupled networks i.e., $0 < \sigma \ll \sigma_c$.

The Kuramoto phase model network with a constant input matrix $B = (b_1, \cdots, b_n)'$ is not fully controllable with a common control $u(t)$, as a result only a few phase patterns can be realized. Furthermore, these patterns have to satisfy (3.19), which reduces the encoding capacity of the network. Given the limited number of feasible phase patterns, a large number of oscillators will be required in order to increase the network encoding capacity or information processing capability. The loss of controllability in real networks could potentially have detrimental consequences, e.g., in the brain neural network, this could lead to a loss of brain functions due to the inability of the neural network to reproduce the precise spiking pattern that contains the necessary information. During seizure episodes, for example, patterns of synchronized neurons appear and normal brain functions are strongly perturbed.

Chapter 4

Phase Modeling of Thermostatically Controlled Loads for Demand Response

With the advent of smart grid technologies and the integration of RESs in distribution systems around the world, system operators will now have to rely on demand response (DR) and ancillary services (AS) to balance supply and demand of energy more than ever before. It is therefore imperative to develop technologies that can exploit the resources available for DR to the fullest extent. Indeed, a significant portion of electricity consumed worldwide is used to power thermostatically controlled loads (TCLs) such as air conditioners, refrigerators, and water heaters. Because the short-term timing of operation of such systems is inconsequential as long as their long-run average power consumption is maintained, they are increasingly used in DR programs to balance supply and demand on the power grid [80, 33, 78, 79].

In this chapter, we present an *ab initio* phase model for general TCLs, and use the concept to develop a continuous oscillator model of a TCL and compute its phase response to changes in temperature and applied power. This yields a simple control system model that can be used to evaluate control policies for modulating the power consumption of aggregated loads with parameter heterogeneity and stochastic drift. We demonstrate this concept by comparing simulations

of ensembles of heterogeneous loads using the continuous state model and an established hybrid state model. The developed phase model approach is a novel means of evaluating DR provision using TCLs, and is instrumental in estimating the capacity of ancillary services or DR on different time scales. As a proof of concept, we propose a novel phase response based open-loop control policy that effectively modulates the aggregate power of a heterogeneous TCL population while maintaining load diversity and minimizing power overshoots. Control policies that can maintain a uniform distribution of power consumption by aggregated heterogeneous loads will enable distribution system management (DSM) approaches that maintain stability as well as power quality, and further allow more integration of renewable energy sources. The main ideas of this chapter were initially developed in [35].

4.1 Thermostatically Controlled Load Models

In this section, we introduce a novel application of phase modeling to TCLs that will facilitate the analysis of the behavior of heterogeneous TCL populations as well as the design and evaluation of control policies for providing effective demand response (DR) services. As we have seen in Chapter 3, phase reduction theory allows one to reduce a high-dimensional oscillating system to a simple one-dimensional phase equation that simplifies the design of control policies and facilitates the analysis of the system. Starting with a one-dimensional hybrid state model of the TCL in Section 4.1.1, our first step is to develop the two-dimensional continuous state model given in section 4.1.3. This is necessary because the computation of phase model parameters, namely, the natural frequency and phase response curve (PRC), using the adjoint method [128] requires a continuous dynamical system. The resulting phase model will be particularly important for

studying temporary synchronization of TCLs that often affects the quality and capacity of ancillary services provided by a Balancing Authority (BA) [33, 34].

4.1.1 One-Dimensional Hybrid Model

The dynamics of the internal temperature $\vartheta(t)$ of a house equipped with an air-conditioning (AC) system is often described using a simple hybrid-state model [146]. The model describes how an AC unit regulates the average temperature by means of a thermostat and a relay with state $s(t) \in \{0,1\}$ [147]. The hybrid state model describing the evolution of the internal temperature $\vartheta(t)$ is given by

$$\dot{\vartheta}(t) = -\frac{1}{RC}\left(\vartheta(t) - \vartheta_a + s(t)PR\right), \tag{4.1}$$

$$s(t) = \begin{cases} 0 & \text{if } \vartheta(t) < \vartheta_{\min} \\ 1 & \text{if } \vartheta(t) > \vartheta_{\max} \\ s(t) & \text{otherwise,} \end{cases} \tag{4.2}$$

where ϑ_a represents the ambient temperature (ϑ_a will be considered constant here), P is the average energy transfer rate of the TCL in the on state, C and R are the thermal capacitance and resistance of the building, respectively. The allowed minimum and maximum temperature of the TCL are $\vartheta_{\min} = \vartheta_s - \delta_b/2$ and $\vartheta_{\max} = \vartheta_s + \delta_b/2$, respectively, with ϑ_s the thermostat temperature set-point and δ_b the deadband. For a population of n TCLs, with temperature states $\vartheta_i(t)$ for $i \in \{1, \cdots, n\}$ that evolve according to (4.1), the aggregate power $P_{\text{agg}}(t)$ drawn by all n TCLs is [148]

$$P_{\text{agg}}(t) = \sum_{i=1}^{n} \frac{1}{\eta_i} s_i(t) P_i, \tag{4.3}$$

where η_i is the coefficient of performance of each TCL unit.

4.1.2 Ab Initio Deterministic TCL Phase Model

We formulate a basic model of a TCL as a deterministic switched oscillating system, whose state is given by the temperature $\vartheta \in [\vartheta_{\min}, \vartheta_{\max}]$ and the switching function $s \in \{\text{off}, \text{on}\}$. Suppose without loss of generality that the system is an air conditioner that cycles through a duty cycle to maintain a temperature $\vartheta_s = (\vartheta_{\max} - \vartheta_{\min})/2$ while remaining within the deadband $\delta_b = \vartheta_{\max} - \vartheta_{\min}$. We denote the beginning of the cycle as the point $(\vartheta, s) = (\vartheta_{\max}, \text{on})$ just after the unit has turned on. The state of the unit changes according to $\dot{\vartheta} = r_- < 0$ when the unit is at $s = \text{on}$, then it switches to $s = \text{off}$ when the state reaches $\vartheta = \vartheta_{\min}$. Subsequently, the state of the unit changes according to $\dot{\vartheta} = r_+ > 0$ until it reaches $\vartheta = \vartheta_{\max}$, and the unit turns on again. Let T_{on} and T_{off} be the lengths of time when the unit is on and off, respectively, so that the period of oscillation is $T = T_{\text{on}} + T_{\text{off}}$.

Our goal is to map this behavior to a phase model, as illustrated in Figure 4.1. Such models are desirable because the homogeneous dynamics are linear and scalar. The state is represented by a scalar phase ϕ, which advances linearly with time according to a frequency $\omega = 2\pi/T$. For an unforced system, this yields a simple solution $\phi = \omega t \pmod{2\pi}$. Thus, we map the state point $(\vartheta_{\max}, \text{on})$ where the unit turns on to the phase point $\phi = \phi_{\text{on}} \equiv 0$, and the state point $(\vartheta_{\min}, \text{off})$ where the unit turns off to the phase point $\phi = \phi_{\text{off}}$. This yields a continuous representation of the switched system.

To complete the picture, we first determine the phase $\phi_{\text{off}} \in [0, 2\pi)$ when the unit switches off. If $r_+ = r_-$, then it is straightforward to show that $\phi_{\text{off}} = \pi$. However, most units will have different values of r_+ and r_-, which will also depend on other factors such as the ambient temperature.

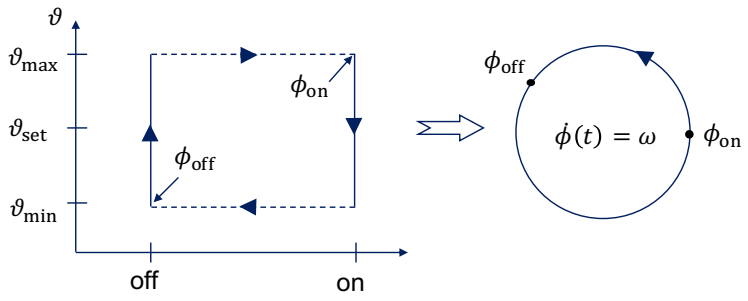

Figure 4.1: Phase model of a switched oscillating system.

Suppose then that $r_+ \neq r_-$, and let us denote the rate ratio, which is equivalent to the duty ratio, by

$$\gamma = -\frac{r_-}{r_+} = \frac{T_{\text{off}}}{T_{\text{on}}}. \tag{4.4}$$

It is straightforward to show that these ratios are equivalent. Integrating the $s = \text{on}$ dynamics $\dot{\vartheta} = r_-$ from $t = 0$ to $t = T_{\text{on}}$ yields

$$r_- T_{\text{on}} = \theta_{\min} - \vartheta_{\max} = -\delta_b, \tag{4.5}$$

and integrating the $s = \text{off}$ dynamics $\dot{\vartheta} = r_+$ from $t = T_{\text{on}}$ to $t = T = T_{\text{on}} + T_{\text{off}}$ yields

$$r_+ T_{\text{off}} = \vartheta_{\max} - \vartheta_{\min} = \delta_b. \tag{4.6}$$

Then, equation (4.4) follows directly from (4.5) and (4.6), and we then have $\gamma > 0$, and $T_{\text{off}} = \gamma T_{\text{on}}$. We can then compute T_{on} and T_{off} according to

$$\begin{aligned} T_{\text{on}} &= T - T_{\text{off}} = T - \gamma T_{\text{on}} = \frac{1}{1+\gamma} T = \frac{r_+}{r_+ - r_-} T, \\ T_{\text{off}} &= T - T_{\text{on}} = T - \frac{1}{1+\gamma} T = \frac{\gamma}{1+\gamma} T = \frac{-r_-}{r_+ - r_-} T. \end{aligned} \tag{4.7}$$

It follows that the switch-off phase is given by

$$\phi_{\text{off}} = \frac{2\pi}{T} T_{\text{on}} = 2\pi \frac{r_+}{r_+ - r_-} = 2\pi \frac{T_{\text{on}}}{T_{\text{on}} + T_{\text{off}}}. \tag{4.8}$$

It is straightforward to show that the parameters in the hybrid-state model given in equations (4.1)-(4.2) are related to the phase model parameters [149] by

$$T_{\text{off}} = RC \ln \left(\frac{\vartheta_{\text{a}} - \vartheta_{\text{min}}}{\vartheta_{\text{a}} - \vartheta_{\text{max}}} \right) \tag{4.9}$$

and

$$T_{\text{on}} = RC \ln \left(\frac{\vartheta_{\text{max}} - \vartheta_{\text{a}} + PR}{\vartheta_{\text{min}} - \vartheta_{\text{a}} + PR} \right), \tag{4.10}$$

with the period given by

$$T = RC \ln \left(\frac{(\vartheta_{\text{a}} - \vartheta_{\text{min}})(\vartheta_{\text{max}} - \vartheta_{\text{a}} + PR)}{(\vartheta_{\text{a}} - \vartheta_{\text{max}})(\vartheta_{\text{min}} - \vartheta_{\text{a}} + PR)} \right). \tag{4.11}$$

Hence, we can express the switch-off phase by

$$\phi_{\text{off}} = 2\pi \frac{\ln \left(\frac{\vartheta_{\text{max}} - \vartheta_{\text{a}} + PR}{\vartheta_{\text{min}} - \vartheta_{\text{a}} + PR} \right)}{\ln \left(\frac{(\vartheta_{\text{a}} - \vartheta_{\text{min}})(\vartheta_{\text{max}} - \vartheta_{\text{a}} + PR)}{(\vartheta_{\text{a}} - \vartheta_{\text{max}})(\vartheta_{\text{min}} - \vartheta_{\text{a}} + PR)} \right)}. \tag{4.12}$$

Note that to control the average power of a TCL, one needs to modulate the duty cycle of the power utilization. This is equivalent to controlling the phase ϕ_{off} of the phase model illustrated in Figure 4.1, assuming for instance that $\phi_{\text{on}} = 0$ is the reference phase.

4.1.3 Continuous Representation of Switching Dynamics

We now present a two-dimensional continuous state-space model that approximates the dynamics of the internal temperature of a TCL unit and the thermostat switching. This is an important step that precedes the derivation of the complete phase model, which will require the computation of the phase response curve (PRC) of the continuous oscillator model. Subsequently, we will examine the phase response of the temperature dynamics to control action applied to the TCL.

Consider the evolution of the temperature $\vartheta(t)$ (see Figure 4.2(a)) described by (4.1), and the corresponding phase portrait in Figure 4.2(c), simulated with the parameters provided in Table 4.1 [87]. Observe that the unperturbed behavior of a TCL is similar to that of an oscillator with a stable limit cycle.

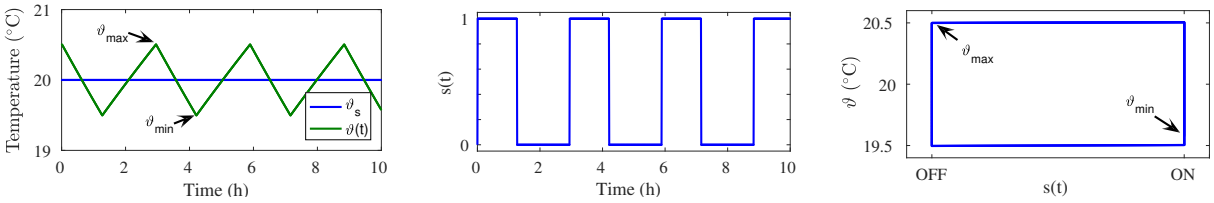

(a) TCL temperature (b) Switching function (c) Limit cycle

Figure 4.2: Simulation of the hybrid model (4.1)-(4.2) with the parameters in Table 4.1 and the deadband $\delta_b = 1.0°\text{C}$. (a) Evolution of the temperature $\vartheta(t)$ around the set-point $\vartheta_s = 20°\text{C}$. (b) Thermostat switching function $s(t)$. (c) Phase portrait of $\vartheta(t)$ *vs.* $s(t)$.

The hybrid-state nature of the system described by (4.1) and (4.2) is due to the thermostat switching function $s(t)$ that transitions between 0 and 1 states. Therefore, modeling the behavior of a TCL using continuous states requires a continuous approximation of the switching function $s(t)$ and its dynamics. Ideally, the evolution of the temperature and the continuous switching function could be represented using a system of two coupled differential equations that has a stable limit cycle similar to the one shown in Figure 4.2(c). Our motivation for the proposed model is the Van der

Table 4.1: Nominal TCLs parameter values

Parameter	Meaning	Value
ϑ_s	temperature set-point	20°C
ϑ_a	ambient temperature	32°C
δ_b	thermostat deadband	0.5°C
R	thermal resistance	2°C/kW
C	thermal capacitance	10 kWh/°C
P	energy transfer rate	14 kW
η	coefficient of performance	2.5

Pol oscillator, which is a simple model of the limit cycle observed in circuits with vacuum tubes. More so, a similar phase portrait is observed in the FitzHugh-Nagumo model, which is a simple mathematical description of the firing dynamics of a neuron [128]. Inspired by these examples, we propose the continuous-state TCL model given by

$$\begin{aligned} \dot{x}(t) &= \mu\left((\frac{\delta_b}{2}+\varepsilon)x - \frac{x^3}{3} + \vartheta - \vartheta_s\right), \\ \dot{\vartheta}(t) &= -\frac{1}{RC}\left(\vartheta - \vartheta_a + \bar{s}(t)PR\right), \end{aligned} \tag{4.13}$$

where $x(t)$ is the state variable of the switching function, $\vartheta(t)$ the internal temperature, and $\bar{s}(t)$ is an approximation of the ideal switching function $s(t)$. The parameter ε was introduced to compensate for the reduction of the effective deadband in (4.13). The constant μ is a damping parameter that controls the oscillation frequency for a fixed time constant $\tau = RC$ as well as the shape of the phase portrait. Similar to the Van der Pol oscillator, limit cycles with circular and rectangular-like shapes are observed at small and larger values of μ, respectively. Hence, in order for (4.13) to have a limit cycle similar to the one shown in Figure 4.2(c) while oscillating approximately at the same frequency as (4.1), we chose $\mu = 100$.

Once the value of μ is fixed, the small difference in the deadband that translates into frequency deviation can be compensated for by the parameter $\varepsilon < \delta_b$. The parameter ε can quickly be determined through numerical simulations as follows. Knowing that $\varepsilon \in [0, \delta_b)$, one can sample n values of ε over this interval, simulate the dynamics (4.13) for each value of ε, and then compare the oscillation frequencies at each value to the nominal frequency of the hybrid state model in (4.1) to determine the most appropriate value of ε. This is only done once using the TCL with a natural frequency corresponding to the average frequency of the population of TCLs considered. For the parameters in the Table 4.1, $\varepsilon = 0.1454$.

Finally, the continuous switching function $\bar{s}(t)$, that is similar to the switching function $s(t)$, is obtained from the variable $x(t)$ by using of a continuous approximation of the Heaviside step function. Similar usage of the continuous step function is found in the Morris-Lecar model, whose behavior is similar to the Hodgkin-Huxley spiking neuron model [125]. The resulting switching function approximation is given by

$$\bar{s}(t) = \frac{1}{2}\left(1 + \tanh(kx)\right), \tag{4.14}$$

where the parameter $k \in [5, 10]$ controls the sharpness of the switching action. As shown in Figure 4.3(d), the phase portrait is similar to that of the hybrid-state model shown in Figure 4.2(c).

The model given in (4.13) reproduces the dynamical behavior of the hybrid-state model in (4.1). However, our goal is to design an ensemble control of a TCL population such that the aggregate power closely tracks a given reference power. Therefore, we modify the model in (4.13) by substituting for the state variable $x(t)$ with the instantaneous power variable $y(t)$. The derivation of this

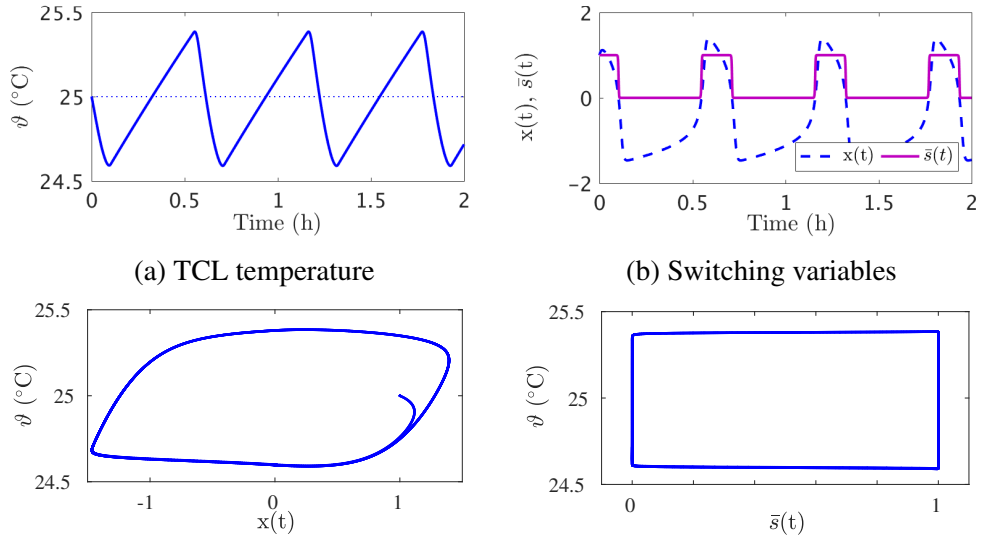

(a) TCL temperature

(b) Switching variables

(c) Limit cycle, $\vartheta(t)$ *vs.* $x(t)$

(d) Limit cycle, $\vartheta(t)$ *vs.* $\bar{s}(t)$

Figure 4.3: Simulation of the system in (4.13). (a) Evolution of temperature $\vartheta(t)$ around the set-point $\vartheta_s = 25°\text{C}$. (b) The switching state variable $x(t)$, and the switching function $\bar{s}(t)$. (c, d) Limit cycles for both $\vartheta(t)$ *vs.* $x(t)$ in (c) and $\vartheta(t)$ *vs.* $\bar{s}(t)$ for the new switching function (4.14) in (d). The parameters used are in Table 4.1, but with $C = 2$ kWh/°C and $\delta_b = 1.0°\text{C}$.

model is provided in Appendix C.1. The resulting model is given by

$$\begin{aligned} \dot{y}(t) &= \mu k \left((\frac{\delta_b}{2} + \varepsilon)\bar{y} - \frac{1}{3}\bar{y}^3 + \vartheta - \vartheta_s \right) (1 - \frac{\eta}{P} y) y, \\ \dot{\vartheta}(t) &= -\frac{1}{CR} (\vartheta - \vartheta_a + \eta y(t) R), \end{aligned} \tag{4.15}$$

where $\bar{y}(t) = -\frac{1}{k}\ln(\frac{P}{\eta y} - 1)$. For a population of n TCLs, the aggregate power is $P_{\text{agg}}(t) = \sum_{i=1}^{n} y_i(t)$. Note that the actual electric power consumed by a TCL is the average energy transfer rate P (in Table 4.1) divided by the coefficient of performance η. The evolution of the TCL's temperature in (4.15), its instantaneous power and the limit cycle are shown in Figure 4.4.

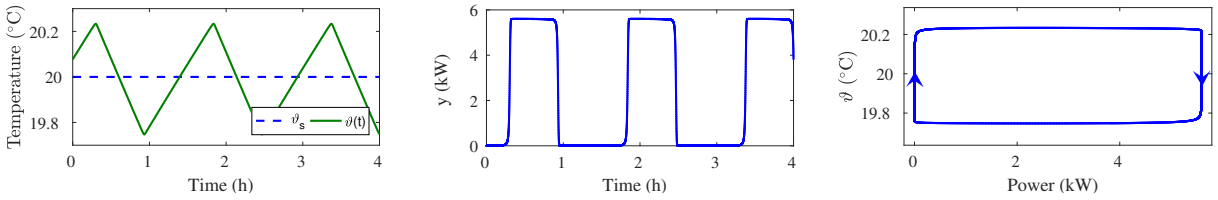

(a) TCL temperature (b) Power variable $y(t)$ (c) Limit cycle

Figure 4.4: Simulation of the continuous TCL system in (4.15). (a) Evolution of the temperature $\vartheta(t)$ around the set-point $\vartheta_s = 20°\text{C}$. (b) Evolution of the electric power $y(t)$ drawn by the TCL. (c) TCL phase portrait. The parameters used are given in Table 4.1.

4.1.4 TCL Phase Model

In Section 4.1.2, we have shown that the unforced cycling dynamics of a TCL can be represented by a phase model $\dot{\phi} = \omega$, where ω is the natural frequency. However, in the presence of an external control input $u(t)$, the phase model takes the form

$$\frac{d\phi}{dt}(t) = \omega + Z(\phi)u(t), \tag{4.16}$$

where $Z(\phi)$ is the phase sensitivity function, also known as phase response curve (PRC), which quantifies the changes in the phase variable in response to an impulse $I(t)$, and $u(t)$ is the external forcing input [128]. For both continuous models (4.13) and (4.15), the PRCs are vectors $Z(\phi) = (Z_s(\phi), Z_\vartheta(\phi))$ and $Z(\phi) = (Z_y(\phi), Z_\vartheta(\phi))$, respectively, where $Z_s(\phi)$, $Z_y(\phi)$ and $Z_\vartheta(\phi)$ are phase sensitivity functions of the switching variable $x(t)$, the instantaneous power $y(t)$, and the temperature $\vartheta(t)$, respectively (see Figure 4.5). Because we are only interested in controlling one state variable of the TCL e.g., the switching $s(t)$ or the power $P(t)$, the PRC in (4.16) will be taken as one of the scalar functions $Z(\phi) = Z_s(t)$ or $Z(\phi) = Z_y(t)$, and the scalar control input will be a temperature signal to offset the set-point. If on the other hand, we were to consider the phase model of the temperature $\vartheta(t)$, the PRC will be $Z(\phi) = Z_\vartheta(t)$ and the corresponding control will be the input power.

The natural frequency is computed as $\omega = 2\pi/T$ using the period T in (4.11) and it is the same for all three variables $s(t)$, $P(t)$ and $\vartheta(t)$. The PRC itself must be computed numerically, using for example the method of the adjoint which requires the computation of the Jacobian of the dynamics of the system described by a continuous function. This method consists of linearizing the system around its periodic orbit $\Gamma(t)$ and solving the adjoint equations with a backward integration [128, 125]. A standard software package used for the computation of the PRC is the XPPAUT [150]. The ability to compute the PRC using the method of the adjoint was one of the reasons for the derivation of the continuous models described in Section 4.1.3. Another important reason for such modeling is the ability to access the switching variable $x(t)$ in (4.13) or the power variable $y(t)$ in (4.15) in order to characterize their dependence on a stimulus $u(t)$. In Appendix C.2, we review some basics of the phase reduction theory as well as different techniques for determining the PRC.

The application of a control input to the phase model (4.16) will either advance or delay the oscillator depending on the phase at which the input is applied. Consequently, the TCL turn-on/off time can be advanced or delayed by ΔT, and therefore, the duty cycle of the TCL power can be modulated. For a heterogeneous TCL population, a common control signal have difference impacts on the TCL phases given that their PRCs are different as shown in Figure 4.5. Note that the PRC of (4.13) looks similar to that of (4.15) except for the amplitude of $Z_s(\phi)$ which is smaller than $Z_y(\phi)$.

4.1.5 Simulation Comparison of TCL Models

In this section, we provide simulation results that are intended to show how well the continuous model (4.15) proposed in Section 4.1.3 approximates the hybrid model dynamics in (4.1)-(4.2). We first compare the phase model in (4.16) to the hybrid-state model in (4.1)-(4.2) by plotting the

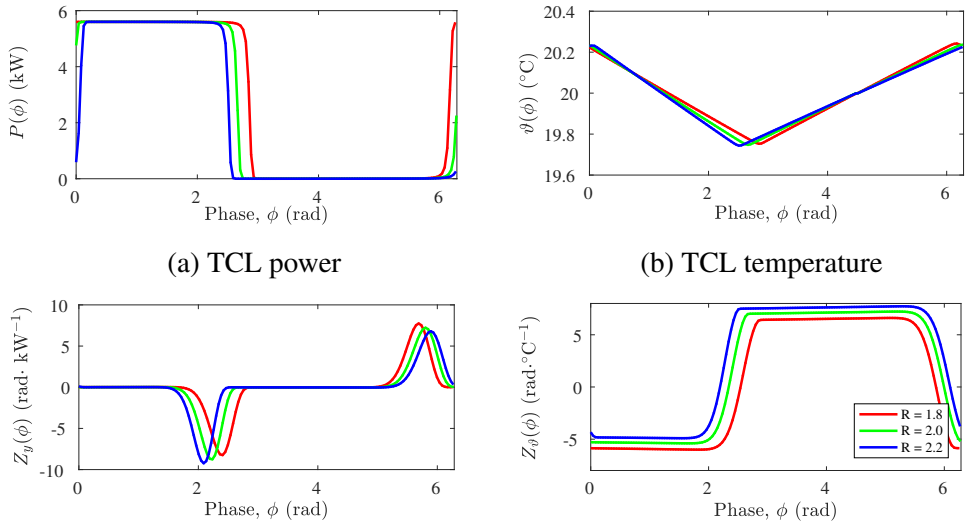

(a) TCL power

(b) TCL temperature

(c) PRC of the TCL power

(d) PRC of the TCL temperature

Figure 4.5: Phase response curves of the power and temperature variables for a range of thermal resistance $R \in [1.8, 2.2]$. (a) and (b) show the power and temperature as a function of the phase ϕ. (c) and (d) show their PRCs $Z_y(\phi)$ and $Z_\vartheta(\phi)$, respectively, for the dynamics in (4.15). The parameters used are shown in Table 4.1.

time evolutions of the phase ϕ and the temperature together in Figure 4.6(a). The phase ϕ_{off} given by (4.12), indicates where the TCL turns off after being on for a time T_{on}. The input powers for both models are shown Figure 4.6(b), with the control $u(t) = 0$.

Second, using the data in Table 4.1, we simulate the aggregate power of 1,000 heterogeneous TCLs for a period of 30 hours. The initial values of temperature and the parameters C, R and P were randomly distributed uniformly within $\pm 5\%$ of their nominal values. The results in Figure 4.6(c) show good agreement between the transient oscillations of both the hybrid and continuous models, and the stationary variation about the long-run mean which occurs after 10 hours appears similar as well.

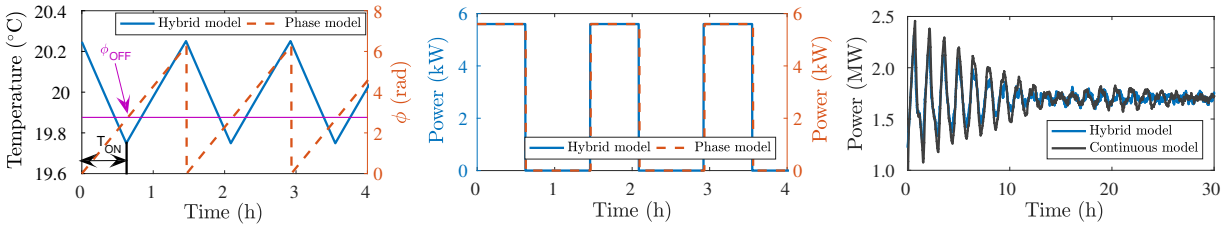

(a) (b) (c)

Figure 4.6: Comparison between the Hybrid model and its derived phase model representation. (a) Time evolution of the temperature (blue, solid) and the phase evolution (red, dashed). (b) Time evolution of the power consumed by the TCL for both models. Note that the TCL turns off exactly after being on for time $t = T_{\text{on}}$ and the switching phase is ϕ_{off}. (c) Aggregate power of 1000 heterogeneous TCLs described by the hybrid and continuous models (4.1) and (4.15), respectively. Simulated with the parameters in Table 4.1.

Now that we have shown that the phase model (4.16) captures the cycling dynamics of a TCL with sufficient accuracy, in the next section we derive a PRC-based control policy and analyze the synchronization properties of TCLs' phase model representations.

4.2 PRC-Based Control Policy

Direct control of TCLs by the Balancing Authority can enable regulation of power consumed by such loads on a distribution subsystem over faster time scales than the price response approach allows [151]. In this section, we proposed an open-loop PRC-based control architecture that can regulate the aggregate power of an ensemble of TCLs without the need to establish two-way communication channels between the loads and the BA. Furthermore, using the phase model of TCLs and the concept of Arnold tongues we analyze the synchronization properties of a given population. This analysis allows us to evaluate the capacity of ancillary services that can be provided by the TCLs and more importantly the appropriate time scale. We then demonstrate the tracking of a power regulation signal that has been decomposed in different frequency bands.

4.2.1 Control of a Single TCL

Phase reduction theory has been used in various scientific areas including physics, neural engineering and biology. This powerful technique has enabled the analysis of synchronization properties of limit cycle oscillators [128]. One can find various applications in the literature such as entrainment of chemical oscillator [66, 67], optimal entrainment of neural oscillator ensembles [64, 120] and phase advance or delay in circadian oscillators where light is used as a control input [121]. Most applications of the phase reduction theory consist of either controlling the phase or the frequency of oscillators [152] e.g., controlling the spiking time of neurons [153], and different control techniques have been developed for that purpose [64, 121].

In this section, we introduce a new application of phase model-based control techniques to TCLs. Unlike previous developed control methods that can only control either the phase or the frequency of an oscillator, the approach presented here must appropriately control both the phase and frequency of a TCL in order to modulate the duty cycle of the input power. Hence, this approach will enable the modulation of the TCL average power consumption, during a period of time T, in response to a regulation signal $\xi(t)$. By appropriately switching the TCLs on and off as illustrated in Figure 4.7, one can modulate the aggregate power of an ensemble over a short time scale without impacting the average temperature of the individual units over the long run. The controls used to produce the results in Figure 4.7 are of the forms $u(t) = Z^{+}(\phi)\xi(t)$ and $u(t) = -Z^{-}(\phi)\xi(t)$ for increasing and decreasing the power consumption, respectively, where Z^{+} and Z^{-} represent the positive and negative parts of the switching PRC ($Z_s(\phi)$). Furthermore, the regulation signal $\xi(t) = \mp 0.1^{\circ}$C was used to increase and decrease the power by forcing the TCL to switch either on (Figure 4.7(b)) or off (Figure 4.7(c)) early.

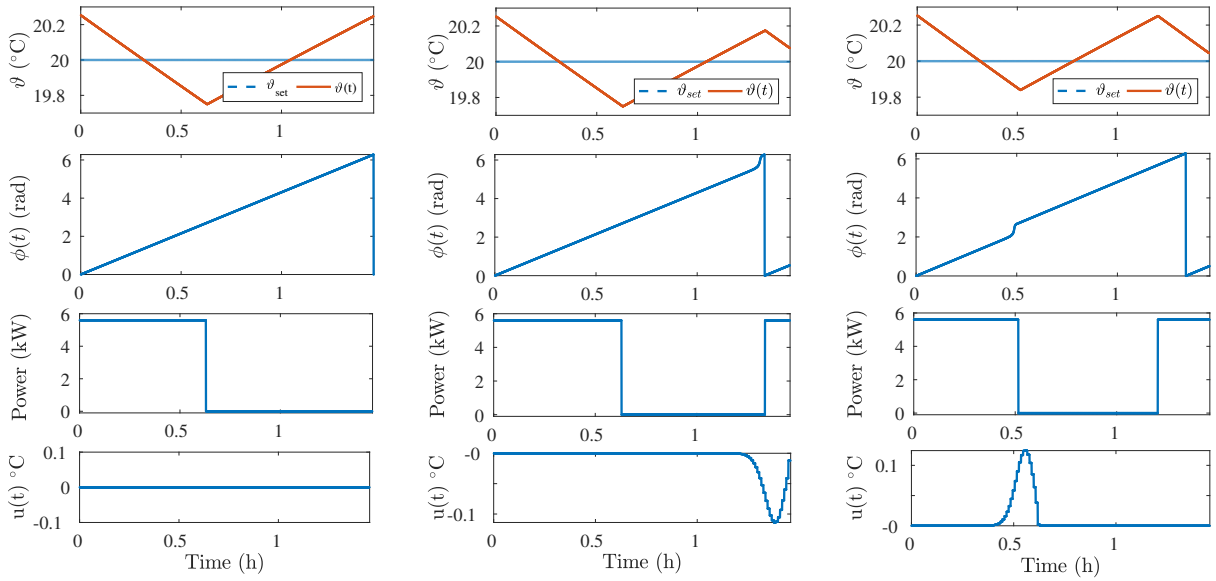

Figure 4.7: Illustration of the phase advances induced by the control input $u(t)$. (a) Unperturbed system $u(t) = 0$. (b) and (c) show the controlled systems. In (b), the control switches the TCL on before its normal turn-on time by temporarily decreasing the set-point. The opposite happens in (c). The first and second rows of plots show the temperatures and their corresponding phases. The third and fourth rows show the corresponding power and control waveforms.

The phase advances induced by $\xi(t)$ in the phase model (4.16) are depicted in the second row of Figure 4.7(b) and (c). By switching a large number of TCLs on, the aggregate power given by (4.3) will instantaneously increase, and conversely switching them off will decrease the aggregate power. It is equally possible to delay the phase which would result in the TCL staying on or off longer than it would have naturally (see Figure 4.8).

4.2.2 Control of an Ensemble of TCLs

One of the main challenges encountered when designing an open-loop control policy for a large population of TCLs is the temporary synchronization that is caused by a sudden change of the

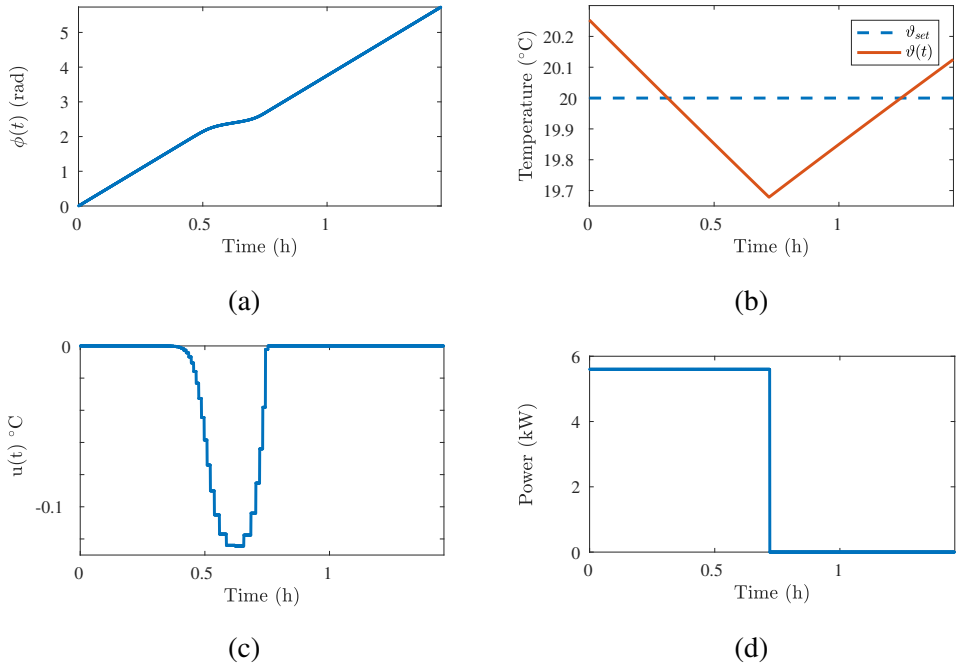

Figure 4.8: Illustration of a phase delay induced by the control $u(t)$. (a) Evolution of the phase $\phi(t)$ showing a slow down (delay) due to the application of the control $u(t) = -Z^{-}\xi(t)$, where $\xi(t) = -0.1°$C. (b) Evolution of the temperature showing that the TCL stays on longer, hence the temperature went below the lower limit of 19.75°C. (c) and (d) show the control input (shift of the set-point temperature) and the TCL power during one period, respectively.

set-point. Although the changes can be small (0.1-0.5°C) and barely noticeable by occupants, they can induce large power fluctuations [87, 154]. Alternatively, such policies can track the aggregate power reference closely when it is relatively slow varying and smooth. The thermostat in this case is assumed to be adjustable with infinitesimally fine precision, although this requirement may be relaxed in practice.

Here, we propose the open-loop control architecture depicted in Figure 4.9, where the local control signal $u(t)$ is generated by a PRC-based controller. The choice of this control architecture is motivated by the needs to suppress two-way communication channels and more importantly, to track a power regulation signal while avoiding or minimizing TCLs synchronization that causes power overshoots. TCLs synchronization is prevented by letting the phase sensitivity functions

dictate the response of each unit to a fast changing regulation signal $\xi(t)$. Note that because of the heterogeneity of the TCLs, the PRCs of all the units in a given population are different. It is assumed that each TCL can measure its state variables (i.e., temperature and switching status) and has knowledge of its own phase sensitivity function $Z(\phi)$. Hence the controller can generate the corresponding control $u(t)$ in response to a global regulation signal $\xi(t)$ from the BA.

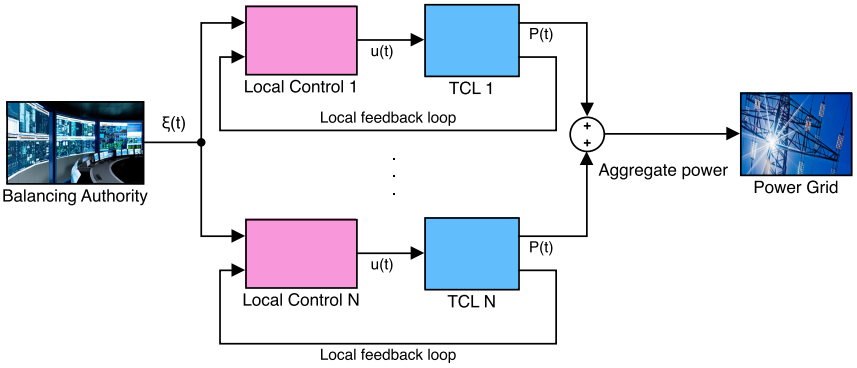

Figure 4.9: Block diagram of the control architecture. The BA regulation signal $\xi(t)$ is sent to all the TCLs in the population. This signal requests that each TCLs changes its power consumption by a given fraction that, if aggregated, will compensate for demand on the power grid. The local controller receives $\xi(t)$ as well as the states of the TCL, then determines the appropriate control input $u(t)$.

The proposed control architecture presents several practical advantages. First, it considerably limits the information complexity required at the Balancing Authority level in the sense that no feedback is required to form the reference signal $\xi(t)$. This also limits the computation and communication costs that would have occurred if feedback was needed. By suppressing the need for a two-way communication, this control policy also addresses privacy concerns [88]. The assumptions that we make on capabilities of the TCL and communication with the BA can be summarized as I) the BA has knowledge of the power utilization of the TCL ensemble and its capacity to service demand response, II) in some instances the BA can totally or partially estimate the aggregate power of the ensemble being controlled, II) each TCL has knowledge of its own PRC and can

measure its internal states, and IV) each TCL is equipped with a control unit and a thermostat that has fine resolution on the deadband.

As a proof of concept, we propose a PRC-based integral controller, and evaluate its performance against a traditional integral controller and the direct control. By direct control, we refer to situations with no feedback and no local controller, in which the signal $\xi(t)$ directly controls the TCL ensemble. We further show its efficacy by tracking a real Area Control Error (ACE) signal taken from the Bonneville Power Administration (BPA) website [155]. The proposed controller is of the form

$$\dot{u}(t) = I_1 \left[I_2 \text{sgn}\left(\tfrac{1}{2} - s(t)\right) Z(\phi)\xi(t) - u(t) \right], \tag{4.17}$$

where *sgn* is the signum function that extracts the sign of $1/2 - s(t)$, I_1 and I_2 are control gains. Discretizing the differential form of the control in (4.17), we arrive at $u(t) = u_k$ for $t \in [t_k, t_{k+1}]$ where

$$u_{k+1} = u_k + I_1 h \left[I_2 \text{sgn}\left(\tfrac{1}{2} - s_k\right) Z(\phi_k)\xi_k - u_k \right], \tag{4.18}$$

where $h = t_{k+1} - t_k$ is the time step, and we have substituted the dependence on the discrete time t_k by the subscript k for simplicity. The control equation (4.18) describes what each local controller in Figure 4.9 is doing when the regulation signal $\xi(t)$ is received. To understand how this control policy is able to track a regulation signal without excessive synchronization of TCL dynamics, observe that $\xi(t)$ enters the control signal through a product with the PRC ($Z(\phi) = Z_y$), which is different from one TCL to another (see Figure 4.5). This implies that each TCL will respond differently according to its own parameters, and more importantly, this response depends on the current phase of the TCL. Without loss of generality, we may assume that at time $t = t_k$, $u_k = 0$ and $\xi_k > 0$, requesting that the TCLs reduce their power consumptions by increasing their set-points by a small fraction of the nominal value. Given the shape of each PRC, the requested change will not be instantaneous for all TCLs. Depending on where the TCLs are on their limit-cycles, some will

switch their status right away while others will do so with a delay that is function of the PRC. The gains I_1 and I_2 control the response time of the controller and the steady state error, respectively. The choice of an integral controller of the form (4.18) was motivated by the desire to minimize higher order harmonics present in the PRCs.

4.2.3 Analysis of Temporary Synchronization in TCL Ensembles

The potential demand response (DR) service that an ensemble of TCLs could provide to a power grid is limited by many factors such as the specified limits for maintaining customer quality of service, the number n of TCLs in the population (the power capacity of a TCL ensemble increases with n), and crucially the frequency bandwidth in which DR can be extracted. Temporary synchronization that causes undesirable fluctuation of the aggregate power is a consequence of the limited bandwidth.

In this section, we provide some useful tools that elucidate the synchronization behavior of TCL ensembles. To fix ideas, observe what happens when a population of TCLs is forced to track a step change in the reference power as shown in Figure 4.10(a). Before the step change is applied at time $t = 5$h, the initial conditions and the finite number of TCLs in the ensemble cause relatively low amplitude oscillations of the aggregate power with a frequency $\omega_0 \approx 1/n \sum_{i=1}^{n} \omega_i$, where the ω_i's are the natural frequencies of the TCLs in the population. Using the wavelet transform, we compute the power spectrum of the aggregate power as a function of time. It appears that the TCL ensemble naturally has damped oscillations with a mean frequency $\omega_0 = 5.69$ rad/h and that a step change at $t = 5$h amplifies these oscillations (Figure 4.10(c)). Observe that by superimposing a decaying sinusoidal signal whose sign is opposed to the step change, the power or amplitude of the oscillations greatly decreases (see Figures 4.10(b) and (d)), which implies that it is possible to

design a control that can change the power usage of the ensemble over a short time scale while minimizing the unwanted oscillations.

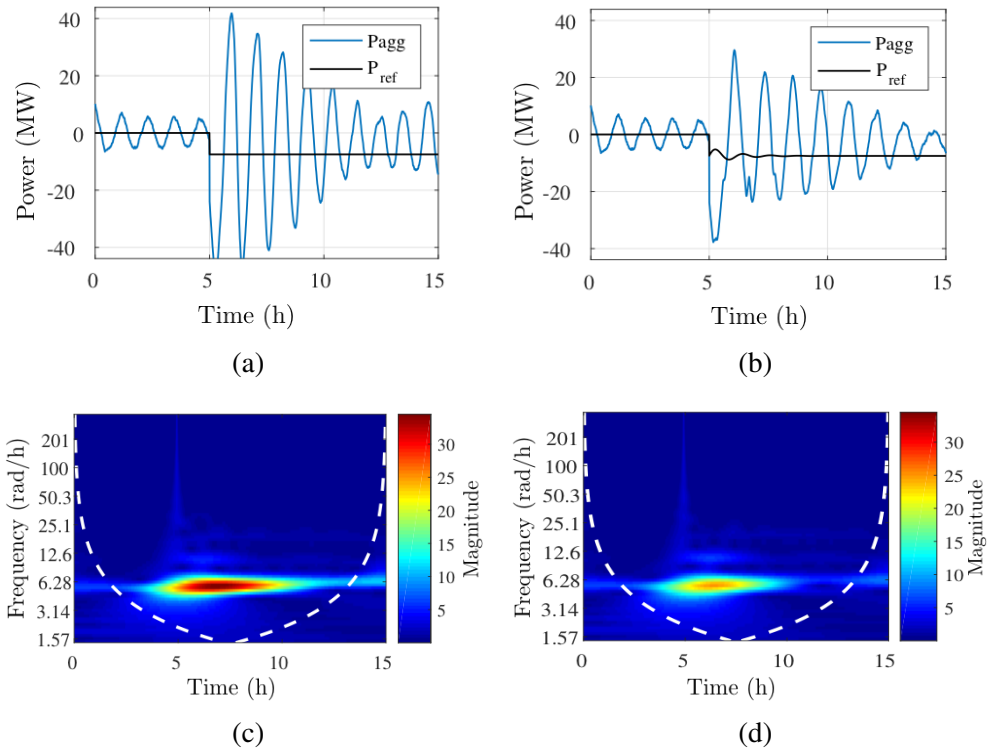

Figure 4.10: Response of a heterogeneous TCL ensemble to a step change in the reference power. (a)-(c) Aggregate power response to a step change and its wavelet transform magnitude scalogram. (b)-(d) Aggregate power response to a step change with an opposing decaying sinusoidal of the same frequency as the induced oscillations. Comparing (c) and (d) reveals that the introduction of a decaying sinusoid with sign opposite the induced oscillation reduces the power content of the undesired oscillations considerably.

It is crucial to note that the step at $t = 5$h behaves like an impulse stimulus whose power content extends over all the frequencies and the population is strongly excited by the frequency closer to its natural mean frequency. It appears as if all the TCLs are now oscillating with the same frequency ω_0 and their phases reset to the same value. This phenomenon is known in the study of rhythmic systems as frequency entrainment [65, 66, 67]. The phase model representation of nonlinear oscillators becomes highly valuable in this case because the phase sensitivity function

$Z(\phi)$ can be used to provide the theoretical linear limits of the entrainment region, commonly referred to as Arnold tongue [156, 157, 158]. For more details see Appendix C.3. An example of Arnold tongues for the TCLs systems considered in this thesis is shown in Figure 4.11.

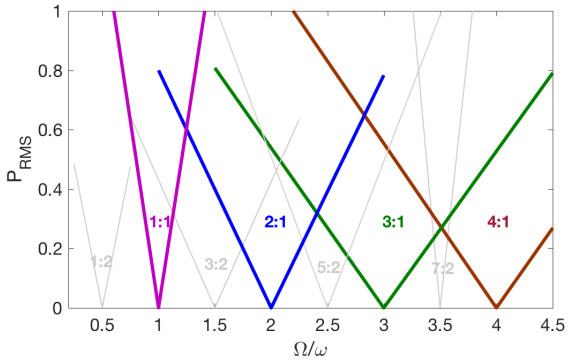

Figure 4.11: Theoretical Arnold tongues of a TCL with frequency ω obtained by driving the system with a sinusoidal input $v(\Omega)$. Theoretical Arnold tongues for a sinusoidal input with frequency Ω applied to one TCL with natural frequency ω. The entrainment ratios are indicated as $N:M$, with $\Omega = N/M\omega$. For this example, the TCL natural frequency is $\omega = 7.95$ rad/h, the parameters in Table 4.1 were used, but with different thermal capacitance $C = 1.8$ kWh/°C and the deadband $\delta_b = 1.5$°C, respectively.

The shape and width of Arnold tongues depend on the PRC and the control input waveform. For entrainment purposes, the control input waveform can be designed to increase the width of the Arnold tongue resulting in a maximum entrainment range [158] or fast entrainment [83]. While maximizing the width of the Arnold tongue is good for entrainment, for control of TCL ensembles it is to be avoided. In Figure 4.12 we have generated Arnold tongues for three different sets of TCL ensembles with different mean frequencies ω_0 by measuring the Root Mean Square Error (RMSE) of the aggregate power tracking with respect to a sinusoidal reference signal with frequency Ω and amplitude A. The tracking error was measured at different power level A and frequency Ω.

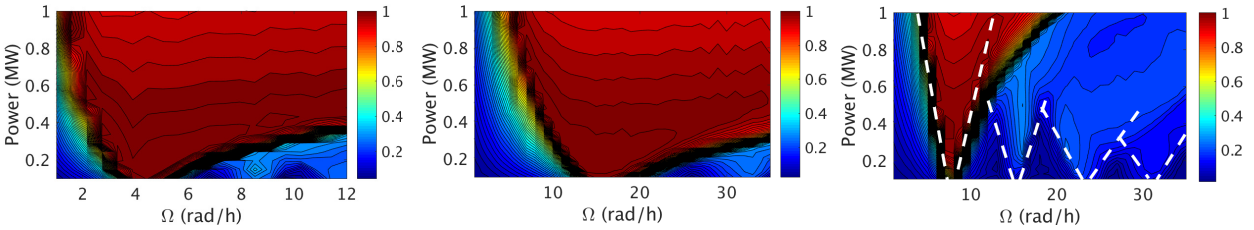

Figure 4.12: Arnold tongues of three different TCL ensembles of 10,000 units obtained by numerical simulations without a controller. The contour maps represent the RMS errors in tracking a sinusoidal input with frequency Ω. (a) The average frequency of the ensemble was $\omega_0 = 4.3$ rad/s with the thermal capacitance $C = 10$ kWh/°C and deadband $\delta_b = 0.5$°C. (b) The average frequency of the ensemble was $\omega_0 = 17.1$ rad/s with the thermal capacitance $C = 2.5$ kWh/°C and deadband $\delta_b = 0.5$°C. (c) The average frequency of the ensemble was $\omega_0 = 7.9$ rad/s with the thermal capacitance $C = 1.8$ kWh/°C and deadband $\delta_b = 1.5$°C. The white dashed-lines correspond to the theoretical Arnold tongues with whole number ratios in Figure 4.11. The power is normalized to 1 MW. The actual peak power was 15 MW.

In Figure 4.12(c), we also drew the theoretical Arnold tongues (white dashed-lines) with whole number ratios that are shown in Figure 4.11; this hence shows that the Arnold tongue corresponding to the 1:1 entrainment region results in the highest tracking error. The 2:1, 3:1 and 4:1 entrainment regions also have relatively high tracking errors. This is because temporary synchronization happens and there are more TCLs turning on or off at the same time than it is needed for tracking a reference. Hence by computing the Arnold tongues one can determine the regions in the power *vs.* frequency (P, Ω) space where the TCLs can provide ancillary services with minimal oscillatory response or better accuracy. Unlike the theoretical bound provided in [159], which suggests that the tracking capacity decreases linearly with frequency, the results presented in this thesis show that this is not entirely the case. Figure 4.12(c) for instance shows that indeed the tracking capacity decreases linearly with the input frequency and reaches its minimum at $\Omega = \omega_0$ but, it increases and decreases again forming bell shapes in the intervals $[\omega_0, 2\omega_0]$, $[2\omega_0, 3\omega_0]$ and $[3\omega_0, 4\omega_0]$. This implies that it is possible to extract responsive regulation from a TCL ensemble at time-scales well beyond the average of natural frequencies of the TCLs by applying an appropriate control

policy that minimizes the area of the Arnold tongue. Example of Arnold tongues of a TCL ensemble controlled with the proportional and integral (PI) controller, and the PRC-based controller are shown in Figure 4.13(a) and Figure 4.13(b). The PI controller reduces the width of the 1:1 Arnold tongue, and the PRC-based controller further reduces it and significantly minimizes its intensity, but the Arnold tongue corresponding to the 1:2 entrainment becomes apparent. This once more confirms that it is possible to obtain significantly more demand response capacity from a given TCL population by using an appropriate controller (or control waveform).

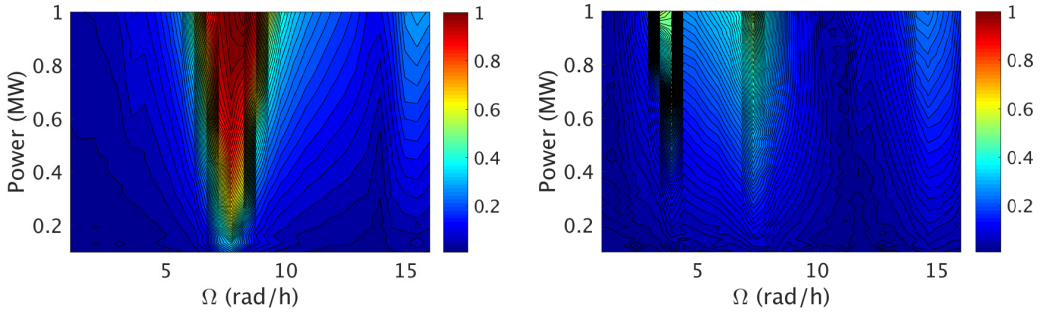

Figure 4.13: Arnold tongues of a TCL ensemble of 10,000 units with controllers. (a) With PI controller. (b) With PRC-based controller. The parameters in Table 4.1 were used with the thermal capacitance $C = 1.8$ kWh/°C and the deadband $\delta_b = 1.5$°C. The power is normalized to 1 MW. The actual peak power corresponds to 15 MW.

4.2.4 Tracking of a Regulation Signal Based on Spectral Decomposition

In this section we demonstrate the tracking of an Area control error signal by using the Arnold tongues in Figure 4.12 to determine the appropriate spectral decomposition to apply to the ACE signal. We identify each TCL ensemble by its mean natural frequency ω_0. The ACE signal to track is shown in Figure 4.14(a) and its wavelet transform is shown in Figure 4.14(b), in which we can see that the dominant frequency is $\omega = 0.59$ rad/h and the second dominant frequency is around $\omega = 2\pi$ rad/h.

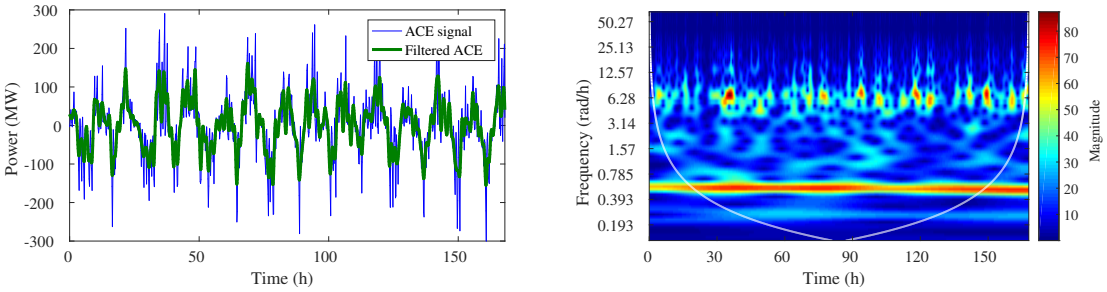

(a) Are control error signal

(b) Magnitude scalogram

Figure 4.14: Area control error (ACE) signal and its power spectrum. The power spectrum was computed using wavelet transform. (a) ACE signal with its lowpass filtered content. The cutoff frequency was 4 rad/h. (b) ACE frequency content vs. time.

The ACE signal contains different frequency components (low and high frequencies) that can be decomposed into different bands so that a certain population of TCLs with a given mean natural frequency is able to accurately track the reference power. In Figure 4.15, we show different groups of TCLs tracking the ACE signal that has been filtered in specific frequency bands identified by their bandwidths (Bw) and scaled such that it can be tracked by the ensemble. Each TCL group is composed of $10,000$ heterogeneous units. For the TCLs with $\omega_0 = 17.1$ rad/h, we show that this group can track low and high frequencies that are contained in the ACE signal (Figures 4.15(d), 4.15(e) and 4.15(f)). In Figure 4.15(g), we show that it is possible to nearly recover the full spectrum of the ACE signal by summing the powers that were tracked in different bands (e.g., the power in Figures 4.15(a), 4.15(b), 4.15(e) and 4.15(f)). Hence, by partitioning a large population of TCLs in different groups based of their capacity to track specific frequency bands, it is possible to provide ancillary services in different time scales.

In Figure 4.16 we show the relative percent error of each group tracking different frequency bands. The relative error is computed as $err(t) = (P_{\text{ref}}(t) - P_{\text{agg}}(t))/P_{\text{ref}}(t) \times 100\%$ around the baseline power P_{base}, which is the average power consumption of 10,000 TCLs. The tracking RMSE (normalized by the average aggregate power) for each case in Figure 4.15 are given in Table 4.2 where

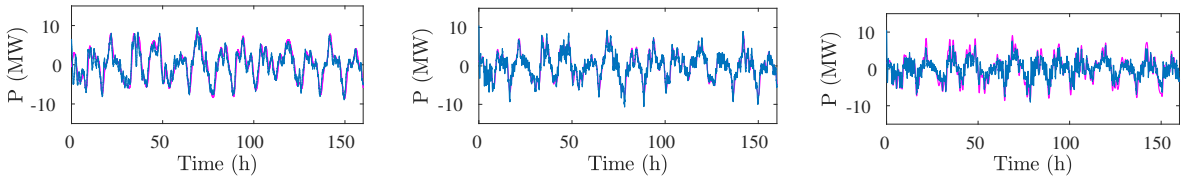

(a) Bandwidth Bw = [0, 2]rad/h. (b) Bandwidth Bw = [0, 3]rad/h. (c) Bandwidth Bw = [0, 4]rad/h.

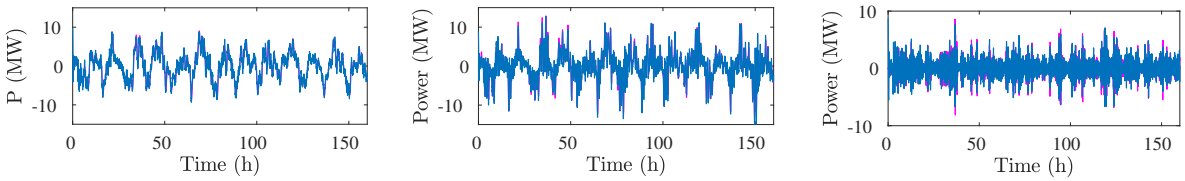

(d) Bandwidth Bw = [0, 4]rad/h. (e) Bandwidth Bw = [0, 8]rad/h. (f) Bandwidth Bw = [23, 25]rad/h.

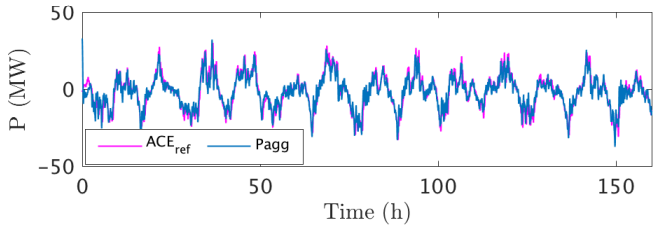

(g) Total power

Figure 4.15: Tracking of the ACE by three different groups of TCL populations with 10,000 units each. The groups are identified by their mean natural frequencies ω_0 corresponding to specific sets of parameters C and δ_b. The rest of the parameters are the same as in Table 4.1. Figures (a) to (f): Power tracking by different TCL populations with the ACE signal filtered in different frequency bands (Bw). (a) TCLs with $\omega_0 = 4.3$ rad/h. (b) TCLs with $\omega_0 = 7.9$ rad/h. (c) TCLs with $\omega_0 = 7.9$ rad/h. (d) TCLs with $\omega_0 = 17.1$ rad/h. (e) TCLs with $\omega_0 = 17.1$ rad/h. (f) TCLs with $\omega_0 = 17.1$ rad/h. (g) The total power P_{agg} is obtained as a sum of the power in (a), (b), (e) and (f). The ACE_{ref} signal is the sum of the filtered ACE signal used in (a), (b), (e) and (f) which almost recovers all the power content of the scaled down original signal in Figure 4.14.

the labeling of TCL groups (a) to (g) corresponds to the labeling used in Figures 4.15 and 4.16.

The RMSE is computed as

$$\text{RMSE } \% = \sqrt{\frac{1}{T}\frac{\int_0^T (P_{\text{ref}}(t) - P_{\text{agg}}(t))^2 dt}{P_{\text{base}}^2}} \times 100.$$

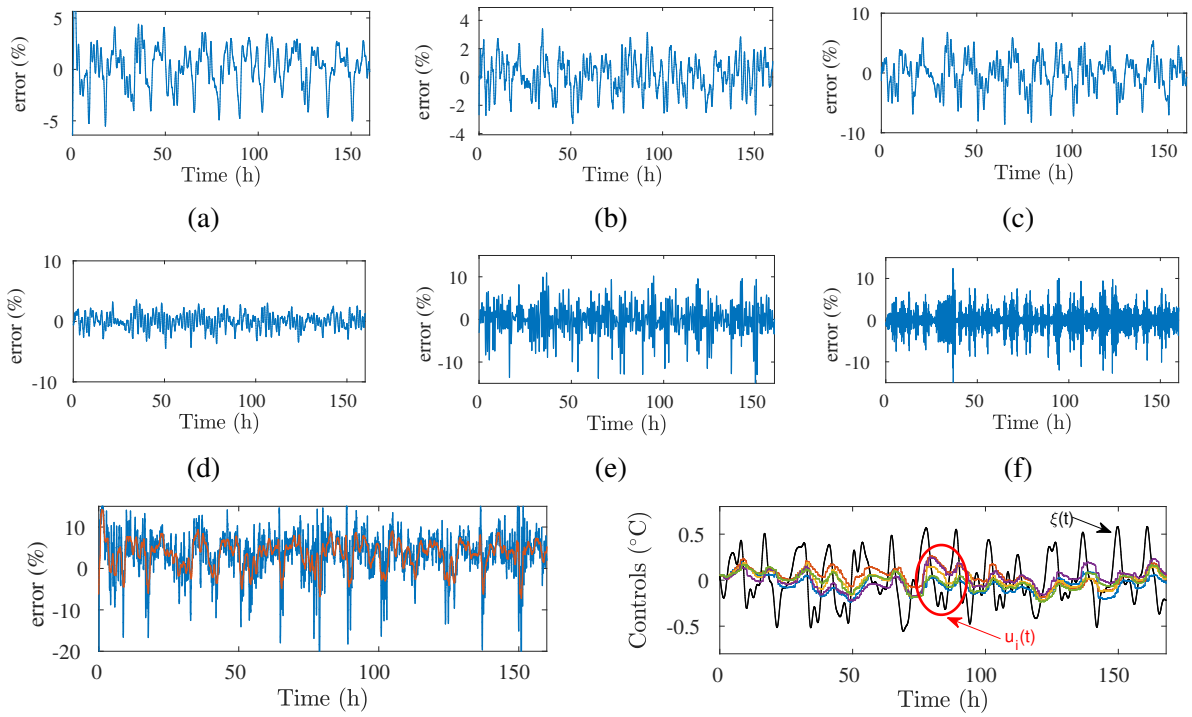

Figure 4.16: Relative tracking errors and sample TCL control inputs. (a) to (g) relative tracking errors corresponding powers in Figure 4.15(a) to Figure 4.15(g). The red line in (g) represents the moving average computed using a sliding window of one hour. This shows that on an hourly average the relative error is less than 10%. (h) Shows the global reference signal $\xi(t)$ sent by the BPA that requests of each TCL to change their power consumptions such that the ACE signal can be tracked. After going through the local controllers (see Figure 4.9), the TCLs control signals $u_i(t)$ are generated.

Table 4.2: Results on the tracking of the ACE regulation signal

TCL groups	(a)	(b)	(c)	(d)	(e)	(f)	(g)
$P_{\max}$ [MW]	10.3	11.2	10.5	9.85	16.5	8.72	39.5
RMSE %	2.31	1.92	3.09	1.38	2.92	3.39	5.89

The results of the numerical experiments that are presented in Figure 4.15, Figure 4.16 and Table 4.2, show that the PRC-based controller performs well in tracking a reference power regulation signal. Before we further discuss these results and assess the tracking errors against previous results in the literature, it is important to note that these numerical experiments confirm the prediction

of the Arnorld tongues in Figure 4.12 that, it is possible to provide DR on a faster time scale than the mean time constant of the TCL population (see Figure 4.15(f)). This has allowed us to provide DR on different time scales and hence, nearly recovering the original ACE signal as shown in Figure 4.15(g), therefore, affirming that the concept of Arnold tongues is a powerful and more accurate tool for evaluating DR than the proposed linear bandwidth limit in [159].

It is remarkable that our controller, which is open-loop (i.e., there is only a one-way communication channel from the BA to the TCLs), achieves good tracking performances, with low tracking errors on the same order of magnitude as the feedback controllers in [87, 160], and actually performs much better than the open-loop controller in [161]. Indeed, the minimum variance control law (MVC) in [87] achieved a tracking relative error of less than 5% with RMSE $< 1\%$. There, the author used 60,000 TCLs (with the same power as in Table 4.1) to track the output of a wind farm with a peak power of approximately 45 MW, which is roughly equivalent to 7.5 MW per 10,000 TCLs, which is less than the peak power considered in Figure 4.15(d) for example, for which we had the lowest RMSE of 1.38%. If we were to consider the same number of TCLs and equivalent power capacity, the performance of our controller would certainly improve. The feedback controller in [160] also achieved an RMSE of $\leq 2.27\%$, whereas, only one of the two feedback controllers in [161] performed slightly better than our controller, with an RMSE of 1.18% while the other controller had an RMSE of 8.7% with a high relative error of 30%. As for the open-loop controllers in [161], they performed poorly with relative errors of up to 50% compared to our PRC-based controller.

Despite not having a feedback loop, our controller achieved good tracking of the ACE signal with reasonably low errors. It is however, possible to increase the performance of our controller with feedback and by optimizing the gains I_1 and I_2 but, this solution is more costly as measurement and transmission equipments will be required to transmit feedback information to the central controller.

Using a feedback control of the form

$$u_{k+1} = u_k + I_1 h \left[I_2 \text{sgn}\left(\tfrac{1}{2} - s_k\right) Z(\phi_k) \left(\xi_k - \xi_k^{P_{\text{agg}}}\right) - u_k \right], \tag{4.19}$$

where $\xi_k^{P_{\text{agg}}}$ is an appropriately scaled regulation signal that depends on the aggregate power, this controller can reduce the error by nearly 50%. For example, the RMSE for the case in Figure 4.15(c) is reduced to 1.8% from 3.1% and its peak relative error is reduced from approximately 8% to 4%.

The comparison above shows that our control policy compares well to several feedback control laws proposed in the literature in terms of reference tracking as well as minimal effect on customer comfort as can be seen from the controls in Figure 4.16(h), where the signals $u_i(t)$ represent the temperature offsets applied to the TCLs set-point temperatures. As one can see in this case the variations of the $u_i(t)$'s are small ($< 0.5^\circ$C), therefore, the TCLs temperature will not significantly deviate from the set-points. With this tracking example, we have demonstrated that it is possible to use TCL ensembles to provide ancillary services at different time scales by tracking low and high frequencies contained in the ACE signal. More interestingly, we arrive at the same observation as in [87], namely, that load populations with smaller thermal time constants are better candidates for providing ancillary services. We confirm this in numerical experiments and, more importantly, by computing the Arnold tongues in Figure 4.12, which demonstrate that the loads with high natural frequency have larger power spectrum bands in which they can provide ancillary services. Considering the tracking errors in Table 4.2, one can see that the TCL population group (d) with the largest ω_0 has the lowest error and that as ω_0 decreases, the error also increases as it can be seen for group (b) and group (a), respectively. Furthermore, for a given TCL population one can see that the tracking error increases as the frequency of the signal to track increases (see groups (d),

(e) and (f), for instance), this is because the signal frequency is getting closer to the entrainment regions (Arnold tongues) that cause synchronization.

The phase modeling approach introduced in this chapter, and in particular the application of Arnold tongues for synchronization analysis, adds new tools to the existing body of work on TCLs and enables a more accurate evaluation of DR capacities on different time scales than previously possible. It will then be possible to a priori determine the specific time scales on which TCLs with given characteristics can be used to provide DR, and the DR capacity that they are able to provide. The impact of these new tools is significant and yet to be explored in depth. In the next chapter, using TCL phase models, we develop a minimum energy control law that can provide accurate demand response while minimizing temperature variations in order to maintain a suitable comfort level inside the building. Finally, by using an open-loop control architecture, we eliminate the need for measuring the states of the TCLs. This has the desirable benefits of addressing customers' privacy concerns, and avoiding the investment cost and technical complications inherent with two-way communication channels.

Chapter 5

A Phase Model-Based Control of Cyclic Loads in Demand Response Programs

In Chapter 4, we introduced the phase model for the general thermostatically controlled load, furthermore, we proposed a novel control paradigm that exploits the TCL phase model. This modeling and control paradigm is also applicable to other periodic or cyclic deferrable loads such as agricultural pumps and swimming pool pumps that can be utilized to provide demand response services [162, 75]. This chapter, without loss of generality, is concerned with the control of heterogeneous TCL populations participating in a DR program. In particular, we present a novel control approach that uses TCL phase models and applies the Pontryagin's maximum [163, 106] to synthesize input signals that can modulate the power consumptions of TCLs to provide DR with minimal impact on consumers' comfort level.

5.1 Control Problem Formulation for TCLs

The phase model is a one-dimensional system with scalar state, and its simplicity has made it one of the most popular models for studying oscillatory systems, including power grids [28] and neural oscillators [125], with particular advantages for control design in the presence of parameter uncertainty [64]. In this section, we use the TCL phase model developed in Chapter 4 to formulate the control problem for regulating the TCL power usage. Thus, we consider the equation describing the evolution of the phase variable, $\phi(t) \in [0, 2\pi)$, subject to an external control input, $u(t)$, that is

$$\frac{d\phi}{dt}(t) = \omega + Z(\phi)u(t), \tag{5.1}$$

where $\omega = 2\pi/T$ is the natural oscillation frequency and $Z(\phi)$ is the phase response curve (PRC) [84, 128, 125]. The frequency ω, or alternatively, the oscillation period T is computed using the TCL parameters in Table 4.1. However, the phase sensitivity function $Z(\phi)$ (see Figure 5.1) is computed numerically, using for example the method of the adjoint, which requires the computation of the Jacobian of the dynamics of the system described by a continuous function, e.g, (4.13).

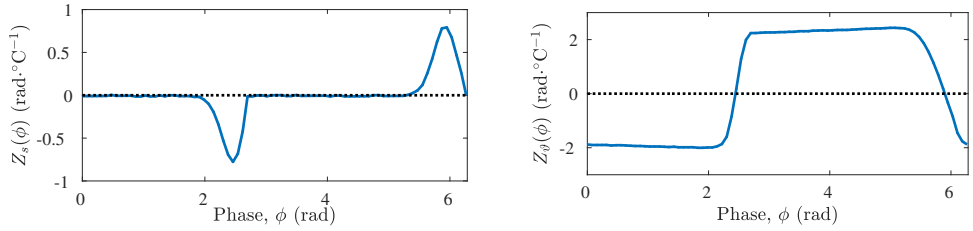

(a) (b)

Figure 5.1: TCL phase response curves. (a) PRC of the switching function $s(t)$. (b) PRC of the temperature $\vartheta(t)$ variable.

5.1.1 Problem Description

We consider the problem of modulating the power consumption of TCLs. This can be achieved by modulating the duty cycle of the switching function, $s(t)$, which is equivalent to controlling the phase ϕ_{off} at which the TCL turns off while maintaining the period, T, constant. The turn-on phase is taken as $\phi_{\text{on}} = 2n\pi$, where $n = 0, 1, 2, \cdots$.

Consider the following optimal control problem:

$$\begin{aligned} \min_{u} \quad & \int_{T_0}^{T_1} u^2(t)dt \\ \text{s.t.} \quad & \dot{\phi} = \omega + Z(\phi)u(t), \\ & \phi(T_0) = \phi_0,\ \phi(T_1) = \phi_{T_1}, \\ & |u(t)| \leq A,\ \forall t \in [T_0, T_1], \end{aligned} \tag{5.2}$$

where $A > 0$ is the bound on the amplitude of the control input $u(t)$. Note that if $T_0 = 0$, $\phi_0 = 0$, $\phi_{T_1} = 2\pi$, and $T_1 \neq T$, where T is the free running period, the optimal control, $u(t)$, will change the oscillation period by $\Delta T = T_1 - T$ [153]. We previously employed this problem formulation to synthesis controls that effectively change the oscillation frequency in experiments with electrochemical oscillators [152].

However, the problem as formulated in (5.2) cannot be used to modulate the duty cycle ($D = T_{\text{on}}/T$) of the TCL. Hence, in the next section we reformulate the optimal control problem such that duty cycle modulation is now possible.

5.1.2 Minimum Energy Control Problem

In order to modulate the duty cycle, we reformulate the optimal control problem in (5.2) to incorporate another boundary condition as

$$\begin{aligned} \min_{u} \quad & \int_{T_0}^{T_1} u^2(t)dt + \int_{T_1}^{T} u^2(t)dt \\ \text{s.t.} \quad & \dot{\phi} = \omega + Z(\phi)u(t), \\ & \phi(T_0) = \phi_0,\ \phi(T_1) = \phi_{\text{off}},\ \phi(T) = 2\pi, \\ & |u(t)| \leq A,\ \forall t \in [T_0, T_1]. \end{aligned} \tag{5.3}$$

We will then derive a piece-wise continuous control, $u(t)$, satisfying the boundary conditions $\phi(T_0) = \phi_0$, $\phi(T_1) = \phi_{\text{off}}$ for $t \in [0, T_1)$ and $\phi(T_1) = \phi_{\text{off}}$, $\phi(T) = 2\pi$ for $t \in [T_1, T)$. The optimal control law is derived using the Pontryagin's maximum principle [106, 164].

Considering the optimal control problem defined in (5.2), we form the control Hamiltonian

$$H = u^2 + \lambda\left(\omega + Z(\phi)u\right), \tag{5.4}$$

where λ is the Lagrange multiplier, which is a solution to the adjoint equation

$$\dot{\lambda} = -\lambda \frac{\partial Z(\phi)}{\partial \phi} u(t). \tag{5.5}$$

The optimality condition from the Pontryagin's maximum principle requires that $\partial H/\partial u = 0$ along the optimal solution. Therefore, we have

$$u(t) = -\frac{1}{2}\lambda Z(\phi). \tag{5.6}$$

Substituting (5.6) for $u(t)$ in (5.5), we obtain

$$\dot{\lambda} = \frac{\lambda^2 Z(\phi)}{2} \frac{\partial Z(\phi)}{\partial \phi}. \tag{5.7}$$

Given that the Hamiltonian is not explicitly dependent on the time t, H is a constant along the optimal trajectory [165]. Hence, we let $H = c, \forall t \in [0, T]$. The Lagrange multiplier λ associated with the optimal solution can then be obtained from (5.4) by substituting (5.6) for $u(t)$ as

$$\lambda = \frac{2\omega \pm 2\sqrt{\omega^2 - cZ^2(\phi)}}{Z^2(\phi)}. \tag{5.8}$$

Note that in the following, we will consider the positive sign in (5.8), which corresponds to forward phase evolution [153]. The optimal phase trajectory can then be obtained from (4.16) after substituting (5.6) for u and (5.8) for λ, as

$$\dot{\phi} = \sqrt{\omega^2 - cZ^2(\phi)}. \tag{5.9}$$

Moreover, the optimal control is given by

$$u(t) = \frac{-\omega + \sqrt{\omega^2 - cZ^2(\phi)}}{Z(\phi)}. \tag{5.10}$$

In addition, by integrating (5.9), we find the target time T_1 in terms of the boundary conditions

$$T_1 = \int_{\phi_0}^{\phi_{T_1}} \frac{1}{\sqrt{\omega^2 - cZ^2(\phi)}} d\phi. \tag{5.11}$$

Therefore, knowing the target time T_1, the initial phase ϕ_0 and final phase ϕ_{T_1}, the constant c in the control law (5.10) can be computed. This control can effectively alter the oscillation frequency to a new target value.

However, for the control of TCL ensembles we require the modulation of the switching duty cycles while maintaining the frequencies constant. This led to the formulation of the optimal control problem in (5.3), where the integration interval $[0,T]$ of the objective function has been divided into two parts and new boundary conditions imposed. It then follows that the optimal control is piece-wise continuous and is given by

$$u(t) = \begin{cases} \frac{-\omega+\sqrt{\omega^2-c_1 Z^2(\phi)}}{Z(\phi)} & \text{for } 0 \leq \phi(t) < \phi_{\text{off}}, \\ \frac{-\omega+\sqrt{\omega^2-c_2 Z^2(\phi)}}{Z(\phi)} & \text{for } \phi_{\text{off}} \leq \phi(t) < 2\pi, \end{cases} \tag{5.12}$$

where the constants c_1 and c_2 are solutions to the integral equations

$$T_1 = \int_0^{\phi_{\text{off}}} \frac{1}{\sqrt{\omega^2 - c_1 Z^2(\phi)}} d\phi, \tag{5.13}$$

and

$$T - T_1 = \int_{\phi_{\text{off}}}^{2\pi} \frac{1}{\sqrt{\omega^2 - c_2 Z^2(\phi)}} d\phi, \tag{5.14}$$

where $T_1 = T_{\text{on}} - \delta T$, with $T_{\text{on}} = \phi_{\text{off}} T/2\pi$ is the time when the unperturbed TCL turns off naturally and δT is the desired change to T_{on}. For the parameter values in Table 4.1, the unperturbed duty cycle is $D = T_{\text{on}}/T = 0.428$, where $T = 0.790$ h (approximately 47 minutes) and $T_{\text{on}} = 0.338$ h. For example, if one wishes to reduce the duty cycle to $D_1 = 0.418$, T_{on} has to be reduced by $\delta T = (D_1 T) - T_{\text{on}} = -0.008$, hence $T_1 = 0.330$ h. Using the new desired T_1 value, we designed the corresponding control, with $c_1 = -54.177$ and $c_2 = 37.669$. The simulation results are shown in Figure 5.2.

Note that the designed control law is periodic, hence it can be repeated periodically to maintain the desired duty cycle. The design of a control law that increases the duty cycle is similar, therefore we do not show it here. In the next section, we are going to apply this control technique to TCL

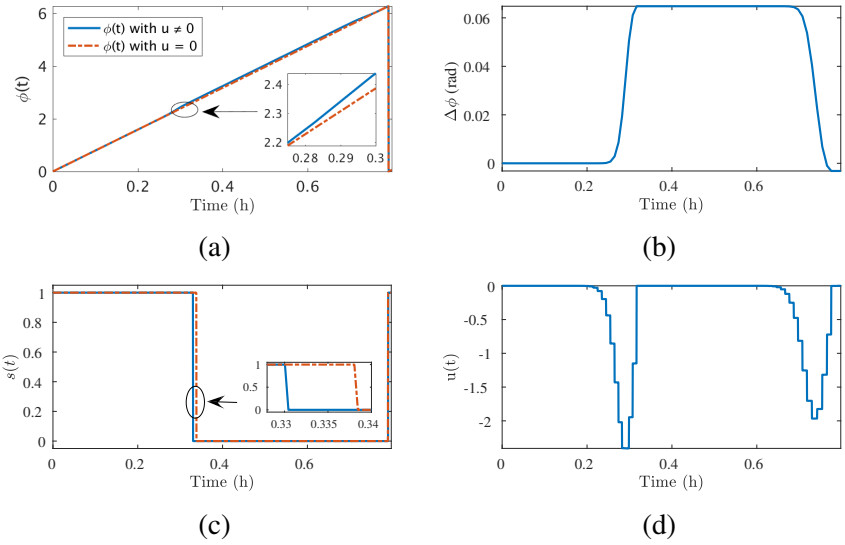

Figure 5.2: Application of the control law to the phase model. (a) Phase trajectories for both the controlled and uncontrolled systems. (b) Phase difference between the two trajectories in (a). (c) Switching functions, $s(t)$. The controlled system turns off at 0.330 h as desired. (d) Control input.

ensembles to control their aggregated power consumptions while maintaining load diversity, in other words avoid TCLs synchronization.

5.2 Optimal Control of TCL Ensembles

The illustration in Figure 5.2 shows the modulation of one TCL's duty cycle by a control designed using the PRC, $Z_s(\phi)$, of the switching function shown in Figure 5.1(a). However, our goal is to control a large collection of heterogeneous TCLs, therefore, we adopt a hierarchical control architecture in which the balancing authority (BA) sends a common control signal $\xi(t)$ to all the units in the population. The BA signal requests of each TCL to alter their energy consumptions by a few percents. This is then interpreted by the local control as a request to modulate the duty cycle.

In this chapter, we adopt a model reference control architecture for the local controller as shown in Figure 5.3. With this configuration, we also opt for the PRC, $Z_{\vartheta}(\phi)$, of the temperature variable, $\vartheta(t)$, to design the control signal, $u(t)$, given by (5.12). However, this control input is in the form of thermal energy and therefore cannot be applied directly to the actual system. Thus, we first apply this control to a reference model as an input $u(t)$ in the dynamic of the temperature, as follows

$$\begin{aligned} \dot{x}(t) &= \mu\left((\frac{\delta_b}{2}+\varepsilon)x - \frac{x^3}{3} + \vartheta - \vartheta_s\right), \\ \dot{\vartheta}(t) &= -\frac{1}{RC}\left(\vartheta - \vartheta_a + \bar{s}(t)PR\right) + u(t). \end{aligned} \tag{5.15}$$

In the rest of this chapter, given that (5.15) is the continuous equivalent of the hybrid-state TCL model, the later will be used as reference model and the actual control input to the plant will be a temperature signal $u_s(t) = \vartheta_r(t) - \vartheta(t)$, where $\vartheta_r(t)$ and $\vartheta(t)$ are the temperatures from the reference model and the plant, respectively.

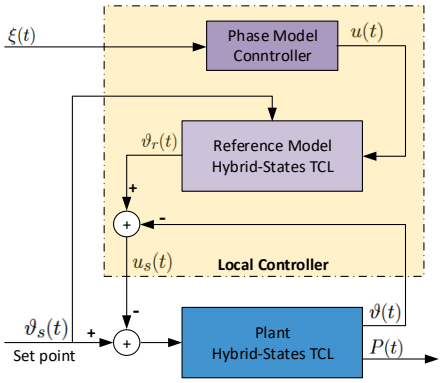

Figure 5.3: Local control architecture. The control signal $\xi(t)$ emitted by the balancing authority is received by each TCLs, which requests from each TCL to reduce or increase its power consumption by a few percents.The phase model controller receives $\xi(t)$ and generates a control signal $u(t)$ which is fed to the reference model as $v(t)$ in (5.15). The actual signal that controls the TCL is $u_s(t)^{\circ}$C.

5.2.1 Control of Heterogeneous TCL Populations

Control induced temporary synchronization of TCLs represents one of the main challenges for designing open-loop control policies for modulating the power consumption of a large population [147, 87]. Indeed, even small sudden changes of the set temperature (0.1-0.5°C) can induce large power fluctuations [166, 87], due to a large number of TCLs synchronizing. In Chapter 4, we examined this phenomenon using the concept Arnold tongues which, at the same time, allows us to evaluate DR capacity and bandwidth of a given TCL population. The Arnold tongues in Figure 4.11 and Figure 4.12, for example, were determined using a periodic forcing input $v(\Omega t)$, and the main observation is that, for a sufficiently strong forcing input, when its frequency Ω is close or equal to the TCL population mean frequency ω_0, synchronization occurs. Therefore, with a periodic sinusoidal control input, the capacity of ancillary services that a given population of TCLs can provide to support grid stability is limited to the regions outside the Arnold tongues in the power *vs.* frequency space [35].

The control law proposed in this chapter is designed to modulate the power consumption of a TCL without changing its natural oscillation frequency, ω. As one can see from the temperature trajectories in Figure 5.4(a), the frequency of oscillation is the same, before, during and after control. However, in Figure 5.4(b) one can see that the duty cycle is only changed when the control is applied, and immediately goes back to its natural value once the control is turned off. Such a control policy can help system operators modulate power consumption of TCLs while maintaining load diversity which in turn will reduce unwanted power oscillations.

The property of the control law in (5.12) to maintain constant the oscillation frequencies of the controlled TCLs, while modulating their duty cycles, enables fast control of the aggregate power, e.g., step changes of the aggregate power as shown in Figure 5.5(a). In order to achieve a steady

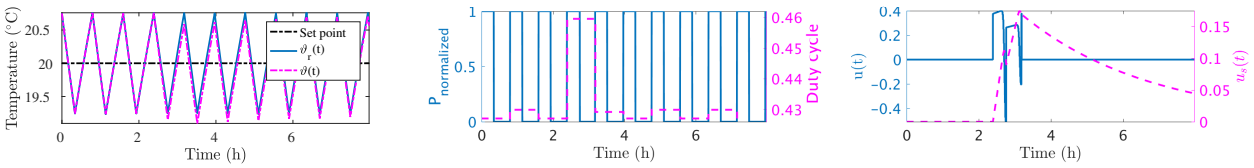

(a) (b) (c)

Figure 5.4: Modulation of the power duty cycle by a control applied for one period. (a) Temperature variables of the reference system, $\vartheta_r(t)$ and the plant $\vartheta(t)$. (b) Normalized TCL power and the duty cycle. (c) Controls applied to the reference system ($u(t)$) and to the plant ($u_s(t)$), respectively.

state power of ± 10 MW, step changes of $\mp 1.7^{\circ}$C are applied (see Figure 5.5(b)), however, without using a dedicated controller these changes induced strong power oscillations that could last a couple of hours as shown in Figure 5.5(a). On the other hand, when we use the control in (5.12), unwanted power overshoots are significantly reduced.

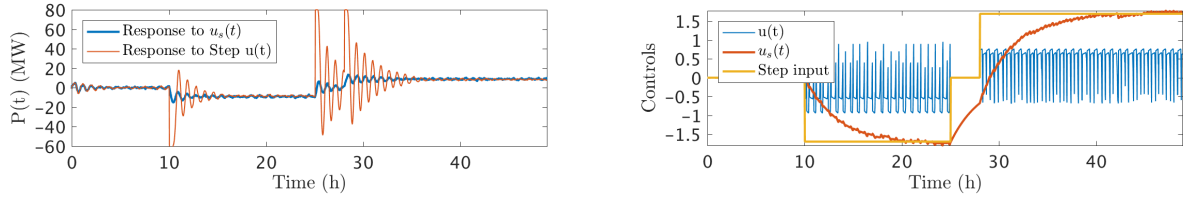

(a) (b)

Figure 5.5: Aggregate power responses to step-like power commands. (a) From 0 to 10 h, the power command is $u(t) = 0$. A command to reduce the power by 10 MW is received by the TCLs between 10 h and 25 h before being set back to zero for 3 h. A command to increase the power by 10 MW is then applied at time 28 h. (b) Optimal control inputs and the step-like input.

Ideally, when controlling TCLs it is desirable to maintain the temperatures as close as possible to their initial set-points such that consumers' comfort level is maintained within acceptable limits. Hence, to evaluate the performance of our control policy, in Figure 5.6 we plot the hourly average temperature of each TCL in the population. The first panel in Figure 5.6 shows that the control law in (5.12) slowly affects the mean temperature of the TCLs, which will be a more comfortable situation for the consumers (building occupants), while in the second panel of Figure 5.6, one can see that the step control abruptly changes the temperature which will be felt immediately by the

occupants. The overall behavior exhibited by the control law (5.12), that is, instantaneously changing the TCLs power consumption while minimizing the power overshoots and slowly affecting the TCLs temperatures in the population is a desirable property that TCL controllers ought to possess.

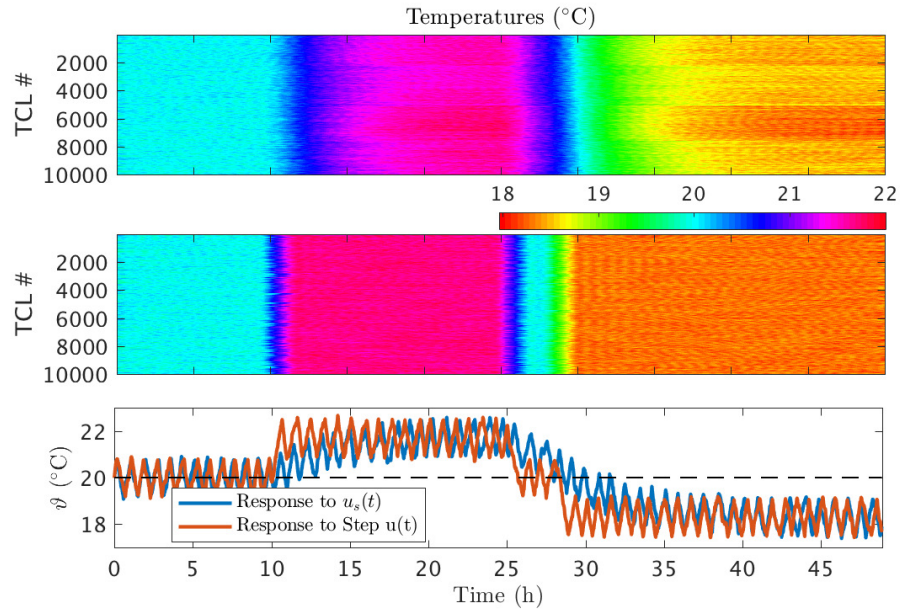

Figure 5.6: The temperature evolution of the TCLs during the controlled period. (First panel) and (second panel): one-hour moving average of the temperature of each TCL with application of the control $u(t)$ in (5.12) and the step-like control, respectively. (Third panel) Sample temperature of one TCL in the population. The parameters of the TCLs are uniformly distributed about the nominal values in Table 4.1 by $\pm 5\%$.

5.2.2 Tracking of an Area Control Error (ACE) Signal

In general, to compensate for the intermittent generation of renewable energy sources, power grid operators emit an ACE signal to all available ancillary services (AS) providers. The provided AS helps balance supply and demand to support grid stability and maintain good quality of service. In this section, we demonstrate provision of ancillary services by a heterogeneous population of

10,000 TCLs. We used the control law in (5.12) to track a real ACE signal taken from the Bonneville Power Administration (BPA) website [155]. This signal was filtered in the frequency band [0,4] rad/h (see Figure 5.7 (first panel)) and scaled down to a level that can be tracked with 10,000 TCLs. Figure 5.7 (third panel) shows that the aggregate power of the population closely follows the reference ACE signal, with a root mean square error of 2.7%. The average temperature of each TCL during the controlled period remains within $\pm 1^{\circ}$C of the set temperature (see second panel in Figure 5.7), which will have minimal adverse impact on the comfort level of consumers.

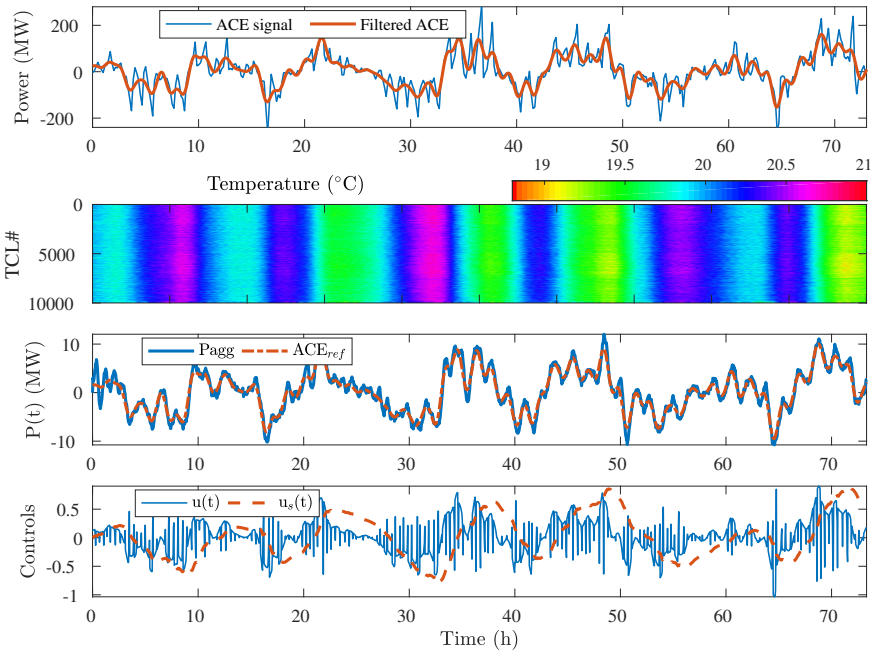

Figure 5.7: Tracking of the Area Control Error (ACE) signal low-pass filtered in the band $[0,4]$ rad/h. (First panel) Original ACE power signal for a three days period. (Second panel) One hour moving average of the TCLs temperatures. (Third panel) Scaled down ACE signal that can be tracked by a population of 10,000 TCLs. (Fourth panel) Sample control signals to the reference system ($u(t)$) and to the plant ($u_s(t)$), respectively.

Chapter 6

A Control Theoretic Approach to Optimal Placement of Driver Nodes in Complex Oscillator Networks

In Chapter 3, we presented a unified control framework for the design of a broadcast or global control that can manipulate the phases or frequencies of either an interacting or a non-interacting collection of oscillators. However, in some real-world applications it is neither feasible nor practical to control all the oscillators simultaneously with a common control signal. In this chapter, we focus on the pinning control problem, which is a feedback strategy that consists on controlling a small subset of nodes in a given network [95, 167, 168, 96]. Specifically, we look at pinning a network of oscillators to its equilibrium and derive analytic conditions under which this can be achieved with a single controlled node. A fundamental challenge of pinning control is to identify the most influential site for establishing stable behavior in the network and to unlock what this site is dependent upon. We address these problems by studying bidirectional networks consisting of n dynamical units and, without loss of generality, illustrate our findings through a network of

Stuart-Landau (SL) oscillators, that is a system of identical dynamic units coupled via a Laplacian matrix and in which each unit has an unstable fixed point.

6.1 Dynamics of Stuart-Landau Oscillator Networks

The Stuart-Landau (SL) oscillator, which is the normal form of the supercritical Hopf bifurcation [128, 169] has been widely used as a model for studying nonlinear phenomena in fluids, lasers, and Josephson junctions [170], and as an associative memory in neural networks [171]. It describes nonlinear dynamics evolving close to a bifurcation point, and the simplicity of this model makes it particularly appealing for theoretical analysis. The dynamics of a single SL oscillator is described by the coupled ordinary differential equations of two state variables, x and y, given by

$$\begin{aligned} \dot{x} &= \alpha x - \omega y - (x^2 + y^2)x, \\ \dot{y} &= \omega x + \alpha y - (x^2 + y^2)y, \end{aligned} \tag{6.1}$$

where α and ω are real parameters. Then, a network of n coupled SL oscillators with coupling in both x and y state variables stimulated by external inputs can be modeled by

$$\begin{aligned} \dot{x}_k &= \alpha x_k - \omega y_k - (x_k^2 + y_k^2)x_k + \sigma \sum_{l=1}^{n} a_{k,l}(x_l - x_k) + u_k(t), \\ \dot{y}_k &= \omega x_k + \alpha y_k - (x_k^2 + y_k^2)y_k + \sigma \sum_{l=1}^{n} a_{k,l}(y_l - y_k) + v_k(t), \end{aligned} \tag{6.2}$$

where σ is the coupling strength, $a_{k,l}$ is the coupling function connecting the oscillators k and l, and $u_k(t)$ and $v_k(t)$ are the external inputs applied to the oscillator k. In particular, we consider the feedback control of the form $u_k(t) = s(t) - Kx_k(t)$ and $v_k = s(t) - Ky_k(t)$, where $s(t) \equiv 0$ represents the desired dynamic behavior dictated by the pinner system. The coupling topology of the network

is described by the adjacency matrix A_{adj} with entries $a_{k,l}$ for $k,l = 1,\cdots,n$. If the elements k and l are coupled, then $a_{k,l} = 1$; otherwise $a_{k,l} = 0$. For the most part in chapter, we focus on undirected unweighted networks with symmetric couplings, i.e., $a_{k,l} = a_{l,k}$, and self couplings are not considered, i.e., $a_{k,k} = 0$ for $k = 1,\cdots,n$.

6.2 Network Stabilization by Pinning Control

6.2.1 Equilibria and Stability

In order to analyze the stability properties of the networked system in (6.2), it is essential to identify the equilibrium points. For the SL oscillator in (6.1), it is easy to verify, using the polar coordinate transformation, that $X_{\text{eq1}} = (0,0)'$ is the unique equilibrium point, where '$'$' denotes the transpose operation. The linearized dynamics around this equilibrium point is characterized by the Jacobian matrix, that is,

$$J_0 = \frac{\partial f(x,y)}{\partial X}\Big|_{X=X_{\text{eq1}}} = \begin{bmatrix} \alpha & -\omega \\ \omega & \alpha \end{bmatrix}, \tag{6.3}$$

where $X = (x,y)'$ and $f(x,y) = (\alpha x - \omega y - (x^2+y^2)x, \omega x + \alpha y - (x^2+y^2)y)'$. The eigenvalues of J_0 are $\lambda_1 = \alpha + i\omega$ and $\lambda_2 = \alpha - i\omega$, which imply that X_{eq1} is unstable since $\alpha > 0$.

6.2.2 Amplitude and Oscillation Death

When the SL oscillators are interconnected in a network as in (6.2), the origin X_{eq1} may no longer be the unique equilibrium state, depending on the coupling and control structure. In this case, the network can be stabilized at the nonzero equilibria. However, for amplitude death (AD) [172],

i.e., stabilization of the origin, to occur in such an oscillatory system, it is required that the origin X_{eq1} be a unique attractive equilibrium point, otherwise, only oscillation death (OD) [173], i.e., stabilization onto a nonzero equilibrium, can be achieved. In the following, we adopt the pinning control strategy as a means of inducing AD in a coupled oscillator network and, for that purpose we consider the coupling and feedback configuration in Section 6.1 which guarantees that the origin is the unique equilibrium point for SL oscillators. Later in Section 6.4, the boundary values of the coupling strength and the feedback gain beyond which stabilization at the origin can occur will be determined. We refer to these values as the critical coupling σ_c and critical gain K_c.

6.3 Identification of Network Structure Influence on the Stabilizability Property

Experimental work with networked oscillatory chemical processes has provided evidence that synchronization patterns are strongly affected by the architecture of the network [174]. In order to understand how the structure, i.e., the size and topology of a network, and further the location of the control site affect the stability properties of the networked system in (6.2), it is essential to have an analytic expression of the eigenvalues of the controlled network such that a sensitivity analysis can be conducted to determine the influence of such network parameters. In this section, we derive such analytical expressions for the chain and ring networks.

The Laplacian matrix associated with a chain network of n oscillators has a tridiagonal structure that allows for the analytical derivation and thus effective computation of its eigenvalues. Here, we consider pinning control of one oscillator in a chain by introducing the feedback gain K. For example, consider a chain of three ($n = 3$) SL oscillators with identical frequency and the pinner

is connected to the first oscillator. In this case, we have $u_1(t) = -Kx_1(t)$, $v_1(t) = -Ky_1(t)$, and $u_k(t) = v_k(t) = 0$ for $k = 2,3,\cdots,n$, and the Jacobian of this networked system evaluated at the origin is given by

$$A = \begin{bmatrix} \alpha-\sigma-K & -\omega & \sigma & 0 & 0 & 0 \\ \omega & \alpha-\sigma-K & 0 & \sigma & 0 & 0 \\ \sigma & 0 & \alpha-2\sigma & -\omega & \sigma & 0 \\ 0 & \sigma & \omega & \alpha-2\sigma & 0 & \sigma \\ 0 & 0 & \sigma & 0 & \alpha-\sigma & -\omega \\ 0 & 0 & 0 & \sigma & \omega & \alpha-\sigma \end{bmatrix}. \tag{6.4}$$

Eigenvalues of a Kronecker Sum of Matrices: The matrix A can be written as a Kronecker sum of two simple matrices as $A = I_n \otimes J_0 + G_1 \otimes I_2$, where J_0 is defined in (6.3), I_2 and I_n are 2×2 and $n \times n$ identity matrices, respectively; the matrix $G_1 = -\sigma L - K \times \text{diag}(\delta_1, \delta_1, \delta_2, \delta_2, \delta_3, \delta_3)$ with $\delta_1 = 1$ and $\delta_2 = \delta_3 = 0$, in which L is the Laplacian of the network. This decomposition as a Kronecker sum facilitates the computation of the eigenvalues of A through that of J_0 and G_1 using the following theorem.

Theorem 1 (Eigenvalues of a Kronecker sum of two matrices)**:** Let B be an $m \times m$ matrix with eigenvalues λ, and C be an $n \times n$ matrix with an eigenvalue μ. Then $\lambda + \mu$ is an eigenvalue of the Kronecker sum $(I_m \otimes B) + (C \otimes I_n)$ and any eigenvalue of $A = B \oplus C$ arises as such a sum of eigenvalues of B and C, and $I_m \otimes B$ commutes with $C \otimes I_n$ [175].

By Theorem 1, we may compute the eigenvalues of A in (6.4) by using the eigenvalues of J and G through

$$\lambda(A) = \lambda(J) + \lambda(G), \tag{6.5}$$

where $J = I_n \otimes J_0$, $G = G_1 \otimes I_2$, and

$$G_1 = \sigma \begin{bmatrix} -1 & 1 & 0 \\ 1 & -2 & 1 \\ 0 & 1 & -1 \end{bmatrix} - K \begin{bmatrix} 1 & 0 & 0 \\ 0 & 0 & 0 \\ 0 & 0 & 0 \end{bmatrix} = \begin{bmatrix} -(\sigma + K) & \sigma & 0 \\ \sigma & -2\sigma & \sigma \\ 0 & \sigma & -\sigma \end{bmatrix}. \tag{6.6}$$

The ability to compute the eigenvalues of the networked system using (6.5) allows us to shift our focus on the computation of the eigenvalues of A to that of G_1 (or equivalently of G), which depends on the network size, topology, and the placement of the feedback.

Adopting the notion proposed above for the computation of eigenvalues of a chain of SL oscillators, we consider the following matrix

$$G_n = \begin{bmatrix} b & c & 0 & \cdots & 0 & \cdots & 0 & 0 & 0 \\ a & 2b & c & \cdots & 0 & \cdots & 0 & 0 & 0 \\ \vdots & \vdots & \vdots & \ddots & \vdots & \cdots & \vdots & \vdots & \vdots \\ 0 & 0 & 0 & \cdots & 2b-\gamma & \cdots & 0 & 0 & 0 \\ \vdots & \vdots & \vdots & \cdots & \vdots & \ddots & \vdots & \vdots & \vdots \\ 0 & 0 & 0 & \cdots & 0 & \cdots & a & 2b & c \\ 0 & 0 & 0 & \cdots & 0 & \cdots & 0 & a & b \end{bmatrix}, \tag{6.7}$$

where the feedback γ is applied to the m^{th} oscillator in the network. Let λ be an eigenvalue of G_n and $v = (v_1, \ldots, v_n)'$ be the corresponding eigenvector. Then, we have $G_n v = \lambda v$, and this gives,

together with the dummy variables $v_0 = 0$ and $v_{n+1} = 0$, a system of equations,

$$\begin{aligned} av_0 + 2bv_1 + cv_2 &= \lambda v_1 + bv_1, \\ av_1 + 2bv_2 + cv_3 &= \lambda v_2 + 0, \\ &\vdots \\ av_{m-1} + 2bv_m + cv_{m+1} &= \lambda v_m + \gamma v_m, \\ &\vdots \\ av_{n-1} + 2bv_n + cv_{n+1} &= \lambda v_n + bv_n, \end{aligned} \tag{6.8}$$

that can then be put into a recursive form,

$$av_{k-1} + \beta v_k + cv_{k+1} = \lambda v_k + f_k, \quad k = 1, 2, \cdots, \tag{6.9}$$

with $f_1 = bv_1$, $f_m = \gamma v_m$, $f_n = bv_n$, and $f_k = 0$ for all $k \neq 1, m, n$, where $\beta = 2b$. Consider the infinite sequence $\bar{v} = \{v_k\}_{k=0}^{\infty}$ with $v_1 \neq 0$, since from (6.9) if $v_1 = 0$ then $cv_2 = 0$ and inductively $v_3 = v_4 = \cdots = v_n = 0$ which contradicts the definition of eigenvector that is a non-zero vector, and $f = \{f_k\}_{k=0}^{\infty}$ with f_j as defined above, it follows from (6.9) that

$$a\{v_k\}_{k=0}^{\infty} + \beta\{v_{k+1}\}_{k=0}^{\infty} + c\{v_{k+2}\}_{k=0}^{\infty} = \lambda\{v_{k+1}\}_{k=0}^{\infty} + \{f_{k+1}\}_{k=0}^{\infty}. \tag{6.10}$$

After some calculations omitted here, we arrive at the following equations characterizing the eigenvalues and the eigenvectors,

$$\begin{aligned} \lambda &= \beta + 2\sqrt{ac}\cos(\theta), \quad \theta \neq k\pi, \quad k \in \mathbb{Z}, \\ v &= \frac{2i}{\sqrt{\omega}}\{\rho^{j+1}\sin[(j+1)\theta]\}(f + c\bar{v}_1)\hbar, \end{aligned} \tag{6.11}$$

where $i=\sqrt{-1}$, $\bar{h}=\{0,1,0,\cdots\}$, and $\bar{v}_1=\{v_1,0,0,\cdots\}$. The interested reader can refer to [176] for more technical details; this reference derived the eigenvalues of tridiagonal matrices without the feedback perturbation γ. We can then evaluate for each $j\geq 1$ to obtain

$$\begin{aligned} v_j =& \frac{2i}{\sqrt{\omega}}\{cv_1\rho^j\sin(j\theta)+bv_1\rho^{j-1}\sin[(j-1)\theta]+H(j-m-1)\gamma v_m\rho^{j-m}\sin[(j-m)\theta] \\ &+H(j-n-1)bv_n\rho^{j-n}\sin[(j-n)\theta]\}, \end{aligned} \tag{6.12}$$

where H is a unit step function with $H(x)=1$ if $x\geq 0$ and $H(x)=0$ if $x<0$. Furthermore, we have

$$\begin{aligned} \frac{\sqrt{\omega}}{2i}v_{n+1} =& cv_1\rho^{n+1}\sin[(n+1)\theta]+bv_1\rho^n\sin(n\theta)+\gamma v_m\rho^{n-m+1}\sin[(n-m+1)\theta] \\ &+bv_n\rho\sin(\theta), \end{aligned} \tag{6.13}$$

$$v_n = \frac{2i}{\sqrt{\omega}}\{cv_1\rho^n\sin(n\theta)+bv_1\rho^{n-1}\sin[(n-1)\theta]+\gamma v_m\rho^{n-m}\sin[(n-m)\theta]\}, \tag{6.14}$$

with

$$v_m = \frac{2i}{\sqrt{\omega}}\{cv_1\rho^m\sin(m\theta)+bv_1\rho^{m-1}\sin[(m-1)\theta]\}. \tag{6.15}$$

Let $\rho=\sqrt{a/c}$ (with $a=c$ for undirected unweighted networks) and $\sqrt{\omega}=2i\sqrt{ac}\sin(\theta)$, substituting (6.14) and (6.15) into (6.13) yields, after some algebraic manipulations,

$$\begin{aligned} 0 =& a\sin[(n+1)\theta]+2b\sin(n\theta)+\frac{b^2}{a}\sin[(n-1)\theta] \\ &+\frac{\gamma}{a}\frac{a\sin(m\theta)+b\sin(m-1)\theta}{\sin(\theta)}\{\sin[(n-m+1)\theta]+\frac{b}{a}\sin(n-m)\theta\}, \end{aligned} \tag{6.16}$$

where we used the fact that $v_{n+1}=0$. Taking $a=\sigma$, $b=-\sigma$, and $\gamma=K$ in (6.16), where σ and K represent the coupling strength among oscillators and the feedback gain applied to the m^{th}

oscillator, respectively, we arrive, after further simplification, at

$$\begin{aligned}\sigma\{\sin[(n+1)\theta]-2\sin(n\theta)+\sin[(n-1)\theta]\}\\ +K\{\sin(m\theta)-\sin[(m-1)\theta]\}\{\sin[(n-m+1)\theta]-\sin(n-m)\theta\}=0.\end{aligned} \tag{6.17}$$

Using the substitution $a=\sigma$, $b=-\sigma$, and $\gamma=K$, the eigenvalue expression in (6.11) can then be written as

$$\lambda_k(G_n)=-2\sigma\left(1-\cos(\theta_k)\right), \tag{6.18}$$

where the θ_k's, $k=1,\cdots,n$, are the solutions to (6.17). The eigenvalues of $G=G_n\otimes I_2$ and $J=I_n\otimes J_0$ satisfy $\lambda(G)=\{\lambda_k(G_n)\}$ for $k=1,\cdots,n$, and $\lambda(J)=\{\alpha\pm i\omega\}$ repeating n times. The eigenvalues of A can then be calculated using (6.5), which gives

$$\lambda_k(A)=\alpha-2\sigma(1-\cos(\theta_k))\pm i\omega,\quad k=1,\cdots,2n. \tag{6.19}$$

Similarly, for a ring network the eigenvalues of the Jacobian matrix evaluated at an equilibrium point can be calculated using (6.18). But in this case, one needs to solve for θ_k satisfying the following equation

$$\begin{aligned}\{\sin[(n+1)\theta]+\frac{K}{\sigma}\sin[n\theta]-\sin[\theta]\}\times\\ \{\sin[\theta]+\sin[(n-1)\theta]\}-\sin^2[n\theta]-\frac{K}{\sigma}\sin[n\theta]\sin[(n-1)\theta]=0,\end{aligned} \tag{6.20}$$

which was derived using the same procedure as for the chain network.

The two network topologies (chain and ring) considered in this section have the same eigenvalue expression (6.18) with the corresponding angles (θ_k) defined by two different equations, (6.17) and (6.20), respectively. This is a clear indication that the eigenvalues are affected by the structure or topology of the network. Furthermore, we observe that the position m of the feedback appears in

(6.17) but not in (6.20), which stipulates that the pinning site has an effect on the eigenvalues of the chain network but not the ring network. However, we can see that the size of the network has an influence on the eigenvalues of both network topologies. The derivations in this section tells us that there networks in which the location of the control site has an impact on the eigenvalues of the network, and in others, this impact is minimal or nonexistent. Hence, in networks where the location of the control site matters, it is important to carefully select its location such as to maximize the influence on the control on the entire network.

6.4 Critical Coupling and Critical Gain of Pinned Networks

6.4.1 Critical Coupling

In the context of this chapter, the critical coupling σ_c refers to the boundary value of the coupling strength such that for any $\sigma > \sigma_c$, there exists a feedback gain K that can stabilize the network. The analytical expression of the eigenvalues of chain networks derived in Section 6.3 played a crucial role in understanding how the critical coupling is related to the dominant (the smallest) eigenvalue of the matrix $\bar{G}_n = -G_n$, with $\lambda_k(G_n)$ as defined in (6.18). From (6.19), we have that the real part of the dominant eigenvalue of A is given by

$$Re(\lambda_1) = \alpha - 2\sigma(1 - \cos(\theta_1)), \tag{6.21}$$

and it requires $\alpha < 2\sigma(1 - \cos(\theta_1))$ for the chain network to be stable. The critical coupling is then defined as the value of σ for which $Re(\lambda_1) = 0$ as $K \to \infty$, and for a chain or a ring network,

is given by

$$\sigma_c = \frac{\alpha}{2(1-\cos(\theta_1))}. \tag{6.22}$$

However, in general for any network topology we have

$$\sigma_c = \frac{\alpha}{\mu_1}, \tag{6.23}$$

where μ_1 is the smallest eigenvalue of $\bar{G}_n = L + K \times \text{diag}(\delta_1, \cdots, \delta_N)$ with $\delta_i = 1$ for the pinned node and $\delta = 0$, otherwise, and the gain is considered very large. As we can see from (6.23), the critical coupling is inversely proportional to the smallest eigenvalue of $\bar{G}_n$, which depends on the network topology, size and the location of the feedback.

6.4.2 Critical Feedback Gain

Dual to the notion of critical coupling σ_c, the critical gain K_c refers to the boundary value of the feedback gain such that for any $K > K_c$, there exists a coupling strength σ that can stabilize the network. To determine the critical feedback gain, we assume that the coupling strength is sufficiently large such that all the oscillators are in perfect synchrony. Indeed, one can show that the time evolution of the norm of the difference between the states of any two coupled oscillators is approximated by $\|x_j - x_i\|(t) \approx e^{-\sigma t}\|x_j - x_i\|(t_0)$. With an exponential decay, the difference will approach zero as time t approaches infinity. For very large coupling, this difference will approach zero very fast, and hence the oscillators will be synchronized.

Proposition 2: The critical feedback gain K_c of a network with only one pinned node is proportional to the size of the network n, i.e., the number of nodes, given by

$$K_c = n\alpha, \tag{6.24}$$

where α denotes the real part of the eigenvalue of the Stuart-Landau oscillator as modeled in Section 6.2.

Proof: Suppose that the coupling strength is sufficiently strong so that all of the oscillators in the network are synchronized. Pinning the first oscillator results in the system of differential equations for the states x_i and y_i,

$$\begin{aligned}
\dot{x}_1 &= \alpha x_1 - \omega y_1 - (x_1^2 + y_1^2)x_1 - Kx_1, \\
\dot{x}_2 &= \alpha x_2 - \omega y_2 - (x_2^2 + y_2^2)x_2, \\
&\vdots \\
\dot{x}_n &= \alpha x_n - \omega y_n - (x_n^2 + y_n^2)x_n,
\end{aligned} \tag{6.25}$$

$$\begin{aligned}
\dot{y}_1 &= \omega x_1 + \alpha y_1 - (x_1^2 + y_1^2)y_1 - Ky_1, \\
\dot{y}_2 &= \omega x_2 + \alpha y_2 - (x_2^2 + y_2^2)y_2, \\
&\vdots \\
\dot{y}_n &= \omega x_n + \alpha y_n - (x_n^2 + y_n^2)y_n,
\end{aligned} \tag{6.26}$$

where the coupling term $\sigma(x_i - x_j)$ for $i, j = 1, \cdots, n$ can be neglected for large σ, according to the analysis provided above. Summing over the x_i and y_i equations yields

$$\begin{aligned}
\sum \dot{x}_i &= n\alpha x_1 - n\omega y_1 - n(x_1^2 + y_1^2)x_1 - Kx_1, \\
\sum \dot{y}_i &= n\omega x_1 + n\alpha y_1 - n(x_1^2 + y_1^2)y_1 - Ky_1.
\end{aligned} \tag{6.27}$$

Linearizing (6.27) around the origin and computing the eigenvalues of the Jacobian, we find that a gain $K > n\alpha$ is necessary for the stabilization of the origin. Here we used the fact that in synchrony $x_1 = x_2 = \cdots = x_n$ and $y_1 = y_2 = \cdots = y_n$. □

In a similar fashion, one can show that for q pinned nodes, the critical gain is given by

$$K_c = \frac{n}{q}\alpha. \tag{6.28}$$

Hence, applying feedback to multiple nodes reduces the magnitude of the required gain for stabilization regardless of their locations in the network.

6.4.3 Critical Coupling of k-regular Graph Networks

Regular graphs have nodes with the same degree k [177], e.g., ring $(k = 2)$ and complete graph $(k = n-1)$ networks. In this type of networks, the critical coupling is independent of the location of the pinning site. Furthermore, it can be shown that the critical coupling $(\sigma_c)_k$ of a k-regular network of size $n \geqslant 3$, is always greater or equal to the critical coupling $(\sigma_c)_c$ of a complete graph, but less or equal to the critical coupling $(\sigma_c)_r$ of a ring network.

Let's first consider a ring network of size n, where we have $\mu_1 = 2(1-\cos(\pi/n))$. Note that for $n = 3$, the ring is also a complete graph and $\mu_1 = 1$ is the maximum value that the smallest eigenvalue of G can take for a single pinning site configuration ($0 < \mu_1 < 1$ for $n \geqslant 3$ in k-regular graph networks). One can further verify that for any complete graph network of size $n > 3$, $\mu_1 = 1$ independently of n (it is assumed that the feedback gain $K \to \infty$).

As an example, consider a complete graph of 7 nodes (6-regular graph). The matrix G_7 of such a network is given by

$$G_7 = \begin{bmatrix} 6+K & -1 & -1 & -1 & -1 & -1 & -1 \\ -1 & 6 & -1 & -1 & -1 & -1 & -1 \\ -1 & -1 & 6 & -1 & -1 & -1 & -1 \\ -1 & -1 & -1 & 6 & -1 & -1 & -1 \\ -1 & -1 & -1 & -1 & 6 & -1 & -1 \\ -1 & -1 & -1 & -1 & -1 & 6 & -1 \\ -1 & -1 & -1 & -1 & -1 & -1 & 6 \end{bmatrix}. \tag{6.29}$$

The eigenvalues of G_7 are $1,7$ and K, with multiplicity $1,5$ and 1, respectively. In fact, for any complete graph network of size n, regardless of the pinning site the eigenvalues of G_n are 1 and K with multiplicity 1 each, and n with multiplicity $n-2$. Hence, by (6.23) the critical coupling of a complete graph is less or equal to that of a ring network, since $(\sigma_c)_c = \alpha/\mu_1 = \alpha \leq (\sigma_c)_r = \alpha/(2-2\cos(\pi/n))$. Moreover, the critical coupling $(\sigma_c)_k$ of any k-regular graph network satisfies $(\sigma_c)_c \leqslant (\sigma_c)_k \leqslant (\sigma_c)_r$ for all $n \geqslant 3$.

6.4.4 Stability Hyperbola

The critical coupling and feedback gain define the extreme operating points, $(K \to \infty, \sigma_c)$ and $(K_c, \sigma \to \infty)$, while normal operating points require finite values of the coupling strength and feedback gain. It would then be convenient to characterize the stability boundary knowing K_c and σ_c such that the choice of a stabilizing finite pair (K, σ) for the networked system is facilitated.

We refer to the curve separating the regions $Re(\lambda) < 0$ and $Re(\lambda) > 0$ in Figure 6.1(a) as the *stability hyperbola* since it can be described by the equation of a rectangular hyperbola [178], given by

$$y = \frac{a}{x - K_c} + \sigma_c, \tag{6.30}$$

where $y = \sigma$ (coupling) and $x = K$ (feedback gain). The asymptotes of the hyperbola are given by K_c and σ_c, and thus it suffices to determine the hyperbola using (6.30) if an additional point, say (K', σ'), on the hyperbola is known. However, this point (K', σ') (see Figure 6.1(a)) is in general arduous to compute, hence alternatively we find the point (K^*, σ^*) on the line $K = \sigma$. Once this point is known, we can compute a in (6.30) as $a = (\sigma^* - \sigma_c)(K^* - K_c)$, and then rewrite (6.30) as

$$\sigma = \frac{(\sigma^* - \sigma_c)(K^* - K_c)}{K - K_c} + \sigma_c. \tag{6.31}$$

Equation (6.31) is a direct consequence of a mathematical linear stability analysis that was initially conducted on the chain network. Indeed, from (6.21), when $Re(\lambda_1) = 0$, we can derive the expression for σ as a function of the angle θ, i.e., $\sigma = \alpha/(2 - 2\cos\theta)$, which is a hyperbola for $\theta \in [0, \pi)$ with the asymptotes given by the critical gain $K = K_c$ and coupling $\sigma = \sigma_c$. From calculus we know that a hyperbola is the only conic with asymptotes, therefore, if our assumption that the stability curve is a hyperbola is correct, then the inscribed angle theorem for hyperbolas must be satisfied. Namely, taking any four points, $P_1, \ldots, P_4$, as shown in Figure 6.1(b), the angles $\angle P_1P_3P_2$ and $\angle P_1P_4P_2$ are equal [179], or, equivalently

$$\frac{(y_4 - y_1)(x_4 - x_2)}{(x_4 - x_1)(y_4 - y_2)} = \frac{(y_3 - y_1)(x_3 - x_2)}{(x_3 - x_1)(y_3 - y_2)}. \tag{6.32}$$

A straightforward calculation by choosing any four points satisfying $Re(\lambda_1) = 0$ shows that our assumption is correct and that indeed the stability curve is a hyperbola. Note that (6.31) is general and applies to any undirected network topology.

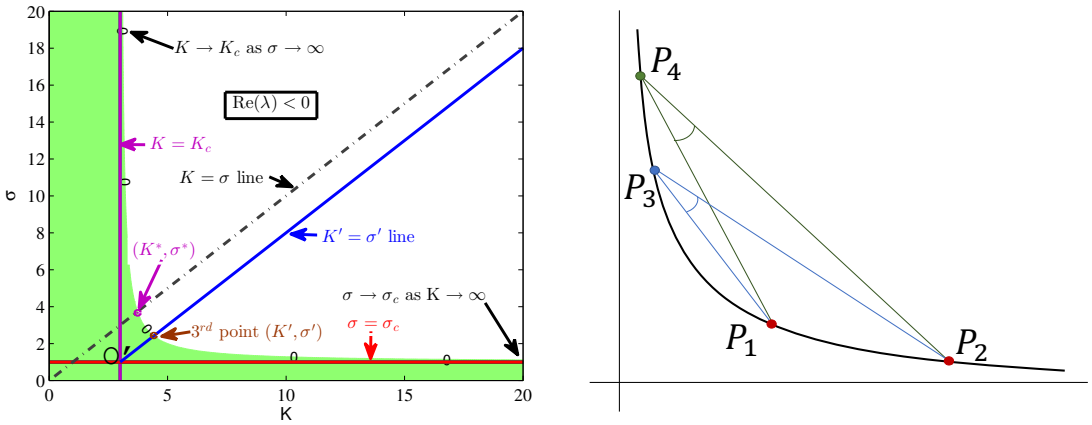

(a) (b)

Figure 6.1: Stability hyperbolas. (a) Analytic stability hyperbola of a chain network depicting the stability boundary. The asymptotes are defined by the critical coupling σ_c and gain K_c. The white and green areas represent the stable and unstable regions, respectively. (b) Hyperbola's inscribed angles.

In the previous sections, we have shown that the critical gain and coupling are dependent on the network structure, i.e., size and topology. Furthermore, we have shown that except for a few particular network topologies (k-regular graphs), the critical coupling is also dependent on the location of the control site. To illustrate how the stability hyperbola is affected by the network size, we consider the case of a chain network where pinning control is applied to the first oscillator. In this particular case, we can derive an analytic expression for determining the third point (K^*, σ^*) on the stability hyperbola. First, we set $Re(\lambda_1) = 0$ in (6.21) and then solve for $\sigma^* = \alpha/2(1-\cos\theta_1)$. Using the relation $\sigma^* = K^*$ in (6.17), we obtain $\theta_1 = \pi/(2n+1)$ (valid for pinning control applied

to the first oscillator only), which leads to

$$\sigma^* = \frac{\alpha}{2 - 2\cos(\frac{\pi}{2n+1})}. \tag{6.33}$$

As it can be seen from (6.33), the coupling strength σ^* increases as n increases, which implies that the third point (K^*, σ^*) moves upward, which means the stability hyperbolas are shifted both vertically and horizontally as shown in Figure 6.2(a). It is then clear that larger network are harder to stabilize than smaller ones, furthermore, they require large feedback gains and coupling strengths. Note that for this pinning configuration, we have an analytic expression describing the third, however, it is not always easy to find such analytic expression. In general, for other pinning control scenarios, one needs to start by numerically solving for the angle θ, and then compute the coupling σ^* and gain K^*.

When the network topology and size are fixed, the location of the control site has no influence on the critical gain, however, its impact on the critical coupling can be significant. In Figure 6.2(b), we show how the stability hyperbolas are affected by the location of the control site in a chain network of nine oscillators.

From this example, we see that controlling the network through node 1 requires a much higher coupling strength than controlling through node 5. For small networks and simple topologies such as the chain, a quick computation of the critical coupling σ_c using (6.23), for every node, could suffice to determine the optimal control site, which minimizes the control effort. However, for large complex networks this approach is not efficient. In the next section, we present a computational efficient and accurate method for determining the optimal control site.

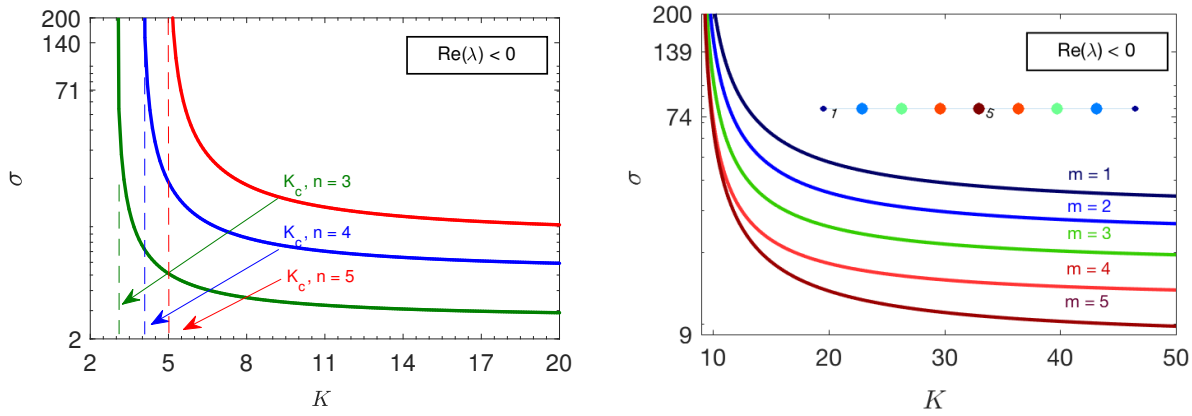

Figure 6.2: Stability hyperbolas for stabilization of network dynamics. (a) Illustration of the shifting of hyperbolas as a function of the network sizes, $n = 3,4,5$. (b) Hyperbolas corresponding to different pinned nodes in a chain network of nine oscillators. The hyperbolas move upward due to an increase of σ_c, for control sites other than the center (5th node), which minimizes σ_c. Stronger coupling is required for stabilization with a given feedback gain $K > K_c$, for any pinned node other than node 5.

6.5 Optimal Placement of Control Sites

Determining the best set of nodes to receive pinning controls in networked systems is a complex combinatorial problem. In this section, we propose an effective algebraic technique to identify one such node to receive pinning control without resorting to an exhaustive search algorithm or heuristic methods based on various centrality measures, such as degree, betweenness, closeness, and the eigenratio [180, 168].

Optimal Pinning Problem: The optimal pinning control problem is concerned with the selection of the best control site(s). That is, given a network of n oscillators, find the node j to pin such that the control effort is minimized, i.e., for a fixed coupling strength σ, the feedback gain K is minimized; or for a fixed feedback gain K, the coupling strength is minimized.

The problem at hand is the stabilization of the origin through pinning control, which can be treated as pole assignment in control theory [181]. And as we have shown in Section 6.4, the critical coupling is inversely proportional to the dominant eigenvalue of the matrix $\bar{G}_n$. Suppose that the eigenvalues of $\bar{G}_n$ are ordered as $\lambda_1 < \lambda_2 \leqslant \cdots \leqslant \lambda_n$ (for a connected graph), then in the absence of feedback, i.e., $K = 0$, the smallest eigenvalue $\lambda_1 = 0$ given by (6.18) (for a chain or a ring network) is independent of the coupling strength σ, while $\lambda_2, \cdots, \lambda_n$ are proportional to σ. Therefore, in order to stabilize a network of coupled (SL) oscillators, we need to move the dominant eigenvalue λ_1 away from zero to a value greater than the constant α in the SL oscillator model by applying the feedback gain K. As a result, the problem of finding the optimal control site is reduced to identifying the node j at which the feedback gain K will be the most effective (in the sense that for a given fixed coupling and gain (σ, K), the feedback at the optimal control site will have the most stabilizing impact on the networked system than at any other location) in placing λ_1 at a desired location in the complex plane. This problem can be tackled using the notion of geometric measure of modal controllability [182], which allows one to quantify the influence of each input on a particular eigenvalue. However, extra care must be taken when this method is applied to systems with repeated eigenvalues [183], and it requires the computation of eigenvalues at least n times, corresponding to each possible control site in the network, which is not very practical when dealing with large complex networks. A comprehensive description of this approach as it applies to networks of oscillators is given in Appendix D.1.

To circumvent the computational burden of the modal controllability method, we propose a methodology based on Lyapunov's direct method [181, 184], where a Lyapunov function $V(x)$ is established to determine stability of a dynamical system. We would refer to this approach as the *Lyapunov-based method* (LBM).

Theorem 3: Consider the time-invariant linear autonomous system

$$\dot{x} = Ax, \tag{6.34}$$

with the origin as an equilibrium point, where $x \in \mathbb{R}^n$ and $A \in \mathbb{R}^{n \times n}$. The system described by (6.34) has the origin as a globally asymptotically stable equilibrium point if a Lyapunov function $V(x)$ can be found such that (i) $V(x) > 0$ for all $x \neq 0$ and $V(0) = 0$, (ii) $\dot{V}(x) < 0$ for all $x \neq 0$, and (iii) $V(x) \to \infty$ as $\|x\| \to \infty$ [184].

A canonical Lyapunov function is $V(x) = x'Px$, with $P \succ 0$ a real symmetric, positive definite (PD) matrix. Taking the time derivative of the Lyapunov function and substituting for the dynamics in (6.34) lead to $\dot{V}(x) = x'[A'P + PA + \dot{P}]x$. If the system matrix A is Hurwitz, then $\dot{V}$ must be negative definite (ND), and for any positive definite (PD) matrix $Q \in \mathbb{R}^{n \times n}$, there exists a matrix $P(t)$ such that the matrix differential equation,

$$A'P + PA + \dot{P} = -Q \tag{6.35}$$

is satisfied. Furthermore, for a given constant matrix A, a constant matrix P will suffice for (6.35), which implies $\dot{P} = 0$ and then (6.35) becomes

$$A'P + PA = -Q. \tag{6.36}$$

The main idea of our method is to consider a control system described by the Laplacian dynamics associated with a network of n nodes, given by

$$\dot{x} = -\sigma Lx + Bu, \tag{6.37}$$

where $L \in \mathbb{R}^{n\times n}$ is the graph's Laplacian matrix of the given network, $B \in \mathbb{R}^{n\times m}$ is an input matrix, and $u = u(x) = -Kx \in \mathbb{R}^m$ is a feedback control law. It is well known that the linear quadratic regulator (LQR) control of the form $u = -Kx = -B'Px$, where P is the solution to the algebraic Riccati equation (ARE) as in (6.36) with $A = -\sigma L$, is a stabilizing feedback control, namely, the closed loop matrix $A_{cl} = A - BB'P$ is Hurwitz [181]. Observe that if we substitute A by A_{cl} in the Lyapunov equation (6.36) we would obtain an ARE and the computed P matrix will be PD. However, solving the ARE associated with a large network system would be computationally expensive. In the following, we would then derive simpler solutions.

To apply the Lyapunov formalism, we will shift the real part of the eigenvalues of A and consider the Lyapunov equation $[A - \frac{1}{n}I]'P + P[A - \frac{1}{n}I] = -Q$, which gives

$$P = -\frac{1}{2}[A - \frac{1}{n}I]^{-1}Q \succ 0, \tag{6.38}$$

where Q is taken as the identity matrix I. Note that the Laplacian dynamics in (6.37) is stable in the sense of Lyapunov [181], in other words, it is marginally stable. Hence, we can relax the condition for P and allow it to be positive semidefinite (PSD) without destabilizing the system. Note that by doing so, the Lyapunov function $V(x) = x'Px$ no longer satisfies condition (i) in Theorem 3 and $V(x) \geqslant 0, \forall x \neq 0$. Nonetheless, we obtain the same information about the relative importance of each control site as if (6.38) was used. By considering this relaxed condition and taking advantage of the symmetry of A, P, and Q, we obtain a simple solution to the Lyapunov equation (6.36),

$$P = -\frac{1}{2}A^{\dagger}Q, \tag{6.39}$$

where $Q = I$ and $A^{\dagger}$ is the Moore-Penrose pseudoinverse of the matrix A. It is important to note that any feedback gain $K > 0$ is sufficient to stabilize the dynamical system in (6.37), and that our

aim thus far is not to compute the stabilizing gain, but rather to find some measure that will allow for the determination of the best control site. We refer to this measure as the control centrality. Once the optimal control site is known, then the appropriate stabilizing gain K can be computed taking into consideration the dynamics of the oscillators in the network.

Let us now define the vector of control centrality measures, $v_c = (1/d_1, \cdots, 1/d_n)'$, as the reciprocal of the diagonal entries of the matrix P, where $d = \text{diag}(P) = (d_1, \ldots, d_n)'$, and the control centrality index i_c (with $i_c = 1, \cdots, n$) as the index of the i^{th} entry of v_c, respectively. To compute the control centralities, we consider that n feedback controls are applied, and thus the input matrix $B = I$ and the gain matrix $K = P$.

It is known that modes (eigenvalues of the A matrix) that are less controllable from a given input require higher gains to stabilize them [185]. Therefore, by computing the gain as proposed, the most influential node in the network will require the least amount of feedback gain. This is the intuition behind the proposed method. Therefore, pinned nodes that have less control (or influence) over the dominant eigenvalue of the network will have low control centrality values, while pinned nodes that have more control over the dominant eigenvalue of the network will have higher values of control centrality. Hence, the node with the highest control centrality is the optimal control site, and its index indicates the location in the network.

Remark 1: The concept of control centrality has been introduced before to quantify the ability of each node to control a directed network [186], however, in this thesis we use it as a measure to quantify the ability of each node to stabilize a network through pinning.

6.6 Evaluation and Analysis of the Lyapunov-Based Method

The evaluation of the LBM presented is Section 6.5 was primarily done using thousands of numerically generated networks. In order to cover diverse network structures one could encounter, we used four different graph topologies, namely, the Barabási-Albert (BA) scale free [187, 188], the Erdős-Rényi (ER) random network [189], the Watt-Strogatz (WS) small world [190] and tree networks [191]. The scale free networks were generated using the preferential attachment algorithm of Barabási and Albert [188]. The initial seed was a small connected graph with the average node degree $\gamma_0 = 2$. The ER random networks were generated by the random graph model $\mathcal{G}(n, p)$ with n nodes and probability of existence $p = \ln(n)/n$ for each possible edge. The WS small-world networks were generated per the Watts and Strogatz model [190] with a rewiring probability $\beta = 0.15$ and an expected degree $\langle\gamma\rangle = 20$ for networks of size $n \geq 25$. The tree networks were generated using a fixed maximum number of generations and node degree (fixed maximum number of children for each non-pendant vertex) and the tree-like networks were spanning trees of ER random networks with a desired number of nodes.

The performance of LBM (denoted M1) is shown in Table 6.1 for different network topologies, where the percentages indicate how many times each method selected the control site with the lowest critical coupling σ_c. From these results, we see that there are networks (for each topology) for which our method did not select the control node with the lowest σ_c. A closer look at these networks lead to the discovery of what we call *degenerate networks*.

The descriptions of different control centralities used in Table 6.1 are provided in Table 6.2, where the optimal control site is located using the index corresponding to the largest value of the control centrality. We use $\langle d_k\rangle$ to denote the average distance measured at node k, that has degree γ_k, and v_k is the k^{th} entry of the Fiedler vector $v_f = (v_1, \cdots, v_n)'$ i.e., the characteristic valuations [191].

Table 6.1: Accuracy of the methods for different topologies over 1000 runs

Methods/Topologies	M1	M2	M3	M4	M5
BA scale free	98.8%	91.8%	94.0%	2.20%	17.7%
ER random graph	99.8%	83.5%	90.8%	1.80%	3.30%
WS small world	99.9%	72.0%	82.1%	1.50%	2.20%
Tree	43.5%	22.6%	24.8%	96.3%	96.5%

Table 6.2: Methods descriptions

Methods	Control centrality measures
M1	Computed by Lyapunov-based method using equation (6.39)
M2	Obtained using the node's degree γ_k
M3	Computed using $1/\langle d_k \rangle$ for acyclic graphs and $\gamma_k/\langle d_k \rangle$ for cyclic graphs
M4	Obtained using the characteristic valuations $1/v_k$
M5	Computed using the equation $1/(v_k * \langle d_k \rangle)$

6.6.1 Degeneracy and Suboptimality of the Control Site

Definition 2 (Degenerate network)**:** A degenerate network is a network that has at least two stability hyperbolas corresponding to two distinct pinning sites that intersect in the (K, σ)-plane at a point (K_1, σ_1), with $K_1 < \infty$ and $\sigma_1 < \infty$.

Remark 2: The control site obtained by (6.39), which minimizes the feedback gain, yields a global optimal control site if the network is not degenerate, and a suboptimal control site if the network is degenerate (i.e., optimal in the strong coupling regime). This is evident when the network is not degenerate because in this case the stability hyperbolas do not intersect, and the stability regions become smaller as the pinning site moves away from the optimal site as in Figure 6.2(b). However, when a network is degenerate, the stability hyperbolas intersect as in Figure 6.3. One can then see that the pinning site that minimizes the stabilizing feedback gain in the strong coupling and weak feedback gain region (R1), no longer minimizes the gain in the weak coupling and strong feedback

gain region (R2). Recall that LBM is based on the principle that modes that are less controllable from a given input will require stronger feedback gains for stabilization, therefore, this method always selects the node that minimizes the gain as the optimal node. So, in case of degenerate networks, the optimality is limited to the weak feedback gain region (R1).

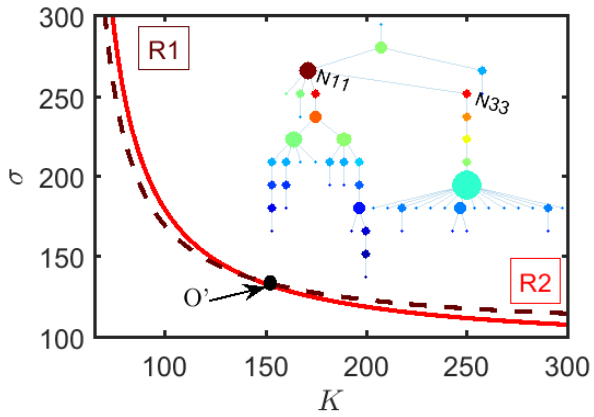

Figure 6.3: Intersecting stability boundaries of degenerate tree networks. Intersecting stability hyperbolas in a 55-node degenerate tree network. The hyperbola (red) corresponding to the node with the lowest σ_c intersects with the hyperbola in brown at the point O' with a finite coupling σ. The blue hyperbola is associated with the optimal pinning site obtained with the Lyapunov method which is optimal in region R1 (a high and low K region, on the left of a line passing through the origin and the point O') and suboptimal in region R2.

This counterintuitive phenomenon which induces a switch of the most influential node in a network, from one node to another, as the coupling strength gets stronger is prominent in tree networks (56.5% in our experiments) while relatively rare in scale free networks (1.2% occurrence). In Figure 6.4, we evaluate LBM against other heuristic approaches described in Table 6.2, in terms of the quotient of the critical couplings $\sigma_c/\sigma_{c-\min}$. When we separate nondegenerate from degenerate networks, we can see from Figure 6.4(a) that our method always select the node with the lowest σ_c, whereas in Figure 6.4(b) we observe significant differences, especially for tree networks.

Thus far, the Lyapunov-based method has been tested on synthetic networks (i.e., computer generated) but its main advantage is to efficiently find the optimal control site in large complex networks.

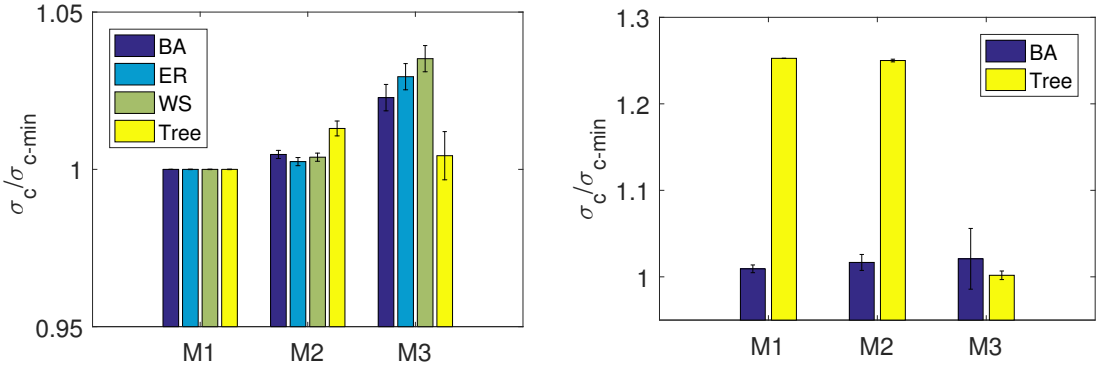

(a) (b)

Figure 6.4: Numerical results on degenerate and nondegenerate networks. (a-b) Quotients $\sigma_c/\sigma_{c-\min}$ for nondegenerate and degenerate networks, respectively (plot of average values and their confidence intervals).

To that end, we tested LBM on real-world networks, and furthermore, we observed degenerate central nodes, for example, in power and social networks.

Specifically, we considered the Western States power grid of the United States (which is a network of 4,941 nodes with 6,594 edges) [190] and the Ego-Facebook network (which is a network of 2,888 nodes with 2,981 edges) [192, 193] that are shown in Figure 6.5(a) and Figure 6.5(b), respectively. The color bar denotes the calculated control centrality for each node. For the power network, LBM identified the optimal site N427 in the weak coupling region and the steepness analysis revealed that this network has 3 degenerate control sites (N1244, N427 and N394) that created 2 hyperbola intersections (N1244 with N427 and N1244 with N394), shown in Figure 6.5(c). As a result, either node N427 or N1244 can be the optimal site in the high gain region, depending on the coupling strength. In addition, this example shows that when the degree centrality fails to select the optimal site, the resulting control node can be far from optimal. Indeed, in the power grid node N2554 has the highest node degree $\gamma_{\max} = 19$, with a critical coupling $\sigma_c = 5,390$, whereas

the two best control sites N427 and N1244 have lower nodes' degree $\gamma = 6$ with the corresponding $\sigma_c = 3,792$ and $\sigma_c = 4,001$, that are 29.65% and 25.77% lower than the critical coupling of N2554.

As for the social network, we found two degenerate control sites, N288 (node degree $\gamma = 481$) and N603 ($\gamma = 769$), with $\sigma_c = 459.07$ and $\sigma_c = 457.84$, respectively. The optimal pinning site switches from node N288 in the low feedback region to N603 in the high feedback region (see Figure 6.5(d)). The switching of the optimal sites due to the degeneracy in the network has practical implications, e.g., change of the social relationship. For example, the Facebook user N603 could be the pivot in this social network when the other users were not acquainted (with weak coupling strength σ) and lose his role to N288 when the friendship among other users was strengthened (in the strong coupling region).

To corroborate the theoretical findings, experiments were performed on networks of coupled chemical reactions. The nodes of the network are corroding nickel wires in sulfuric acid, and without an external control, the corrosion rate (current) is oscillatory. The perturbation of the circuit potential through feedback can stabilize the chemical reaction, hence suppressing oscillations. The coupling between nodes is established by cross-resistances whose currents affect the reaction rate [174] (See Appendix D.2).

The validation of the developed Lyapunov-based method for selecting the optimal control site is carried out using an 8-node nondegenerate network shown in Figure 6.6(a). Using LBM, we theoretically predicted that node 1 is the optimal control site. In experiment, we first determined a stabilizing feedback gain K in weak coupling regime by pinning node 1, and then measured the mean oscillation amplitudes A of the oscillations for different control sites with the same K, (see Figure 6.6(b)). The results show that as the control site moves away from node 1, the control becomes less effective resulting in higher mean amplitude of oscillations. In Figure 6.6(c), we

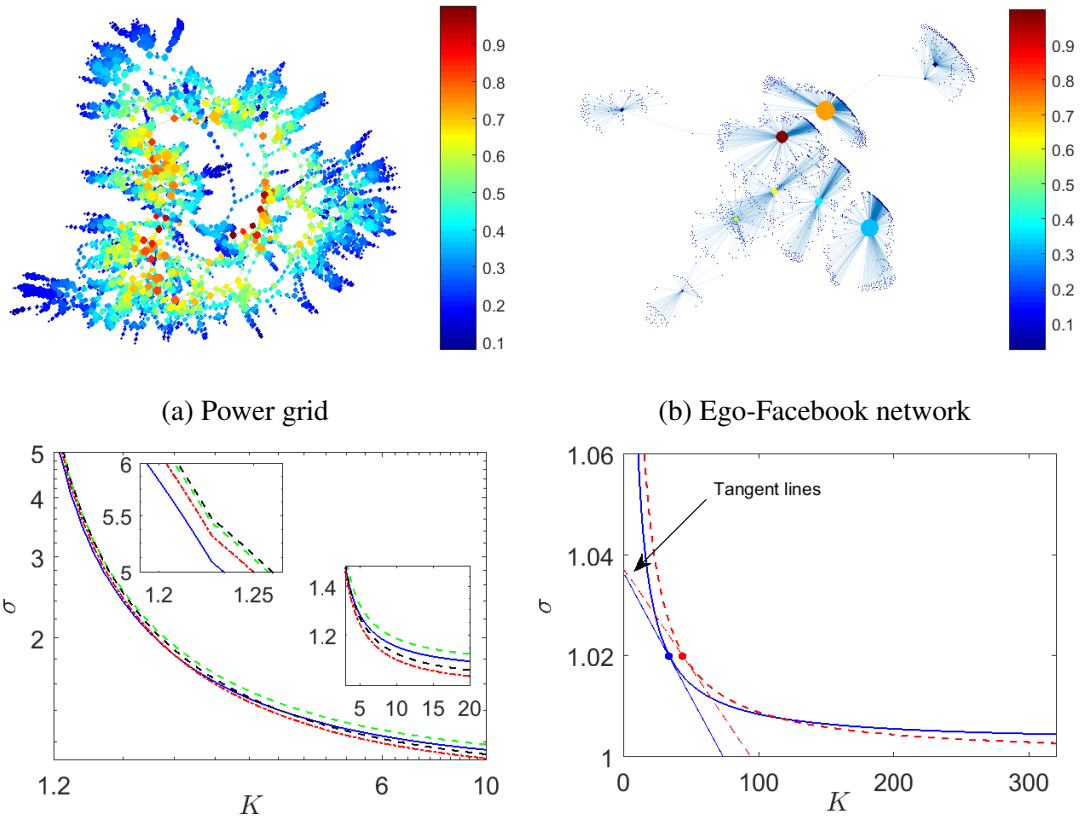

(a) Power grid

(b) Ego-Facebook network

(c) Stability hyperbolas for (a)

(d) Stability hyperbolas for (b)

Figure 6.5: Real-world degenerate networks. (a) Western States power grid of the United States. (b) Ego-Facebook networks, respectively. The colormap represents the normalized control centrality of each node from zero to one (red, highest centrality value). (c) and (d) Intersecting hyperbolas for the power grid and Ego-Facebook networks, respectively. The hyperbolas in (c) were normalized by $\sigma_{c-\min} = 3,792$ (N427, red hyperbola) and K_c = 4941. The other hyperbolas have $\sigma_c = 3,865$ (N394, black), $\sigma_c = 4,001$ (N1244, blue) and σ_c = 4,086 (N1309, green). The optimal site (N1244) selected with our method and node N427 have the same degree $\gamma = 6$, while the other two suboptimal nodes have $\gamma = 5$. The network maximum degree is $\gamma_{\max} = 19$ (N2554 with $\sigma_c = 5,390$). The hyperbolas in (f) were also normalized by the network $\sigma_{c-\min}$ and K_c. The tangent lines show the steepness of the hyperbolas.

show the trend of the critical couplings as the quotient σ_c/σ_c^1 (σ_c^1 is the critical coupling for node 1) which agrees with experimental variations of the amplitudes.

Likewise, degeneracy was theoretically predicted (using the procedure in Section 6.6.2) and experimentally observed in the 10-node network in Figure 6.6(d-e), which was obtained by adding a star motif to the end of a chain network. Using LBM node 3 was predicted as the optimal control site in the strong coupling (weak gain) regime, whereas node 1 was found to be optimal in the weak coupling (strong gain) regime. This is experimentally confirmed by measuring the mean oscillation amplitudes of the network for both control sites, in the weak and strong coupling regimes, respectively (see Figure 6.6(f)). The results thus show that the distance of a node to the peripheries of the network becomes more important as the coupling strength is weakened, while at strong coupling more weight is placed on the degree of nodes causing the shift in the optimal control site. These experimental observations support the stability hyperbola-based selection of the optimal control site.

6.6.2 Identification of Degenerate Undirected Networks

This test determines whether or not the hyperbola corresponding to the optimal site selected with our proposed method intersects with any other hyperbolas, in which case, the network is degenerate. Hence, the selected node is only a suboptimal solution in the (K, σ) space. One strong indication of degenerate networks is when the critical coupling σ_c^k associated with the optimal pinning node k selected by the Lyapunov method is greater than the critical coupling associated with some other node i, denoted σ_c^i, in the network. A natural approach to determine intersecting points among hyperbolas is to check the existence of the solution (K, σ) satisfying the equations defining the hyperbolas. However, this approach, though accurate, is computationally costly and time consuming for large networks. To give an idea, the computation of σ_c at each node in the power grid shown in Figure 6.5 took approximately 8 hours on a standard desktop computer, and, furthermore, the computation for finding the point (K^*, σ^*), where $K^* = \sigma^*$ on the hyperbola (see

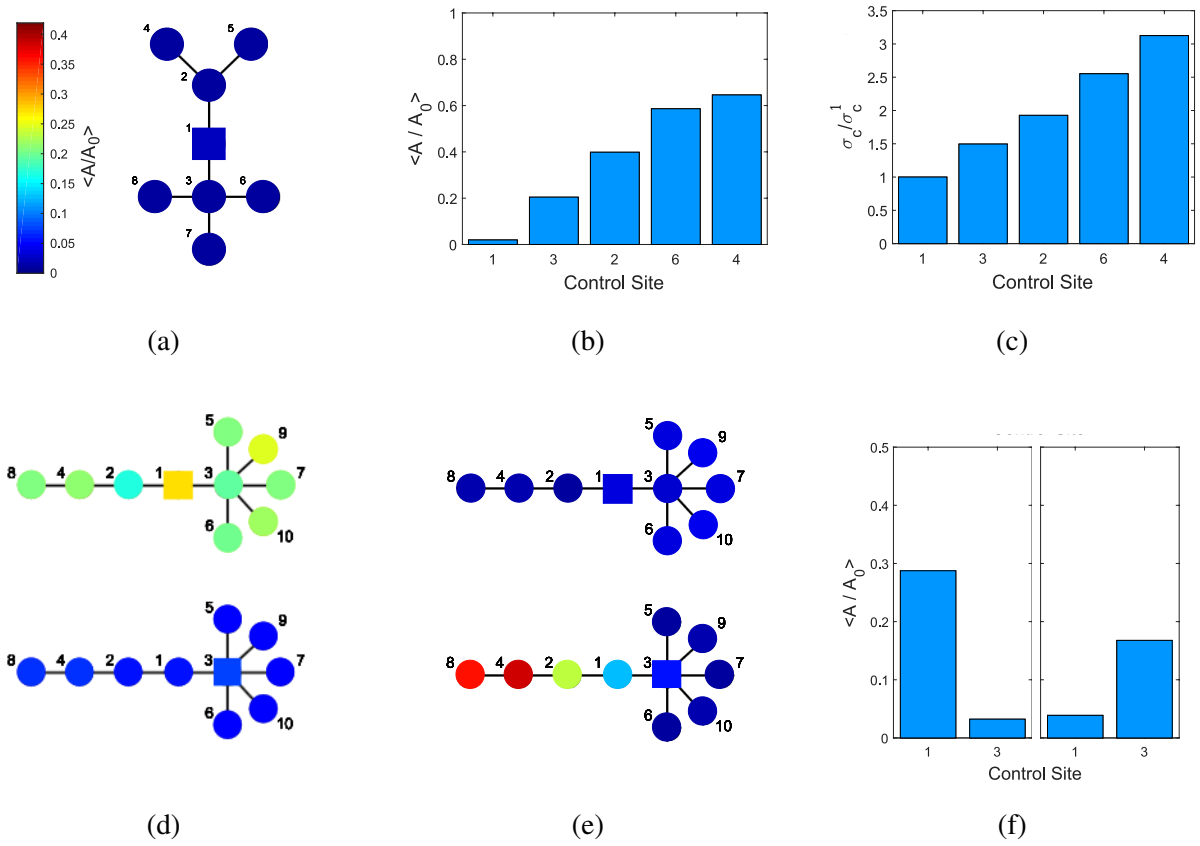

Figure 6.6: Experiments: pinning control of large networks; $R_{\text{ind}} = 1$ kΩ. (a) Eight-electrode tree network, with node 1 as the optimal site. The color represents the mean percent of the natural amplitude; V = 1110 mV, $\sigma = 1$ mS, $K = 5.4$ A/V. (b) Mean amplitude for various control nodes at K sufficient to control the network by the optimal control node. (c) The quotient σ_c/σ_c^1 for each control site, where $\sigma_c^1 = \sigma_{c-\min}$. (d) Ten-electrode degenerate tree network in the limit of K_c (strong σ); V = 1090 mV, $\sigma = 2$ mS, $K = 2.4$ V/A. The square indicates the pinned node. (e) Ten-electrode degenerate tree network in the limit of σ_c (strong K); V = 1090 mV, $\sigma = 0.50$ mS, $K = 5.5$ V/A. The square indicates the pinned node. (f) The mean percent amplitudes in the strong coupling (left) and weak coupling (right).

Figure 6.1), requires an iterative scheme. Here, we propose a systematic and tractable computational procedure:

- Step 1. Obtain the diagonal entries p_{ii} of the matrix P and compute the vector

$$\bar{p} = \frac{1}{\min_i(P_{ii})}(p_{11}, \cdots, p_{nn})' \tag{6.40}$$

- Step 2. Compute the weights $c_j = \|p_j\|_2^2$ for $j = 1, \cdots, n$, where p_j is the j^{th} row of P, then rescale $\bar{p}$ to get

$$\bar{w} = \frac{1}{\min_i(c_i\bar{p}_i)}(c_1\bar{p}_1, \cdots, c_n\bar{p}_n)' \tag{6.41}$$

- Step 3. Compute the difference of the two vectors $z = \bar{w} - \bar{p} = (z_1, \cdots, z_n)'$

- Step 4. Assume k is the index of the optimal pinning site selected by the Lyapunov method with σ_c^k denoting the corresponding critical coupling, then for any $z_i < z_k$, $i = 1, \cdots, n$, compute σ_c^i. If $\sigma_c^i < \sigma_c^k$ then the stability hyperbolas of nodes i and k intersect. Hence, the network is degenerate

The number of nodes satisfying $z_i < z_m$ is much less than the size of the network n, which makes this procedure computational more tractable than computing the critical coupling for all n nodes in the network.

6.6.3 Degeneracy in Directed Networks

Thus far, we have shown that the developed Lyapunov technique for identifying the most influential site in undirected networks works perfectly when the network is not degenerate. The existence of degeneracy in undirected networks is a counterintuitive phenomenon, especially since the coupling is homogeneous and, more importantly, every pinning site has exactly the same critical gain K_c. Intrigued by degeneracy in undirected networks, we then decided to investigate both unweighted

and weighted directed networks, and indeed we found degeneracy in these types of networks as well.

Here, for illustrative purposes we present a 10-node weighted directed network (see Figure 6.7(a)). The adjacency matrix of this network was generated using the following Matlab code,

```
>> A = magic(n)-diag(diag(magic(n)));
>> A(A>45) = 0;
>> A_adj = A./10;
```

Note that for both weighted undirected and directed networks, the critical coupling might have to be redefined, and furthermore, the Laplacian matrix is not symmetric. However, here we consider that the Laplacian dynamics is of the form $\dot{x} = -\sigma L_{\mathrm{i}} x + Bu$, where L_{i} is the Laplacian matrix of the weighted directed network, such that the definitions of the critical coupling and gain, given in Supplementary Note 4, remain valid. The Laplacian matrix is computed as $L_{\mathrm{i}} = D_{\mathrm{i}} - A_{\mathrm{adj}}$, where D_{i} is a diagonal matrix of indegrees.

In order to determine whether this network was degenerate or not, we started by plotting the stability hyperbolas for all the nodes, as depicted in Figure 6.7(b). In addition, we numerically computed the critical coupling σ_c and critical gain K_c for each node. These values are stored in the following two vectors:

$$\boldsymbol{\varsigma_{\mathbf{c}}} = (1.52, 1.23, 2.60, 2.28, 1.91, 0.94, 1.02, 1.02, 0.85, 0.44),$$

and

$$\boldsymbol{\kappa_{\mathbf{c}}} = (10.53, 8.83, 14.8, 10.21, 10.73, 9.12, 10.32, 8.19, 9.53, 10.19),$$

where $\boldsymbol{\varsigma_{\mathbf{c,i}}}$ and $\boldsymbol{\kappa_{\mathbf{c,i}}}$ are the critical coupling and gain of the i^{th} node, for $i = 1, \cdots, 10$. From the hyperbolas, one can clearly see that node 10 is the most influential when the coupling σ is weak and the feedback gain K is strong. However, as the coupling σ gets stronger and the gain K gets

weaker, node 10 progressively loses its position of influence and ends up in 5^{th} position behind nodes $8, 2, 6$ and 9.

To demonstrate the impact that the switching of control sites has on the dynamical response, we proceed with simulations of this network, with Stuart-Landau oscillators (Figure 6.7(c)-(d)). We started by controlling the network using node 8 as the pinning site, and fixed the values of the gain $K = 10$ and coupling $\sigma = 100$ (strong coupling regime). With K and σ fixed, we then proceeded with node 10 as the control site; and for both control sites (i.e., node 8 and node 10), we show the mean oscillation amplitude in Figure 6.7(c). We repeated the simulation, but this time with $K = 100$ and $\sigma = 1.5$ (weak coupling regime) and the results are shown in Figure 6.7(d). These simulation results show that node 8 performs better when the coupling σ is strong (as predicted by the hyperbolas in Figure 6.7(b)), whereas, node 10 performance is poor. However, once the values of K and σ switched, the performance of node 10 becomes better than the performance of node 8. This example shows the importance of knowing whether a network is degenerate and how to select the optimal control site depending of the strength of the coupling.

6.6.4 Degeneracy in Undirected Networks with Two Pinning Sites

We have discovered the existence of degenerate directed and undirected networks with a single control site, however, degeneracy is not a property exclusive to single site controlled networks. Here, we present two networks that are controlled using two pinning sites and for which we have observed the switching of optimal control site pairs. We first present a 55-node tree network shown in Figure 6.8. In this network, using a search algorithm, we found that the optimal control sites in the weak coupling regime are given by the pair of nodes $(1, 45)$, and the corresponding critical coupling is $\sigma_c = 20.42$ with the critical gain $K_c = 27.5$, given by (6.28). In the strong coupling

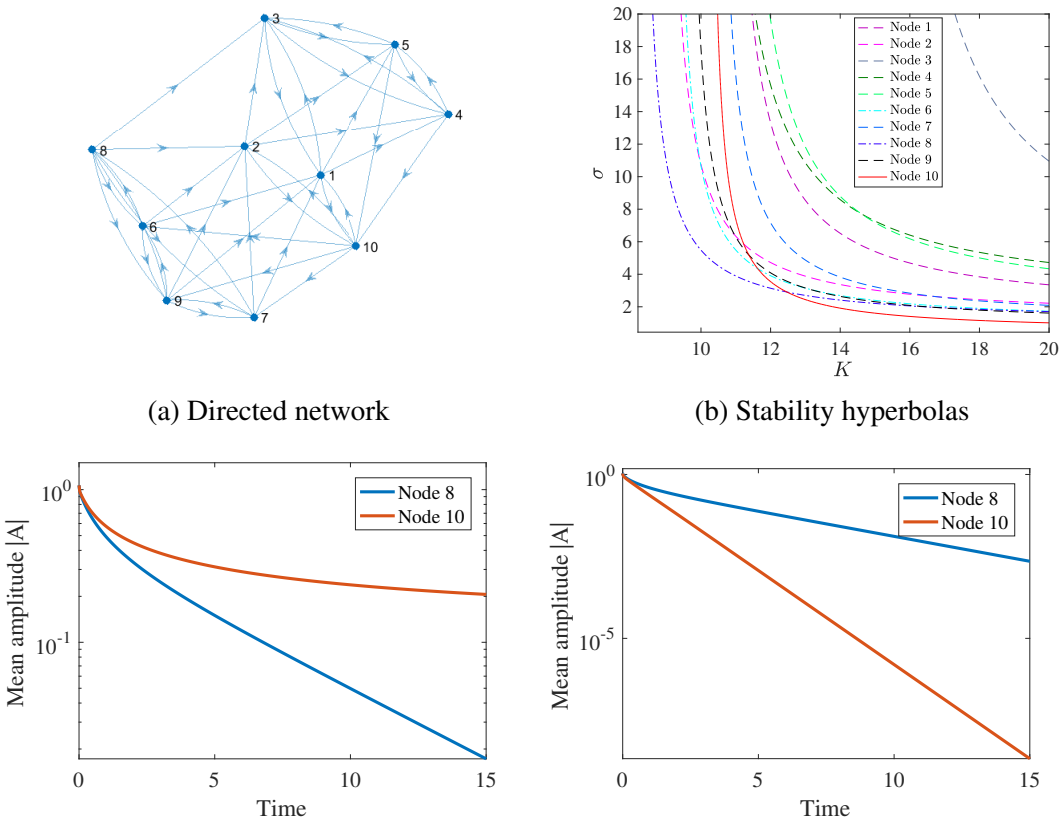

(a) Directed network

(b) Stability hyperbolas

(c) Strong coupling simulations

(d) Weak coupling simulations

Figure 6.7: Illustration of a degenerate directed network. (a) Directed graph with ten nodes. (b) Stability hyperbolas. (c) and (d) Mean oscillation amplitudes of the network in high coupling ($\sigma = 100$, $K = 10$) and low coupling ($\sigma = 1.5$, $K = 100$) regimes, respectively. For strong σ, node 8 is the most influential, whereas for weak σ, node 10 is the most influential.

regime, on the other hand, we found that the pair $(2,45)$ (with $\sigma_c = 28.67$) becomes the optimal control pair. We notice a shift of the first control site from node 1 (with node degree $\gamma = 7$) to node 2 (with $\gamma = 18$).

The second example in Figure 6.9(a) shows a 35-nodes ER network that also has control pairs with intersecting hyperbolas (see Figure 6.9(b)). Similar to the previous example, we found the optimal pair in the weak coupling regime, given by $(25,32)$ (with $\sigma_c = 3.87$) and in strong coupling

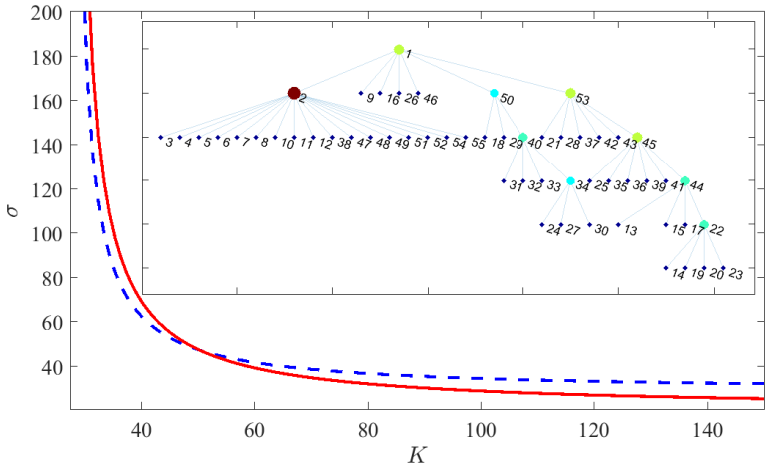

Figure 6.8: Illustration of degeneracy in an undirected Tree network with two pinned nodes. (a) Graph of the 55-nodes network. (b) Stability hyperbolas. The hyperbola in red corresponds to the control pair $(25,32)$, whereas the blue one corresponds to the pair $(3,25)$.

regime, given by $(3,25)$ (with $\sigma_c = 4.09$). Once again, we observe a switch of one of the control sites, specifically, from node 32 (with $\gamma = 5$) to node 3 (with $\gamma = 7$) as the coupling strengthens.

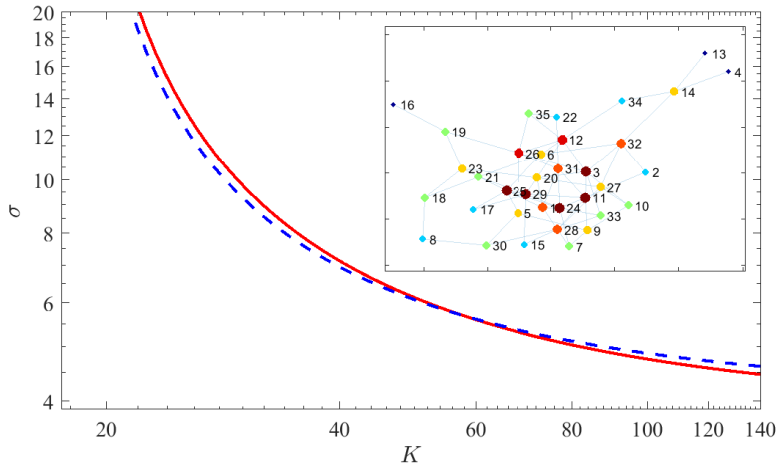

Figure 6.9: Illustration of degeneracy in an Erdős-Rényi undirected network with two pinned nodes. (a) Graph of the 35-nodes ER random network. (b) Stability hyperbolas. The hyperbola in red corresponds to the control pair $(25,32)$, whereas the blue one corresponds to the pair $(3,25)$.

An important observation from these two examples is that, in strong coupling regimes, the node degree γ becomes more influential. Before giving a plausible explanation for this phenomenon,

first, we observe that the control site with the lower node degree has the shortest maximum path or distance (see the inset in Figure 6.8, for example). Referring to the same figure for clarity, observe that the distance of node 1 to the farthest nodes (14,19,20 and 23) is 5, while it is 6 for node 2. So, in the weak coupling regime (where the node dynamics are not necessarily synchronized) the control influence from node 1 has to travel a shorter distance before reaching all the nodes. The control influence from node 2, on the other hand, can immediately reach 18 nodes directly connected to node 2, however, it has to travel longer distances, passing through node 1, before reaching the rest of the network. It is also important to note that there is an inherent delay in the propagation of the control influence from one node to another because the node dynamics are not synchronized due to weak coupling. Hence, in this case we can see that the node with the shortest path has the most influence. However, when the coupling strength is strong, the node dynamics quickly synchronize, and hence reducing or eliminating the propagation delay observed in weak σ. This is advantageous for node 2 which has already 18 nodes that easily and quickly synchronize to it; therefore, the control influence is also transmitted to the rest of the network without difficulties. To conclude, the control site with high node degree influences more nodes rapidly without requiring a large amount of feedback gain.

Chapter 7

Conclusion

7.1 Iterative Control Methods

In Chapter 2, a convergent iterative method for solving optimal tracking control problems, for bilinear systems, with quadratic cost functional is proposed. The developed control algorithm is versatile, and allows for the design of optimal tracking control as well as minimum energy control laws. In addition, with minor modifications, it can be used for the design of bounded control inputs. Furthermore, we prove the convergence of the iterative control algorithm and provide sufficient conditions for a local or global optimal control to exists. The effectiveness of the proposed method is demonstrated through numerous examples, using different bilinear systems, that show fast convergence and better performance than some algorithms in the literature. This simple to implement algorithm, that also applies to ensemble bilinear systems, can find many practical applications, for example, for synthesizing optimal pulse sequences in nuclear magnetic resonance spectroscopy and imaging.

The work in Chapter 3 extends the iterative control algorithm, for bilinear systems, presented in Chapter 2 to oscillating systems that can be reduced to phase model descriptions. In particular, we

leverage phase reduction theory to reduce the complexity of the control problem by reducing the dimensions of the dynamical system, e.g., the Hodgkin-Huxley neuron model. Furthermore, we showed by computing the iterated Lie brackets that, for ensemble controllable neuron or oscillator systems, the developed control algorithm can be used to synthesize control inputs that manipulate the phases or frequencies of the oscillators such that coherent and meaningful complex spatiotemporal phase patterns can be formed.

This control algorithm has potentially a wide range of applications, from treatment of neural pathologies such as Parkinson's disease and epilepsy [194, 195] to design of neurocomputers [143, 196]. The robustness of the open-loop control will allow us to overcome some of the practical challenges of experimental implementation, namely, the difficulty to collect states information necessary to form a feedback control law. Furthermore, the control of a large number of neural oscillators with a single global control will have a significant impact in application such the retinal implants by reducing the number of required electrodes transmitting visual information to the visual cortex through optic neurons. Although the core of this work considered neuron oscillator models, the methods and analysis presented in Chapter 3 are applicable to any limit-cycle oscillator, e.g., pulsating cardiac cells that generate the heartbeats and which are often modeled by reaction-diffusion systems [126]. As future directions, we would like to investigate the robustness of the iterative control algorithm in experiments, and in presence of uncertainty and parameter dispersions.

7.2 Novel Modeling and Control Paradigms of Cyclic Loads

The Chapters 4 and 5 present a new modeling and control paradigm for thermostatically controlled loads (TCLs) using neuroscience-inspired oscillator modeling and phase model reduction theory.

The simplicity of the TCL phase model opens the door to a rich variety of analysis tools and control strategies that could improve the way in which TCLs are operated to provide demand response (DR) on a power distribution system. Indeed, one of the main challenges in control of TCLs, that limit the capacity and time scale of ancillary services (AS), is synchronization which leads to unwanted power fluctuations. In Chapter 4 we show that the concept of Arnold tongues, which is a tool of choice for analyzing synchronization of oscillators, can be used to, more accurately, estimate AS capacity and time scale that a given TCL population can provide to support power grid stability. Furthermore, we use Arnold tongues to characterize the performance of control policies tracking sinusoidal reference power signals.

In Chapter 4, as a proof of concept, we propose a PRC-based open-loop controller that is used to track a reference power signal. Open-loop control of TCLs is appealing given that, by not requiring feedback, it eliminates the need to establish two-way communication channels (reducing the cost) and privacy concerns that have been raised. However, the proposed PRC-based controller was not optimized. Therefore, taking advantage of the simplification introduced by phase models, which allows the formulation of optimal control problems, in Chapter 5 we develop a minimum energy phase model-based controller for modulating the power consumption of TCLs. This control policy provides demand response on time-scales of interest while satisfying the TCLs operating constraints. Specifically, by keeping constant the frequency at which a load is made to switch on and off in a given time period, this controller will help avoid excessive wear on the equipments. In addition, we show that the response of this controller to a step input slowly affects the mean temperature of the TCLs, which is a more comfortable scenario for the consumers, while keeping power overshoots to a minimum.

As a future directions, we would like to determine the maximum ancillary service capacity that the minimum energy controller can provide and on the appropriate time scales. Furthermore, we would

like to explore the impact of user defined constraints such as bounds on the allowable temperature deviations, and also formulate optimization problems to maximize AS capacity and bandwidth. The application of phase models to evaluate the ability of random on/off switching policies to provide demand response on different time-scales is also promising. Lastly, the use of pinning control strategy in large building with multiple TCLs is also worth investigating.

7.3 Identification of Influential Nodes in Complex Networks

Chapter 6 investigates a significant problem in pinning control of oscillator networks, that is, to identify the most influential site for establishing stable behavior in the network and to unlock what this site is dependent upon i.e., elucidate its dependence on the network structure. We start by establishing the conditions under which stabilization with a single pinning site is achievable. Specifically, our analysis, based on the derivation of the analytical eigenvalue structure of the controlled network and linear stability analysis, reveals that for any complex undirected network, the stable and unstable states are separated by a hyperbolic curve in a phase diagram of K *vs.* σ, which we refer to as the *stability hyperbola*. In general, each possible control site in a network is associated with a stability hyperbola that characterizes the stable region, and the most influential control site (optimal) often has the large stable region. For some network topologies such the chain network, the stability hyperbolas associated with the control sites never intersect, which means that the node with the large stability region, defined by the hyperbola, is the global optimal control site.

However, the work in Chapter 6 has led to the discovery of degenerate networks, i.e., the most influential node switches from one node to another according to the strength of the coupling between nodes. This counterintuitive phenomenon is observed in both computer generated and real-world networks, such as social and power grid networks. We further show that in a degenerate network, a

node that is most influential and which can stabilize the network dynamics when the coupling between different units is strong, may no longer be the most influential when the coupling weakens. We use dynamic simulations of a directed network of ten Stuart-Landau oscillators to demonstrate this phenomena. Moreover, a computationally efficient method (called LBM) was developed to identify the global optimal and the candidate optimal pinning sites for stabilization of a nondegenerate and a degenerate complex undirected network, respectively. The theoretical development was confirmed in experiments with networks of chemical reactions, where oscillations in the networks were effectively suppressed through pinning of a single reaction site determined by the computational method.

The developed methods are directly applicable to identify and control the so-called influential spreader [197], for instance, to determine the foci and dosage required for immunization in an epidemic network [198] or locate optimal pacemaker position for synchronization [199, 200]. The relocation of influent network nodes due to the change in coupling strengths could be of particular importance for tree-like networks, which are often used for efficient distribution of resources, e.g., in the nephrons of kidney [201]. The development of an efficient computational method for determining, simultaneously, multiple control sites in pinned networks is left for future investigation.

Appendix A

Proofs of Bounded Solutions

The proof of convergence in Section 2.2.2 rely on the fact that one can find finite bounds for α_i and β_i with $i \in \mathbb{N}$. In appendix A.0.1, we show that all the norms of matrix and vector valued functions that define the β_i coefficients are bounded, and in appendix A.0.2, we show how the α_i are obtained.

A.0.1 β-Coefficients

Since, we are dealing with a finite-time optimal control problem, it can be shown that for a finite time horizon T the following norms are bounded, $\|\Phi(t,\sigma)\|, \|x_k(t)\|, \|E_k(x)\|, \|g_k(t)\|$, and $\|P_k(t)\|$. Indeed, a bound on the transition matrix as shown in [107] is given by

$$\|\Phi(t,\sigma)\| \leq \alpha_0(|t-\sigma|) = \gamma_1, \quad \forall t,\sigma \in [0,T], \tag{A.1}$$

where $\alpha_0 \in \mathbb{R}$. Suppose that $x_k(t)$ is in the reachable set $\mathcal{R}(t;\hat{x}(t_0),t_0,\mathcal{U})$, there exists a control $u(t) \in \mathcal{U}$ such that

$$x_k(t) = \Phi(t,t_0)\{\hat{x}(t_0) + \int_{t_0}^{t} \Phi(t_0,\sigma)B(\sigma)u(\sigma)d\sigma\}. \tag{A.2}$$

Since all the entries in Φ and B are continuous on $[t_0,T]$, it follows that there exists numbers L_1 and L_2 such that $\|\Phi(t,t_0)v_1\| \leq L_1\|v_1\|$ and $\|\Phi(t,\sigma)B(\sigma)v_2\| \leq L_2\|v_2\|$ for all $v_1 \in \mathbb{R}^n$, $v_2 \in \mathbb{R}^m$, and $t,\sigma \in [t_0,T]$. It then follows that

$$\|x_k\| \leq L\{\|x_k(0)\| + (t-t_0)MN\} = \gamma_2, \tag{A.3}$$

where $M = \sup_{\sigma\in[t_0,T]}\|u(\sigma)\|$. Consider $E_k(x) = (\bar{B}+\{xN\}_k)R^{-1}(\bar{B}+\{xN\}_k)'$, where $\{xN\}_k = (\sum_{j=1}^n x_j N_j)_k$. It follows that

$$E_k(x) = \bar{B}R^{-1}\bar{B}' + \bar{B}R^{-1}\{xN\}_k' + \{xN\}_k R^{-1}\bar{B}' + \{xN\}_k R^{-1}\{xN\}_k'. \tag{A.4}$$

Given that $\bar{B}$ and N_j are constant matrices, and R is positive definite while $\|x_k\|$ is bounded, by the triangle inequality it follows that

$$\|E_k(x)\| \leq \|\bar{B}R^{-1}\bar{B}'\| + \|\bar{B}R^{-1}\{xN\}_k'\| + \|\{xN\}_k R^{-1}\bar{B}'\| + \|\{xN\}_k R^{-1}\{xN\}_k'\| \leq \gamma_3. \tag{A.5}$$

Similar arguments as used to show that $\|x_k\| < \gamma_2$ can be used to show that $\|g_k(t)\| < \gamma_4$ for all $t \in [t_0, T]$, since (2.11) is the adjoint to the system dynamics in (2.14).

The Kalman conditions (i)-(iii) in Theorem 3 guarantee the existence of a bounded solution $P(t)$ to the Riccati equation in (2.10) $\forall\, t \leq T$. Hence, one can find an upper bound such that $\|P_k(t)\| \leq \gamma_5$.

A.0.2 α-Coefficients

The norm of the difference

$$\begin{aligned}\|E_k(x) - E_{k-1}(x)\| &= \|\bar{B}R^{-1}\{xN\}_k' - \bar{B}R^{-1}\{xN\}_{k-1}' + \{xN\}_k R^{-1}\bar{B}' - \{xN\}_{k-1}R^{-1}\bar{B}' \\ &\quad + \{xN\}_k R^{-1}\{xN\}_k' - \{xN\}_{k-1}R^{-1}\{xN\}_{k-1}'\| \\ &\leq \alpha_1 \xi_{k-1}(t),\end{aligned} \tag{A.6}$$

is bounded, where $\alpha_1 = \left[\sum_{j,k=1}^n \|N_j R^{-1} N_k'\|^2\right]^{1/2}(\|x_{k-1}\| + \|x_{k-2}\|) + \left[\sum_{k=1}^n \|\bar{B}R^{-1}N_i' + N_R^{-1}\bar{B}'\|^2\right]^{1/2}$ and $\xi_{k-1}(t) = \|x_{k-1} - x_{k-2}\|$. To obtain the bound on $\|P_k - P_{k-1}\|$, let's write

$$\frac{d}{dt}(P_k - P_{k-1}) + (P_k - P_{k-1})(A - E_k P_k) + (A - E_k P_k)'(P_k - P_{k-1}) + P_{k-1}(E_{k-1} - E_k)P_k = 0. \tag{A.7}$$

Then, integrating (A.7) backward in time gives

$$P_k - P_{k-1} = \int_t^T \Phi(\sigma, t)[P_{k-1}(E_{k-1} - E_k)P_k]\Phi(\sigma, t)d\sigma. \tag{A.8}$$

After taking the norm on both sides, it follows

$$\|P_k - P_{k-1}\| \leq \int_t^T \gamma_6 \|E_k - E_{k-1}\| d\sigma, \tag{A.9}$$

where $\gamma_6 = \|\Phi'(\sigma,t)\|\|P_{k-1}\|\|P_k\|\|\Phi(\sigma,t)\|$.
Substituting (A.6) into (A.9) yields

$$\|P_k - P_{k-1}\| \leq \int_t^T \alpha_1\gamma_6 \|x_{k-1} - x_{k-2}\| d\sigma = \alpha_2 \xi_{k-1}, \tag{A.10}$$

where $\alpha_2 = \int_t^T \alpha_1\gamma_6 d\sigma$.
Finally, to obtain the bound on $\|g_k - g_{k-1}\|$, let's write

$$\frac{d}{dt}(g_k - g_{k-1}) = -(A - E_kP_k)'g_k - Wz + (A - E_{k-1}P_{k-1})g_{k-1} + Wz. \tag{A.11}$$

Adding and subtracting $[A - E_kP_k]'g_{k-1}$ to (A.11), one obtain

$$\frac{d}{dt}[g_k - g_{k-1}] = -[A - E_kP_k]'g_k + [A - E_{k-1}P_{k-1}]g_{k-1} + [A - E_kP_k]'g_{k-1} - [A - E_kP_k]'g_{k-1}. \tag{A.12}$$

After some algebraic manipulation, one obtains

$$[\dot{g}_k - \dot{g}_{k-1}] = [A - E_kP_k]'[g_k - g_{k-1}] - [E_{k-1}P_{k-1} - E_kP_k]'g_{k-1}. \tag{A.13}$$

Integrating backward in time with $g_k(T) - g_{k-1}(T) = 0$, gives

$$g_k - g_{k-1} = \int_t^T \Phi_k'(t,\sigma)[E_kP_k - E_{k-1}P_{k-1}](\sigma)g_{k-1} d\sigma, \tag{A.14}$$

then, after taking the norm on both sides and knowing that $\|E_kP_k - E_{k-1}P_{k-1}\| \leq \gamma_7 \xi_{k-1}(t)$, it follows that

$$\|g_k - g_{k-1}\| \leq \int_t^T \gamma_7 \|\Phi_k'(t,\sigma)\|\|g_k(\sigma)\| \xi_{k-1} d\sigma = \alpha_3 \xi_{k-1}, \tag{A.15}$$

where $\alpha_3 = \int_t^T \gamma_7 \|\Phi_k'(t,\sigma)\|\|g_k(\sigma)\| d\sigma$.

Appendix B

Control of Spatiotemporal Patterns Supplement

B.1 Iterative Control of Phase Models

Consider the phase model (3.2) or equivalently the nonlinear system (3.3). These two equations are both affine in the control input $u(t)$, but for the phase model (3.2), $f(\theta)$ can either be a constant $f = \omega$ or a nonlinear function of the phase variable θ, i.e., $f = f(\theta)$. We previously developed an iterative method for designing optimal tracking control inputs for bilinear systems [103] of the form $\dot{x} = f(x) + u(t)g(x)$, where $f(x) = A(t)x(t)$ is linear. Here, we extend the control algorithm to accommodate ensemble phase models, with constant and nonlinear baseline dynamics $f(\theta)$.

B.1.1 Optimal Tracking Control Problem for Phase Model Systems

Consider the tracking problem of the following phase model ensemble,

$$\dot{\Theta}(t) = f(\Theta) + Z(\Theta)u(t), \tag{B.1}$$

where $\Theta(t) = (\theta_1, \theta_2, \cdots, \theta_n)' \in \Omega \subset \mathbb{R}^n$, $f, Z : \Omega \to \mathbb{R}^n$ and $u(t) \in \mathcal{U} \subset \mathbb{R}$. Let $\Theta_d(t) \in \mathbb{R}^n$ be the desired phase trajectory vector. The aim is to control the system in (B.1) such that the phase variables, θ_i's, track the desired phase trajectories, $\theta_{i,d}(t)$, as close as possible in the time interval $[0, T]$, with minimum control effort. Let's define the error vector as $e(t) = \Theta_d(t) - \Theta(t)$, the control

law is then obtained by solving the optimization problem

$$\begin{aligned} \min_{u\in\mathcal{U}} \quad & J = \varphi(T,e(T)) + \int_0^T \mathcal{L}(e(t),u(t))dt, \\ \text{s.t. } & \dot{\Theta}(t) = f(\Theta) + Z(\Theta)u(t), \\ & \Theta(0) = \Theta_0,\ \Theta(T) \text{ is free,} \end{aligned} \tag{B.2}$$

where $\varphi : \mathbb{R}\times\mathbb{R}^n \to \mathbb{R}$, denoting the terminal cost, and $\mathcal{L} : \mathbb{R}\times\mathbb{R}^n \to \mathbb{R}$, denoting the running cost. The terminal and running costs are $\varphi(T,e(T)) = \frac{1}{2}e'(T)Fe(T)$ and $\mathcal{L}(e(t),u(t)) = \frac{1}{2}e'(t)Q(t)e(t) + u'(t)R(t)u(t)$, where the matrices $F \succeq 0$ and $Q(t) \succeq 0$ are $n\times n$ positive semidefinite, and $R(t) \in \mathbb{R}$ is positive definite, $\forall t \in [0,T]$.

B.1.2 Optimal Control Solution

Let $V(t,\theta)$ be the value function associated with the optimal control problem of the system in (B.1) with the cost functional $J(u)$ in (B.2), then $V(t,\theta) = \inf_{u\in\mathcal{U}_{(t,\theta)}} J(u)$ over all admissible controls $u : [0,T] \to \mathcal{U} \subseteq \mathbb{R}^m$. If V is differentiable with respect to (t,θ), then by minimizing the Hamiltonian of the system over all admissible controls, one obtains the HJB equation [106, 202], given by

$$V_t + \min_{u\in\mathcal{U}}\left\{V_\theta\left(f(\Theta) + Z(\Theta)u\right) + \frac{1}{2}(e'Qe + u'Ru)\right\} \equiv 0, \tag{B.3}$$

where $V_t = \frac{\partial V}{\partial t} \in \mathbb{R}$ and $V_\theta = \frac{\partial V}{\partial \theta} \in \mathbb{R}^{1\times n}$. The necessary condition of optimality gives

$$u(t) = -R^{-1}Z(\Theta)'V_\theta'. \tag{B.4}$$

Substituting for $e(t)$ and $u(t)$ in (B.3) yields

$$V_t + \frac{1}{2}\left\{\left(V_\theta f(\Theta) + f(\Theta)'V_\theta'\right) - V_\theta E V_\theta' + (\Theta'Q\Theta) + (\Theta_d'Q\Theta_d) - (\Theta'Q\Theta_d + \Theta_d'W\Theta)\right\} \equiv 0, \tag{B.5}$$

where $E(\Theta) = Z(\Theta)R^{-1}(t)Z'(\Theta)$. Suppose that a candidate solution of (B.5) is of the form

$$V(t,\Theta) = \frac{1}{2}\Theta^{*\prime}(t)P(t)\Theta^*(t) - \Theta^{*\prime}(t)g(t) + h(t), \tag{B.6}$$

where $\Theta^*(t)$ is the optimal state trajectory, $P(t) \in \mathbb{R}^{n\times n}$, $g(t) \in \mathbb{R}^n$, and $h(t) \in \mathbb{R}$. Taking the partial derivatives of (B.6) with respect to Θ and t, one obtains

$$\begin{aligned} V_\theta(t) &= P(t)\Theta^*(t) - g(t), \\ V_t(t) &= \frac{1}{2}\Theta^{*\prime}(t)\dot{P}(t)\Theta^*(t) - \Theta^{*\prime}\dot{g}(t) + \dot{h}(t). \end{aligned} \tag{B.7}$$

Substituting (B.7) into (B.5) yields after some algebraic manipulations

$$\frac{1}{2}\Theta^*\{\dot{P} - PEP + Q\}\Theta^* + \dot{h} + \frac{1}{2}\Theta_d' Q\Theta_d - \frac{1}{2}gEg + \Theta^{*\prime}\{-\dot{g} + PEg - Q\Theta_d + Pf(\Theta)\} - g'f(\Theta) \equiv 0, \tag{B.8}$$

where, for simplicity, we dropped the time dependence (t) on the phase variable $\Theta^*(t)$. Now, (B.8) must be satisfied for all $\Theta^*(t)$, $\Theta_d(t)$ and $t \in [0, T]$. Hence, one obtains the following set of coupled differential equations that characterize the optimal solution of the tracking problem,

$$\dot{P}(t) = P(t)E(\Theta)P(t) - Q(t), \tag{B.9}$$

$$\dot{g}(t) = P(t)E(\Theta)g(t) + P(t)f(\Theta) - Q(t)\Theta_d(t), \tag{B.10}$$

$$\dot{h}(t) = g'f(\Theta) + \frac{1}{2}(g'E(\Theta)g - \Theta_d'(t)Q(t)\Theta_d(t)), \tag{B.11}$$

with the respective boundary conditions, $P(T) = F$, $g(T) = F\Theta_d(T)$, and $h(T) = \Theta_d'(T)F\Theta_d(T)$. In addition, the optimal feedback control law is of the form

$$u^*(t) = -R^{-1}Z'(\Theta^*)\left[P(t)\Theta^*(t) - g(t)\right], \tag{B.12}$$

and the optimal trajectory is given by

$$\dot{\Theta}^*(t) = f(\Theta) - E(\Theta^*)\left[P(t)\Theta^*(t) - g(t)\right]. \tag{B.13}$$

The set of differential equations (B.9), (B.10), (B.12) and (B.13) are then used in Algorithm 2 (see Appendix B.2) to iteratively solve for the optimal solution.

One should note that although the solution presented here is for designing tracking controls, it is also possible to design minimum energy controls as well when tracking a particular state trajectory is not required. To accomplish this, one needs to set the penalty matrix $Q = 0$, and then penalize the control energy and the final state through the matrices R and F, respectively.

B.2 Iterative Algorithm for Optimal Tracking Problems

The optimal control problem formulated in (B.2) is solved iteratively using algorithm 2.

Data: $f(\Theta)$, $Z(\Theta)$, $Q(t)$, $R(t)$, F, $\Theta(t_0)$, $\Theta_d(t)$, T
Initialization ;
$k = 0$;
$\Theta_0(t) = \Theta_d(t)$, $\Theta_0(0) = \Theta_d(0)$;
while $||\Theta_k(t) - \Theta_{k-1}(t)|| > \varepsilon$ **do**
    compute $P_k(t)$ and $g_k(t)$ using $Z(\Theta_k(t))$;
    $u_k(t) = -R^{-1}Z'(\Theta_k(t))[P_k(t)\Theta_{k+1}(t) - g_k(t)]$;
    $\dot{\Theta}_{k+1}(t) = f(\Theta_{k+1}(t)) + Z(\Theta_k(t))u_k(t)$;
    $k = k + 1$;
end

Algorithm 2: Algorithmic description of the iterative method

B.3 Control of Uncoupled Oscillators

The control algorithm 2 has a wide range of applications besides the ones mentioned in Chapter 3. It can be used to design stimuli that synchronize or desynchronize an ensemble of oscillators, and even change their oscillation frequencies. Here, we present a few canonical examples using some popular neuron models in neuroscience and neuroengineering, namely, the Hodgkin-Huxley (HH) and the Morris-Lecar (ML) Neuron Model. The control inputs in this section were computed using (B.12), then applied as an open-loop control to the full state model, e.g., the HH and ML differential equations, which demonstrate the robustness of the control algorithm.

B.3.1 Spiking Time Control of a Single Neuron

For this application we use the HH model, a four dimensional system of differential equations (see Appendix B.6) that models the propagation and initiation of action potential in squid axon [118]. Phase reduction theory makes it possible to reduce such complex system of differential equations

to a simple scalar phase model with baseline dynamics $f = \omega$. The PRCs of the HH model and the voltages as a function of the phase for different parameter values are shown in Figure B.1(a).

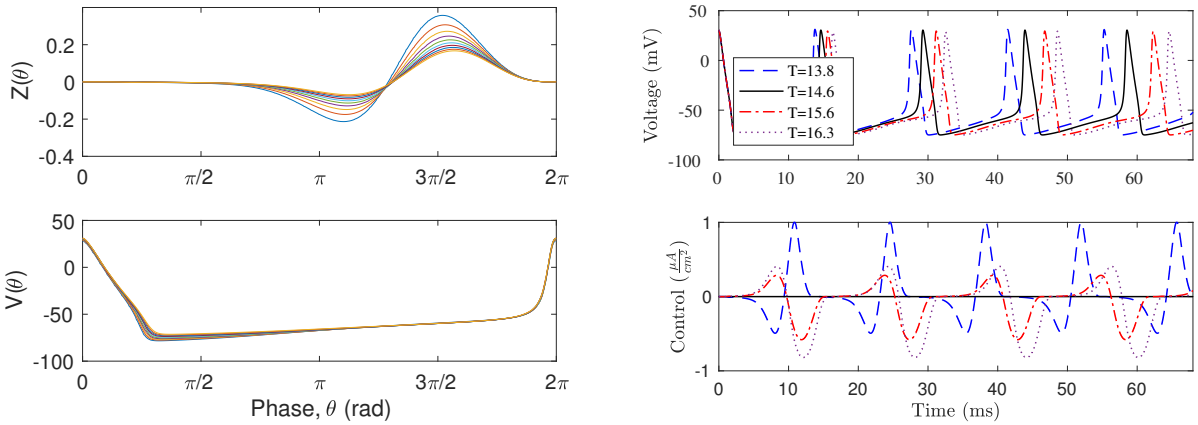

(a) (b)

Figure B.1: Hodgkin-Huxley neuron model simulations. (a) Phase sensitivity functions $Z(\theta)$ and membrane voltages as function of the phase $V(\theta)$. The parameters of the ensemble of HH neurons were distributed within 2% of the nominal values. (b) Controlled spiking train of Hodgkin-Huxley model. The voltage of the uncontrolled neuron spikes every $T_0 = 14.6$ ms, and the three controlled neurons spike every $T = 13.8$ ms, $T = 15.6$ ms and $T = 16.3$ ms, respectively. The corresponding controls are shown in the bottom plot.

The controlled and uncontrolled spiking trains of one neuron are shown in Figure B.1(b). The amplitudes and shape of the controls obtained with our method are consistent with the charge-balanced minimum-power controls in [61], which is an indication of the optimally of the converged solution.

B.3.2 Synchronization and Desynchronization of Neuron Ensembles

The control of neuron ensembles have therapeutic applications such as in Parkinson's disease, where electrical deep brain stimulation is used to mitigate pathological synchronization of a neuron population [47]. Here, we study synchronization and desynchronization of neuron ensembles in finite time $T \ll \infty$.

Synchronization of a neuron population can be achieved by applying a T-periodic control input that forces the phases of the neurons to be the same at the end of each cycle, corresponding to the time $t = kT_u$, where $k = 1,2,3,\cdots$, and T_u is the period of the forcing input. The design of the synchronizing control input can be carried out simply by considering a system of three neurons with natural frequencies corresponding to the minimum, maximum and mean value of the population frequencies. This reduced order design approach is guaranteed to synchronize all the neurons with frequencies within the range of the three nominal values considered as long as the trajectories of these neurons have no crossings when stimulated by a common control input [129]. By designing a control that steers the phases of the three neurons from arbitrary nonzero (but close to zero) initial phases to a common final phase value $\theta(T_u) = 2\pi$ at time $t = T_u$, this will ensure synchronization of the ensemble. The synchronizing control input in Figure B.2(c) was design over one period and then applied repeatedly with period T_u for three cycles.

Similar to the synchronization control design, one can consider three neurons with natural frequencies chosen as previously, and then design a control input that assigns different phases to each neuron at time $t = T_u$ as shown in Figure B.2(a). This control is sufficient for desynchronizing a population of uncoupled neurons. In Figure B.2(c) we applied a synchronizing control for three periods then turn it off for three cycles before applying the desynchronizing control for two periods. One can see that the desynchronizing control greatly speeds up the desynchronization process which was slow during the period of zero input.

This numerical experiment was carried out using the Morris-Lecar neuron model [203], which is a simplified version of the HH neuron model that describes the oscillating voltage of the giant barnacle muscle fiber. The ML system of differential equations is given in Appendix B.5. This is a model that has been extensively used to represent real neurons that are experimentally observable [204]. For the parameter values in Appendix B.5, the neuron fires periodically with a natural frequency $\omega = 0.255$ rad/ms.

B.4 Theorems

Theorem 4: (Versions of Chow's Theorem) Let $\{f_1(\theta), f_2(\theta), \cdots, f_m(\theta)\}$ be a collection of vector fields such that $\{f_1(\theta), f_2(\theta), \cdots, f_m(\theta)\}_{LA}$ is

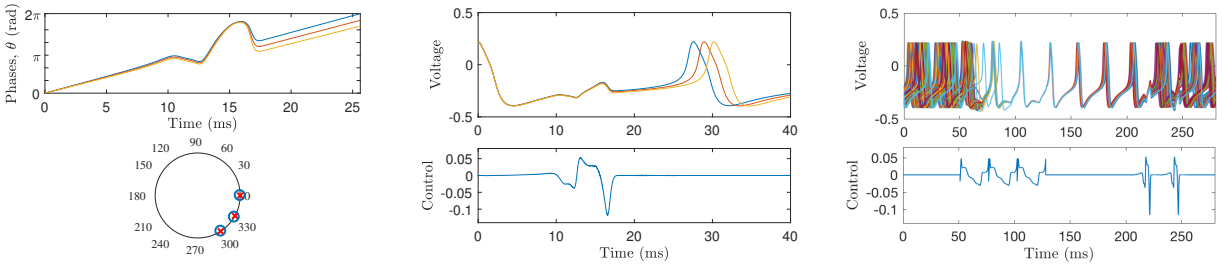

(a) (b) (c)

Figure B.2: Synchronization and desynchronization of neurons. (a) Phase trajectories of the ML phase model undergoing desynchronization (top) and the phases distribution after one period (bottom). The blue circles indicate the target phases and the red crosses indicate the actual final phases. (b) Voltages of three neurons (top) with the desynchronizing control (bottom) applied to the full states ML models. (c) Synchronization and desynchronization of neuron voltages (top) by application a synchronizing control followed by a desynchronizing control (bottom).

a) analytic on an analytic manifold M. Then given any point $\theta_0 \in M$, there exists a maximal submanifold $N \subset M$ containing θ_0 such that $\{\exp\{\theta_i\}\}_G\theta_0 = \{\exp\{\theta_i\}_{LA}\}_G\theta_0 = N$.

b) C^∞ on a C^∞ manifold M with $\dim(\text{span}\{f_i(\theta)\}_{LA})$ constant on M. Then given any point $\theta_0 \in M$, there exists a maximal submanifold $N \subset M$ containing $\theta_0 = N$.

Theorem 5: Suppose that f and g are vector fields on a manifold M. Suppose that $\{f,g\}$ meet either of the conditions of Chow's theorem and suppose that for each initial condition θ_0 the solution of

$$\dot{\theta}(t) = f[\theta(t)]$$

is periodic with a least period $T(\theta_0) < M$. Then the reachable set from θ_0 for $\dot{\theta} = f(\theta) + u(t)g(\theta)$ is $\{\exp\{f,g\}\}_G\theta_0$.

For more details on these two theorems, the reader can refer to [129, 27] and references therein.

B.5 Morris-Lecar Model

The Morris-Lecar neuron equations representing the voltage-gated calcium channel model with a delayed-rectifier potassium channel is described by two coupled dynamical equations,

$$\begin{aligned}
\dot{V} &= \frac{1}{C}[(I_b + I) + g_{Ca} m_\infty (V_{Ca} - V) + g_k w (V_k - V) \\
&\quad + g_L (V_L - V)], \\
\dot{w} &= \phi(\omega_\infty - w)/\tau_w(V), \\
m_\infty &= 0.5[1 + \tanh((V - V_1)/V_2)], \\
\omega_\infty &= 0.5[1 + \tanh((V - V_3)/V_4)], \\
\tau_w &= 1/\cosh[(V - V_3)/(2V_4)].
\end{aligned} \tag{B.14}$$

The variable V is the voltage across the axon membrane, I_b is the base current and I is the control input. The nominal parameter values considered in this dissertation are as follow, $V_1 = -0.01$ mV, $V_2 = 0.15$ mV, $V_3 = 0.1$ mV, $V_4 = 0.145$ mV, $V_k = -0.7$ mV, $V_L = -0.5$ mV, $V_{Ca} = 1$ mV, $g_{Ca} = 1$ mS/cm^2, $g_k = 2$ mS/cm^2, $g_L = 0.5$ mS/c^2, $I^b = 0.09\ \mu$ A/cm^2, $\phi = 0.5$, $C = 1\ \mu$F/cm^2.

B.6 Hodgkin-Huxley Model

The Hodgkin-Huxley model describing the action potentials in the squid giant axon is described by

$$\begin{aligned}
c\dot{V} &= I_b + I(t) - \bar{g}_{Na} h (V - V_{Na}) m^3 - \bar{g}_K (V - V_k) n^4 - \bar{g}_L (V - V_L), \\
\dot{m} &= a_m(V)(1 - m) - b_m(V) m, \\
\dot{h} &= a_h(v)(1 - h) - b_h(V) h, \\
\dot{n} &= a_n(v)(1 - n) - b_n(V) n.
\end{aligned} \tag{B.15}$$

The axon membrane voltage is represented by the variable V, while the ion gating variables are given by m, n and h. The baseline current and control input are given by I_b and I, respectively. The nominal parameters used in this dissertation are $V_{Na} = 50$ mV, $V_K = -77$ mV, $V_L = -54.4$ mV, $I_b = 10\ \mu$A/cm^2, $\bar{g}_{Na} = 120$ mS/cm^2 , $\bar{g}_K = 36$ mS/cm^2, $\bar{g}_L = 0.3$ mS/cm^2 and $c = 1\,\mu$F/cm^2.

Appendix C

Thermostatically Controlled Loads Supplement

C.1 TCL Model with Power and Temperature as Variables

Consider the model in (4.13) with the switching function defined in (4.14) together with the aggregate power equation (4.3). Let $y(t) = 1/\eta s(t)P$ be the instantaneous power drawn by a single TCL. The time derivative of the instantaneous power is given by $\dot{y}(t) = 1/\eta \dot{s}(t)P$. The switching function in (4.14) can also be written using an exponential function as $s(t) = (1+\exp(-kx))^{-1}$. We can then write $x(t)$ in terms of the switching function as

$$x(t) = -\frac{1}{k}\ln\left(\frac{1-s}{s}\right). \tag{C.1}$$

Taking the time derivative of $x(t)$ yields

$$-k\frac{dx}{dt} = \frac{d}{dt}\left(\ln(1-s) - \ln(s)\right). \tag{C.2}$$

Let $u = 1-s$, and by applying the chain rule, we obtain

$$\begin{aligned} -k\frac{dx}{dt} &= \frac{d}{dt}\ln(u) - \frac{d}{dt}\ln(s), \\ &= \frac{d}{du}\ln(u)\frac{du}{dt} - \frac{d}{ds}\ln(s)\frac{ds}{dt}, \\ &= \frac{1}{u}\frac{du}{dt} - \frac{1}{s}\frac{ds}{dt}. \end{aligned} \tag{C.3}$$

After substituting for u and $\frac{du}{dt} = -\frac{ds}{dt}$ in (C.3), we obtain

$$\dot{x} = \frac{\dot{s}}{ks(1-s)}. \tag{C.4}$$

We may now write (C.4) in terms of the instantaneous power, $y(t)$, as follows

$$\dot{x} = \frac{\dot{y}}{k\left(1-\frac{\eta}{P}y\right)}. \tag{C.5}$$

Substituting for (C.5) and (C.1) in (4.13), with $s(t) = \frac{\eta}{P}y$, we obtain

$$\begin{aligned} \dot{y}(t) &= \mu k\left(\frac{\delta_b}{2}\bar{y} - \frac{1}{3}\bar{y}^3 + \vartheta - \vartheta_s\right)\left(1-\frac{\eta}{P}y\right)y, \\ \dot{\vartheta}(t) &= -\frac{1}{CR}\left(\vartheta - \vartheta_a + \eta R y\right), \end{aligned} \tag{C.6}$$

where $\bar{y}(t) = -\frac{1}{k}\ln\left(\frac{P}{\eta y} - 1\right)$.

C.2 Phase Model and Phase Response Curve

Phase reduction theory is a powerful tool for studying multi-dimensional rhythmic systems that are reduced to a scalar differential equation that is much easier to analyze and control. The autonomous oscillatory system is then described by its phase variable ϕ rotating on a circle $\mathbb{S}^1$. This is represented by the phase equation $\dot{\phi}(t) = \omega$. In neuroscience the origin of the phase ϕ is defined as the time since the last spike of a neuron [84], and in our work we define it as the phase corresponding to the time the TCL turns ON. When an oscillator receives a pulse of strength A and duration ΔT, the magnitude of the induced phase shift is given by $\mathrm{PRC}(\phi) = \phi_{\text{new}} - \phi$ [84, 128].

For completeness, we summarize the derivation of the phase model here. More details can be found in [84, 121]. Consider a smooth dynamical system described by

$$\dot{x} = f(x,u), \tag{C.7}$$

where the state variable $x(t) \in \mathbb{R}^n$ and the input $u(t) \in \mathcal{U} \subseteq \mathbb{R}^m$. Suppose that the unforced system $\dot{x} = f(x,0)$ evolves on an attractive periodic orbit $\Gamma \subset \mathbb{R}^n$ with period T. The limit cycle is then described by a non-constant periodic trajectory $\gamma(t) = \gamma(t+T) \in \chi$, $\forall t \geq 0$. The linearized system along the limit cycle is given by

$$\delta\dot{x} = A(t)\delta x(t) + B(t)u(t), \tag{C.8}$$

where $A(t) = \frac{\partial f}{\partial x}(\gamma(t),0)$ and $B(t) = \frac{\partial f}{\partial u}(\gamma(t),0)$ are T-periodic. Given that the limit cycle Γ is a one-dimensional closed curve [84], the position of any point $x_0 \in \Gamma$ can be uniquely described by a scalar phase $\phi_0 \in \mathbb{S}^1 = [0, 2\pi)$ [128]. Let's introduce the phase function $\Theta(x)$ that maps each point x_0 on the limit cycle to its phase $\phi_0 = \Theta(x_0)$. The phase variable $\phi : \mathbb{R}_{\geq 0} \to \mathbb{S}^1$ is defined for each trajectory on the limit cycle as $\phi(t) = \gamma(t + \omega^{-1}\phi_0)$, and is periodic due to the periodicity of $\gamma(t)$.

From the linearized model and the asymptotic phase variable, one can derive the phase-reduced model in a neighborhood of the limit cycle, Γ, for sufficiently small inputs [84, 121]. By differentiating $\phi(t)$ with respect to time in the neighborhood of $\gamma(t)$ using the chain rule, one obtains

$$\begin{aligned}
\frac{d\Theta(x)}{dt} &= \frac{\partial\Theta}{\partial x}(\gamma(t)) \cdot \frac{d}{dt}x(t) + \frac{\partial\Theta}{\partial x}(\gamma(t)) \cdot B(t)u(t), \\
&= \frac{\partial\Theta}{\partial x}(\gamma(t)) \cdot f(x) + \frac{\partial\Theta}{\partial x}(\gamma(t)) \cdot B(t)u(t), \\
&= \omega + Z(\phi) \cdot B(t)u(t),
\end{aligned} \tag{C.9}$$

where we have used to the fact that $\frac{\partial\Theta}{\partial x}(\gamma(t)) \cdot f(x) = \omega$ and $Z(\phi) = \frac{\partial\Theta}{\partial x}(\gamma(t))$ is the phase sensitivity function also referred to as infinitesimal PRC. The input matrix function $B(t)$ depends of the differential equations describing the system, for example $B(t) = (-\mu, 0)$ for the system in (4.13) where the control is a perturbation of the set-point temperature $\vartheta_s(t)$.

In the following we review the main three methods that are commonly used to compute the phase sensitivity function. These techniques are explained with great details and illustrations in [84].

- Winfree's Approach
  In a sufficiently small neighborhood of the limit cycle, the PRC scales linearly with respect to the strength of the pulse. Hence one can write

$$\mathrm{PRC}(\phi, A) \approx Z(\phi)A, \tag{C.10}$$

where $Z(\phi) = \partial \text{PRC}(\phi, A)/\partial A$ at $A = 0$ is the linear response or sensitivity function that quantifies the small change in the instantaneous frequency caused by the weak stimulus that was applied. Now assume that we apply a sufficiently small stimulus $\varepsilon p(t)$ and that the perturbed trajectory remains near the limit cycle attractor at all time. Replacing the continuous input function $\varepsilon p(t)$ with the equivalent pulse train of strength $A = \varepsilon p(t_n)h$, where h is the time between two consecutive pulses, and t_n is the timing of the n^{th} pulse, one can write the Poincaré phase map as $\phi(t_{n+1}) = \{\phi(t_n) + Z(\phi(t_n))\varepsilon p(t_n) + h\}$ mod T, in the form

$$\frac{\phi(t_n + h) - \phi(t_n)}{h} = 1 + Z(\phi(t_n)\varepsilon p(t_n), \tag{C.11}$$

which is a discrete version of

$$\dot{\phi} = 1 + \varepsilon Z(\phi) \cdot p(t), \tag{C.12}$$

in the limit $h \to 0$. Note that the phase model (C.12) is valid for any arbitrary input function $p(t)$. To summarize, Winfree's approach consists of measuring the phase shift induced by a pulse train to determine the PRC.

- Kuramoto Approach

  Kuramoto considered the unperturbed oscillator with $\phi(x)$ denoting the phases of points near its limit cycle attractor. Differentiating $\phi(x)$ using the chain rule yields

$$\frac{d\phi(x)}{dt} = \text{grad } \phi \cdot \frac{dx}{dt} = \text{grad } \phi \cdot f(x),$$

  where grad ϕ is the gradient of $\phi(x)$ with respect to the state vector of the oscillator $x \in \mathbb{R}^n$. However, given that on the limit cycle the flow of the vector field, $f(x)$, is exactly in the direction of the periodic orbit so that $\frac{d\phi(x)}{dt} = 1$, we obtain the important equality

$$\text{grad } \phi \cdot f(x) = 1. \tag{C.13}$$

  By applying the chain rule to the perturbed system

$$\begin{aligned} \frac{d\phi(x)}{dt} &= \text{grad } \phi \cdot \frac{dx}{dt}, \\ &= \text{grad } \phi \cdot \{f(x) + \varepsilon p(t)\}, \\ &= \text{grad } \phi \cdot f(x) + \varepsilon \text{grad } \phi \cdot p(t), \end{aligned} \tag{C.14}$$

and using (C.13), the phase model is obtained as

$$\dot{\phi} = 1 + \varepsilon \text{grad } \phi \cdot p(t). \tag{C.15}$$

Kuramoto phase model (C.15) and Winfree's model (C.12) are equivalent. Hence we have $Z(\phi) = \text{grad } \phi$.

- Malkin's Approach
  Here we formally state Malkin's theorem as in [84]. Suppose the unperturbed oscillator has an exponentially stable limit cycle of period T. Its phase evolution is described by

$$\dot{\phi} = 1 + \varepsilon Q(\phi) \cdot p(t), \tag{C.16}$$

  where Q is a T-periodic function that is the solution to the linear "adjoint" equation

$$\dot{Q} = -\{Df(x(t))'\}Q, \quad \text{with } Q(0) \cdot f(x(0)) = 1, \tag{C.17}$$

  where $Df(x(t))'$ is the transposed Jacobian of the flow f at the point $x(t)$ on the limit cycle, and the normalization condition can be replaced by $Q(t) \cdot f(x(t)) = 1, \forall t$.

The phase models (C.16) and (C.15) or (C.12) are equivalent, hence one can see that

$$Z(\phi) = \text{grad } \phi(x) = Q(\phi). \tag{C.18}$$

The method of the adjoint was used in this dissertation to numerically compute the phase sensitivity function $Z(\phi)$. Examples of computer codes for this method can be found in [84, 128].

C.3 Entrainment Region

The PRC defines the synchronization properties of an oscillator and the synchronized states as fixed points of the corresponding Poincaré phase map [84]. The phenomenon of entrainment by weak forcing of limit-cycle oscillators can be modeled by

$$\dot{\phi} = \omega + AZ(\phi)v(\Omega t), \tag{C.19}$$

where ω and Ω are the natural frequencies of the oscillator, respectively, and the forcing input is $u(t) = Av(\Omega t)$, where v is 2π-periodic with unit energy [65]. The region of existence of a synchronized state is called Arnold tongue [48, 157]. This region of phase-locked states on (Ω, A)-plane shrinks as the intensity A of the stimulus approaches 0, with Ω the frequency of the stimulus. In general, $m : n$ entrainment occurs when $\omega/\Omega \approx m/n$ with positive relative prime integers n and m. This implies that the oscillator rotates exactly m times while the external forcing oscillates n times. Let $\Delta = \omega - \frac{m}{n}\Omega$ and by formal averaging we can write (C.19) as

$$\frac{d\psi}{dt} = \Delta + A\Gamma_{m/n}(\psi), \tag{C.20}$$

where $\psi = \phi - \frac{m}{n}\Omega t$ is a slow varying phase variable, and $\Gamma_{\mathrm{m/n}}(\psi)$ is the interaction function determined by Z and v as

$$\begin{aligned}
\Gamma_{\mathrm{m/n}}(\psi) &= \frac{1}{T_{\mathrm{ext}}} \int_0^{T_{\mathrm{ext}}} Z\left(\psi + \frac{m}{n}\Omega t\right) v(\Omega t) dt, \\
&= \frac{1}{2\pi} \int_0^{2\pi} Z\left(\psi + m\theta\right) v(n\theta) d\psi, \\
&= \frac{1}{2\pi} \langle Z\left(\psi + m\theta\right), v(n\theta) \rangle,
\end{aligned} \tag{C.21}$$

where $T_{\mathrm{ext}} = \frac{2\pi}{\Omega}$ is the period of the external forcing and $\theta = \frac{\Omega t}{n} \in [0, 2\pi)$. Without loss of generality, let $A = 1$ and consider the $1 : 1$ entrainment i.e., $n = m = 1$ and write $\Gamma_{\mathrm{m/n}}(\psi)$ as simply $\Gamma(\psi)$. It can be shown that when the condition

$$\min\ \Gamma(\psi) < -\Delta < \max\ \Gamma(\psi), \tag{C.22}$$

is satisfied, (C.20) has at least two fixed points at which $d\psi(t)/dt = 0$ holds, and one of them is stable [128, 65]. The interval Δ of phase locking for a fixed input strength A decreases as $A \to 0$. So, for different values of A and entrainment ratios m/n one obtains the Arnold tongues as shown in Figure 4.11.

Appendix D

Optimal Placement of Control Sites Supplement

D.1 Geometric Measure of Modal Controllability

In degenerate networks, the optimal control site relocates depending on the strength of the coupling σ between agents. Once we have identified that a network is degenerate, we can use the notion of modal controllability, as described in this section, in conjunction with our proposed Lyapunov method to precisely locate the optimal control site for any given coupling regime.

Proposition 4: The controllability of the i^{th} mode of the dynamical system in (6.37) from the j^{th} input, is proportional to

$$\cos[\theta(v_i, b_j)] = \frac{|v_i^T b_j|}{\|v_i\|\|b_j\|}, \tag{D.1}$$

where v_i is the left-eigenvector associated with λ_i and b_j is the j^{th} column vector of the input matrix B [182].

Clearly, if v_i and b_k are orthogonal the measure is zero, meaning that the i^{th} mode is not controllable from the j^{th} input. This is also a measure of coupling between the mode and the input [182]. Let $cd_j = \cos[\theta(v_i, b_j)]$ be the controllability degree, with $0 \leqslant cd_j \leqslant 1$. The closer cd_j is to 1, the more controllable the i^{th} mode is from the j^{th} input. Hence, the optimal control site can be located by identifying the input that has the highest controllability degree over the first mode (λ_1). Thus, if one wishes to accurately find the optimal pinning site in any coupling regime (from weak to strong) for any type of networks (degenerate or nondegenerate), (D.1) can be applied. However, this method, if

used alone, is computationally expensive because it requires computing the controllability degree for each possible control position in order to determine the optimal site. Hence, for degenerate networks, we propose using this method in conjunction with the Lyapunov method. The latter method will provide a reduced set of nodes from which the most influential one will be identified by using either a search algorithm or the degree of controllability, instead of computing the degree of controllability of all the possible control sites.

The degree of controllability cannot be applied directly to the system in (6.37), because the eigenvector corresponding to the zero eigenvalue has identical components. In order to use the degree of controllability measure on the Laplacian system (6.37), we need to rewrite it in the following form

$$\frac{dx}{dt} = -\bar{G}x - \bar{B}u(t), \tag{D.2}$$

where $\bar{G} = \sigma L + \text{diag}(\delta_1, \cdots, \delta_n)$ and $\bar{B} = (K-1) \times \text{diag}(\delta_1, \cdots, \delta_n)$. Basically, (D.2) has the same form as the LTI system in (6.37), and the degree of controllability measure in Proposition 4 can be computed.

D.2 Experimental Setup

To validate the theory developed in Chapter 6, we conducted several experiments using networks of electrochemical oscillators. The experimental schematic is depicted in Figure D.1. The networks of oscillators were built using an electrochemical cell with a platinum coated titanium rod counter electrode, Hg/Hg_2SO_4/saturated K_2SO_4 reference electrode, a working electrode array of 1 mm diameter nickel wires and 3 M sulfuric acid at a constant temperature of 10°C. The electrodes are connected to a Gill-IK64 multichannel potentiostat through individual resistances ($R_{\text{ind}} = 1$ kΩ), and the potential V of each electrode can be set individually. The electrodes are polarized with a constant overpotential (V_0) and the electrodissolution reaction provides an oscillatory current via a Hopf bifurcation due to a negative differential resistance process (Figure D.1). The oscillating currents from the electrode array are then collected by a Real-time LabVIEW interface at a sampling rate of 1 KHz. To form different network topologies, additional cross resistances (R_c) are placed between electrodes, thus creating the coupling of strength $\sigma = 1/R_c$. Furthermore, the oscillatory reactions of the electrodes can be suppressed through a feedback potential, control signal, that is

generated from the measured currents as shown in Figure D.1, given by

$$V_j(t) = V_0 + K[I_j(t) - \bar{I}_j], \tag{D.3}$$

where $V_j(t)$ is the potential applied to the j^{th} electrode, $I_j(t)$ is the current, $\bar{I}_j$ is a time averaged current, and K is the feedback gain. These experiments are designed such that a variety of network topologies can be constructed by reconfiguring the cross resistances connections, and to allow the control of any node in the network through feedback.

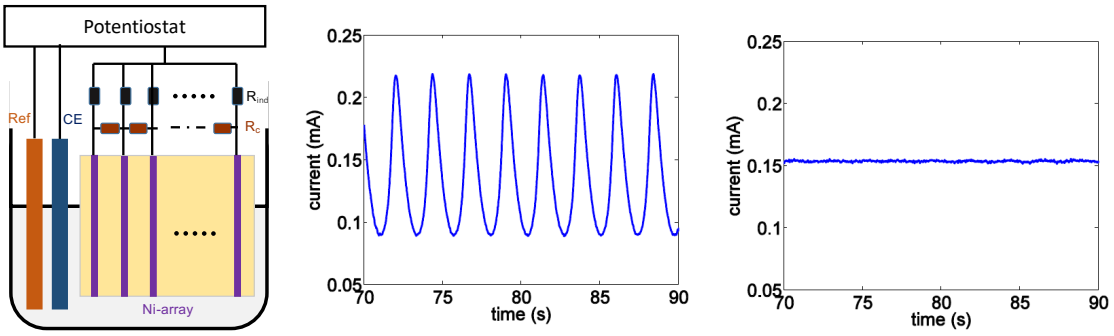

(a) (b) (c)

Figure D.1: Schematic of experimental setup and control of a single electrochemical oscillator. (a) Experimental setup where CE is the counter electrode, Ref is the reference electrode and Ni-array is the working electrode array. The individual resistances are denoted (R_{ind}) and coupling resistances (R_{c}). (b) Current oscillations of a single electrode; V = 1105 mV, $R_{\text{ind}} = 1$ kΩ. (c) Current of a single electrode when feedback is applied with $K = 1.4$ V/A.

References

[1] C. Wrobel, A. Dieter, A. Huet, D. Keppeler, C. J. Duque-Afonso, C. Vogl, G. Hoch, M. Jeschke, and T. Moser, "Optogenetic stimulation of cochlear neurons activates the auditory pathway and restores auditory-driven behavior in deaf adult gerbils," *Science translational medicine*, vol. 10, no. 449, p. eaao0540, 2018.

[2] J. Rauschecker and R. Shannon, "Sending sound to the brain," *Science*, vol. 295, no. 5557, pp. 1025–1029, 2002.

[3] R. R. Mohler and W. Kolodziej, "An overview of bilinear system theory and applications," *IEEE Transactions on Systems, Man and Cybernetics*, vol. 10, no. 10, pp. 683–688, 1980.

[4] R. R. Mohler and C.-N. Shen, "Optimal control of nuclear reactors," 1970.

[5] M. Ekman, "Suboptimal control for the bilinear quadratic regulator problem: Application to the activated sludge process," *IEEE Transactions on Control Systems Technology*, vol. 13, pp. 162–168, Jan. 2005.

[6] J.-S. Li, *Control of inhomogeneous ensembles*. PhD thesis, Harvard University USA, 2006.

[7] J.-S. Li, J. Ruths, and D. Stefanatos, "A pseudospectral method for optimal control of open quantum systems," *The Journal of chemical physics*, vol. 131, no. 16, p. 164110, 2009.

[8] J. Ruths and J.-S. Li, "A multidimensional pseudospectral method for optimal control of quantum ensembles," *The Journal of chemical physics*, vol. 134, no. 4, p. 044128, 2011.

[9] A. Zlotnik, *Optimal Control and Synchronization of Dynamic Ensemble Systems*. PhD thesis, Washington University in St. Louis, 2014.

[10] R. Mohler and W. Kolodziej, "On stochastic bilinear control," in *Decision and Control including the Symposium on Adaptive Processes, 1979 18th IEEE Conference on*, vol. 2, pp. 752–753, IEEE, 1979.

[11] C. Bruni, G. Dipillo, and G. Koch, "Bilinear systems: An appealing class of" nearly linear" systems in theory and applications," *IEEE Transactions on automatic control*, vol. 19, no. 4, pp. 334–348, 1974.

[12] R. W. Brockett, "System theory on group manifolds and coset spaces," *SIAM Journal on control*, vol. 10, no. 2, pp. 265–284, 1972.

[13] R. W. Brockett, "On the reachable set for bilinear systems," in *Variable Structure Systems with Application to Economics and Biology*, pp. 54–63, Springer, 1975.

[14] Z. Aganovic and Z. Gajic, "Successive approximation procedure for steady-state optimal control of bilinear systems," *Journal of Optimization Theory and Applications*, vol. 84, pp. 273–291, Feb. 1995.

[15] W. A. Cebuhar and V. Costanza, "Approximation procedures for the optimal control of bilinear and nonlinear systems," *Journal of Optimization Theory and Applications*, vol. 43, pp. 615–627, Aug. 1984.

[16] J.-S. Li and N. Khaneja, "Control of inhomogeneous quantum ensembles," *Physical review A*, vol. 73, no. 3, p. 030302, 2006.

[17] E. P. Hofer and B. Tibken, "An iterative method for the finite-time bilinear-quadratic control problem," *Journal of Optimization Theory and Applications*, vol. 57, no. 3, pp. 411–427, 1988.

[18] S. P. Banks and K. Dinesh, "Approximate optimal control and stability of nonlinear finite- and infinite-dimensional systems," *Annals of Operations Research*, vol. 98, pp. 19–44, 2000.

[19] T. Çimen and S. P. Banks, "Global optimal feedback control for general nonlinear systems with nonquadratic performance criterea," *Systems and Control Letters*, vol. 53, pp. 327–346, 2004.

[20] Z. Aganovic and Z. Gajic, "The successive approximation procedure for finite-time optimal control of bilinear systems," *IEEE Transactions on Automatic Control*, vol. 39, pp. 1932–1935, Sep. 1994.

[21] A. Wernli and G. Cook, "Suboptimal control for the nonlinear quadratic regulator problem," *Automatica*, vol. 11, pp. 75–84, 1975.

[22] W. L. Garrard, "Suboptimal feedback control for nonlinear systems," *Automatica*, vol. 8, pp. 219–221, 1972.

[23] T. Çimen and S. P. Banks, "Nonlinear optimal tracking control with application to supertankers for autopilot design," *Automatica*, vol. 40, pp. 1845–1863, 2004.

[24] J.-S. Li and N. Khaneja, "Ensemble control of bloch equations," *IEEE Transactions on Automatic Control*, vol. 54, no. 3, pp. 528–536, 2009.

[25] J. Ruths, *Optimal Control of Inhomogeneous Ensembles*. PhD thesis, Washington University in St. Louis, 2011.

[26] J.-M. Coron, *Control and nonlinearity*. No. 136, American Mathematical Soc., 2007.

[27] R. W. Brockett, "Nonlinear systems and differential geometry," *Proceedings of the IEEE*, vol. 64, no. 1, pp. 61–72, 1976.

[28] F. Dörfler and F. Bullo, "Synchronization and transient stability in power networks and nonuniform kuramoto oscillators," *SIAM Journal on Control and Optimization*, vol. 50, no. 3, pp. 1616–1642, 2012.

[29] F. Dörfler, M. Chertkov, and F. Bullo, "Synchronization in complex oscillator networks and smart grids," *Proceedings of the National Academy of Sciences*, vol. 110, no. 6, pp. 2005–2010, 2013.

[30] L. Alberto and N. Bretas, "Synchronism versus stability in power systems: Frequency dependent loads," in *Power System Technology, 1998. Proceedings. POWERCON'98. 1998 International Conference on*, vol. 2, pp. 1341–1345, IEEE, 1998.

[31] M. Bier, B. M. Bakker, and H. V. Westerhoff, "How yeast cells synchronize their glycolytic oscillations: a perturbation analytic treatment," *Biophysical Journal*, vol. 78, no. 3, pp. 1087–1093, 2000.

[32] P. Richard, B. M. Bakker, B. Teusink, K. Van Dam, and H. V. Westerhoff, "Acetaldehyde mediates the synchronization of sustained glycolytic oscillations in populations of yeast cells," *European journal of biochemistry*, vol. 235, no. 1-2, pp. 238–241, 1996.

[33] V. Lakshmanan, M. Marinelli, A. M. Kosek, P. B. Nørgård, and H. W. Bindner, "Impact of thermostatically controlled loads' demand response activation on aggregated power: A field experiment," *Energy*, vol. 94, no. Supplement C, pp. 705 – 714, 2016.

[34] A. Malik and J. Ravishankar, "A hybrid control approach for regulating frequency through demand response," *Applied Energy*, 2017.

[35] W. Bomela, A. Zlotnik, and J.-S. Li, "A phase model approach for thermostatically controlled load demand response," *Applied Energy*, vol. 228, pp. 667 – 680, 2018.

[36] P. Hines, K. Balasubramaniam, and E. C. Sanchez, "Cascading failures in power grids," *IEEE Potentials*, vol. 28, no. 5, 2009.

[37] P. Crucitti, V. Latora, and M. Marchiori, "Model for cascading failures in complex networks," *Physical Review E*, vol. 69, no. 4, p. 045104, 2004.

[38] L. B. Good, S. Sabesan, S. T. Marsh, K. Tsakalis, D. Treiman, and L. Iasemidis, "Control of synchronization of brain dynamics leads to control of epileptic seizures in rodents," *International journal of neural systems*, vol. 19, no. 03, pp. 173–196, 2009.

[39] B. J. Gluckman, H. Nguyen, S. L. Weinstein, and S. J. Schiff, "Adaptive electric field control of epileptic seizures," *Journal of Neuroscience*, vol. 21, no. 2, pp. 590–600, 2001.

[40] E. M. Izhikevich, "Polychronization: computation with spikes," *Neural computation*, vol. 18, no. 2, pp. 245–282, 2006.

[41] P. A. Tass, "A model of desynchronizing deep brain stimulation with a demand-controlled coordinated reset of neural subpopulations," *Biological cybernetics*, vol. 89, no. 2, pp. 81–88, 2003.

[42] C. Hauptmann, O. Popovych, and P. A. Tass, "Effectively desynchronizing deep brain stimulation based on a coordinated delayed feedback stimulation via several sites: a computational study," *Biological cybernetics*, vol. 93, no. 6, pp. 463–470, 2005.

[43] P. J. Uhlhaas and W. Singer, "Neural synchrony in brain disorders: relevance for cognitive dysfunctions and pathophysiology," *Neuron*, vol. 52, no. 1, pp. 155–168, 2006.

[44] F. E. Hanson, "Comparative studies of firefly pacemakers.," in *Federation proceedings*, vol. 37, pp. 2158–2164, 1978.

[45] R. E. Mirollo and S. H. Strogatz, "Synchronization of pulse-coupled biological oscillators," *SIAM Journal on Applied Mathematics*, vol. 50, no. 6, pp. 1645–1662, 1990.

[46] I. Fischer, Y. Liu, and P. Davis, "Synchronization of chaotic semiconductor laser dynamics on subnanosecond time scales and its potential for chaos communication," *Physical Review A*, vol. 62, no. 1, p. 011801, 2000.

[47] D.-B. S. for Parkinson's Disease Study Group *et al.*, "Deep-brain stimulation of the subthalamic nucleus or the pars interna of the globus pallidus in parkinson's disease," *N Engl J Med*, vol. 2001, no. 345, pp. 956–963, 2001.

[48] M. J. Schaus and J. Moehlis, "On the response of neurons to sinusoidal current stimuli: phase response curves and phase-locking," in *Decision and Control, 2006 45th IEEE Conference on*, pp. 2376–2381, IEEE, 2006.

[49] J.-S. Li, "Control of a network of spiking neurons," *IFAC Proceedings Volumes*, vol. 43, no. 14, pp. 314–319, 2010.

[50] L. Glass, "Cardiac arrhythmias and circle maps- a classical problem," *Chaos: An Interdisciplinary Journal of Nonlinear Science*, vol. 1, no. 1, pp. 13–19, 1991.

[51] A. T. Winfree, *The geometry of biological time*, vol. 12. Springer Science & Business Media, 2001.

[52] W. Gerstner, R. Ritz, and J. L. Van Hemmen, "Why spikes? hebbian learning and retrieval of time-resolved excitation patterns," *Biological cybernetics*, vol. 69, no. 5-6, pp. 503–515, 1993.

[53] J. V. Arthur and K. Boahen, "Learning in silicon: Timing is everything," in *Advances in neural information processing systems*, pp. 75–82, 2006.

[54] M. Mehta, A. Lee, and M. Wilson, "Role of experience and oscillations in transforming a rate code into a temporal code," *Nature*, vol. 417, no. 6890, p. 741, 2002.

[55] P. A. Merolla, J. V. Arthur, R. Alvarez-Icaza, A. S. Cassidy, J. Sawada, F. Akopyan, B. L. Jackson, N. Imam, C. Guo, Y. Nakamura, *et al.*, "A million spiking-neuron integrated circuit with a scalable communication network and interface," *Science*, vol. 345, no. 6197, pp. 668–673, 2014.

[56] M. Davies, N. Srinivasa, T.-H. Lin, G. Chinya, Y. Cao, S. H. Choday, G. Dimou, P. Joshi, N. Imam, S. Jain, *et al.*, "Loihi: A neuromorphic manycore processor with on-chip learning," *IEEE Micro*, vol. 38, no. 1, pp. 82–99, 2018.

[57] J.-s. Seo, B. Brezzo, Y. Liu, B. D. Parker, S. K. Esser, R. K. Montoye, B. Rajendran, J. A. Tierno, L. Chang, D. S. Modha, *et al.*, "A 45nm cmos neuromorphic chip with a scalable architecture for learning in networks of spiking neurons," in *Custom Integrated Circuits Conference (CICC), 2011 IEEE*, pp. 1–4, IEEE, 2011.

[58] E. Zrenner, "Will retinal implants restore vision?," *Science*, vol. 295, no. 5557, pp. 1022–1025, 2002.

[59] K. A. Zaghloul and K. Boahen, "Optic nerve signals in a neuromorphic chip i: Outer and inner retina models," *IEEE Transactions on Biomedical Engineering*, vol. 51, no. 4, pp. 657–666, 2004.

[60] K. A. Zaghloul and K. Boahen, "Optic nerve signals in a neuromorphic chip ii: Testing and results," *IEEE Transactions on Biomedical Engineering*, vol. 51, no. 4, pp. 667–675, 2004.

[61] I. S. Dasanayake and J.-S. Li, "Constrained charge-balanced minimum-power controls for spiking neuron oscillators," *Systems & Control Letters*, vol. 75, pp. 124–130, 2015.

[62] A. Nabi and J. Moehlis, "Charge-balanced optimal inputs for phase models of spiking neurons," in *ASME 2009 Dynamic Systems and Control Conference*, pp. 685–687, American Society of Mechanical Engineers, 2009.

[63] A. Zlotnik and J.-S. Li, "Optimal asymptotic entrainment of phase-reduced oscillators," in *ASME 2011 Dynamic Systems and Control Conference and Bath/ASME Symposium on Fluid Power and Motion Control*, pp. 479–484, American Society of Mechanical Engineers, 2011.

[64] A. Zlotnik and J.-S. Li, "Optimal entrainment of neural oscillator ensembles," *Journal of Neural Engineering*, vol. 9, p. 046015, Aug 2012.

[65] H.-A. Tanaka, "Optimal entrainment with smooth, pulse, and square signals in weakly forced nonlinear oscillators," *Physica D: Nonlinear Phenomena*, vol. 288, pp. 1–22, 2014.

[66] T. Harada, H.-A. Tanaka, M. J. Hankins, and I. Z. Kiss, "Optimal waveform for the entrainment of a weakly forced oscillator," *Physical review letters*, vol. 105, no. 8, p. 088301, 2010.

[67] A. Zlotnik, R. Nagao, I. Z. Kiss, and J.-s. Li, "Phase-selective entrainment of nonlinear oscillator ensembles," *Nature Communications*, vol. 7, p. 10788, 2016.

[68] A. Nabi and J. Moehlis, "Single input optimal control for globally coupled neuron networks," *Journal of neural engineering*, vol. 8, no. 6, p. 065008, 2011.

[69] A. Nandi, H. Schättler, and S. Ching, "Selective spiking in neuronal populations," in *American Control Conference (ACC), 2017*, pp. 2811–2816, IEEE, 2017.

[70] Y. Zhai, I. Z. Kiss, and J. L. Hudson, "Control of complex dynamics with time-delayed feedback in populations of chemical oscillators: Desynchronization and clustering," *Industrial & Engineering Chemistry Research*, vol. 47, no. 10, pp. 3502–3514, 2008.

[71] I. Z. Kiss, C. G. Rusin, H. Kori, and J. L. Hudson, "Engineering complex dynamical structures: sequential patterns and desynchronization," *Science*, vol. 316, no. 5833, pp. 1886–1889, 2007.

[72] E. C. Kara, M. D. Tabone, J. S. MacDonald, D. S. Callaway, and S. Kiliccote, "Quantifying flexibility of residential thermostatically controlled loads for demand response: a data-driven approach," in *Proceedings of the 1st ACM Conference on Embedded Systems for Energy-Efficient Buildings*, pp. 140–147, ACM, 2014.

[73] J. Yan, Y. Zhai, P. Wijayatunga, A. M. Mohamed, and P. E. Campana, "Renewable energy integration with mini/micro-grids," *Applied Energy*, vol. 201, no. Supplement C, pp. 241 – 244, 2017.

[74] E. C. Kara, M. Bergés, and G. Hug, "Impact of disturbances on modeling of thermostatically controlled loads for demand response," *IEEE Transactions on Smart Grid*, vol. 6, pp. 2560–2568, Sept 2015.

[75] S. P. Meyn, P. Barooah, A. Bušić, Y. Chen, and J. Ehren, "Ancillary service to the grid using intelligent deferrable loads," *IEEE Transactions on Automatic Control*, vol. 60, pp. 2847–2862, Nov 2015.

[76] S. Behboodi, D. P. Chassin, N. Djilali, and C. Crawford, "Transactive control of fast-acting demand response based on thermostatic loads in real-time retail electricity markets," *Applied Energy*, 2017.

[77] C. Sijie and L. Chen-Ching, "From demand response to transactive energy: state of the art," *Journal of Modern Power Systems and Clean Energy*, vol. 5, pp. 10–19, Jan 2017.

[78] Y. Zhou, C. Wang, J. Wu, J. Wang, M. Cheng, and G. Li, "Optimal scheduling of aggregated thermostatically controlled loads with renewable generation in the intraday electricity market," *Applied Energy*, vol. 188, no. Supplement C, pp. 456 – 465, 2017.

[79] A. Ghaffari, S. Moura, and M. Krstić, "Modeling, control, and stability analysis of heterogeneous thermostatically controlled load populations using partial differential equations," *Journal of Dynamic Systems, Measurement, and Control*, vol. 137, pp. 1213–1219, Aug 2015.

[80] V. Lakshmanan, M. Marinelli, J. Hu, and H. W. Bindner, "Provision of secondary frequency control via demand response activation on thermostatically controlled loads: Solutions and experiences from denmark," *Applied Energy*, vol. 173, no. Supplement C, pp. 470 – 480, 2016.

[81] D. Docimo and H. K. Fathy, "Demand response using heterogeneous thermostatically controlled loads: Characterization of aggregate power dynamics," *Journal of Dynamic Systems, Measurement, and Control*, vol. 139, no. 10, p. 101009, 2017.

[82] M. Chertkov and V. Chernyak, "Ensemble of thermostatically controlled loads: Statistical physics approach," *arXiv preprint arXiv:1701.04939*, 2017.

[83] A. Zlotnik and J.-S. Li, "Optimal subharmonic entrainment of weakly forced nonlinear oscillators," *SIAM Journal on Applied Dynamical Systems*, vol. 13, no. 4, pp. 1654–1693, 2014.

[84] E. M. Izhikevich, *Dynamical systems in neuroscience*. MIT press, 2007.

[85] K. Ma, C. Yuan, J. Yang, Z. Liu, and X. Guan, "Switched control strategies of aggregated commercial hvac systems for demand response in smart grids," *Energies*, vol. 10, no. 7, p. 953, 2017.

[86] B. Baeten, F. Rogiers, and L. Helsen, "Reduction of heat pump induced peak electricity use and required generation capacity through thermal energy storage and demand response," *Applied Energy*, vol. 195, no. Supplement C, pp. 184 – 195, 2017.

[87] D. S. Callaway, "Tapping the energy storage potential in electric loads to deliver load following and regulation, with application to wind energy," *Energy Conversion and Management*, vol. 50, no. 5, pp. 1389 – 1400, 2009.

[88] N. A. Sinitsyn, S. Kundu, and S. Backhaus, "Safe protocols for generating power pulses with heterogeneous populations of thermostatically controlled loads," *Energy Conversion and Management*, vol. 67, pp. 297–308, 2013.

[89] N. Mehta, N. A. Sinitsyn, S. Backhaus, and B. C. Lesieutre, "Safe control of thermostatically controlled loads with installed timers for demand side management," *Energy Conversion and Management*, vol. 86, pp. 784–791, 2014.

[90] S. Ching, E. N. Brown, and M. A. Kramer, "Distributed control in a mean-field cortical network model: implications for seizure suppression," *Physical Review E*, vol. 86, no. 2, p. 021920, 2012.

[91] R. Mikkelsen, M. Andreasen, and S. Nedergaard, "Suppression of epileptiform activity by a single short-duration electric field in rat hippocampus in vitro," *Journal of neurophysiology*, vol. 109, no. 11, pp. 2720–2731, 2013.

[92] E. F. Du Toit and I. K. Craig, "Selective pinning control of the average disease transmissibility in an hiv contact network," *Physical Review E*, vol. 92, no. 1, p. 012810, 2015.

[93] A. Rahmani, M. Ji, M. Mesbahi, and M. Egerstedt, "Controllability of multi-agent systems from a graph-theoretic perspective," *SIAM Journal on Control and Optimization*, vol. 48, no. 1, pp. 162–186, 2009.

[94] C. W. Wu, "On the relationship between pinning control effectiveness and graph topology in complex networks of dynamical systems," *Chaos: An Interdisciplinary Journal of Nonlinear Science*, vol. 18, no. 3, p. 037103, 2008.

[95] X. Li, X. Wang, and G. Chen, "Pinning a complex dynamical network to its equilibrium," *IEEE Transactions on Circuits and Systems I: Regular Papers*, vol. 51, no. 10, pp. 2074–2087, 2004.

[96] X. Wang and H. Su, "Pinning control of complex networked systems: A decade after and beyond," *Annual Reviews in Control*, vol. 38, no. 1, pp. 103–111, 2014.

[97] M. Egerstedt, S. Martini, M. Cao, K. Camlibel, and A. Bicchi, "Interacting with networks: How does structure relate to controllability in single-leader, consensus networks?," *IEEE Control Systems*, vol. 32, no. 4, pp. 66–73, 2012.

[98] R. Olfati-Saber, J. A. Fax, and R. M. Murray, "Consensus and cooperation in networked multi-agent systems," *Proceedings of the IEEE*, vol. 95, no. 1, pp. 215–233, 2007.

[99] N. Khaneja, B. Luy, and S. J. Glaser, "Boundary of quantum evolution under decoherence," *Proceedings of the National Academy of Sciences*, vol. 100, no. 23, pp. 13162–13166, 2003.

[100] N. Khaneja, T. Reiss, B. Luy, and S. J. Glaser, "Optimal control of spin dynamics in the presence of relaxation," *Journal of Magnetic Resonance*, vol. 162, no. 2, pp. 311–319, 2003.

[101] D. Stefanatos, S. J. Glaser, and N. Khaneja, "Relaxation-optimized transfer of spin order in ising spin chains," *Physical Review A*, vol. 72, no. 6, p. 062320, 2005.

[102] J. Ruths and J.-S. Li, "Optimal control of inhomogeneous ensembles," *IEEE Transactions on Automatic Control*, vol. 57, no. 8, pp. 2021–2032, 2012.

[103] W. Bomela and J. S. Li, "An iterative method for computing optimal controls for bilinear quadratic tracking problems," in *2016 American Control Conference (ACC)*, pp. 2912–2917, July 2016.

[104] S. Wang and J.-S. Li, "Free-endpoint optimal control of inhomogeneous bilinear ensemble systems," *Automatica*, vol. 95, pp. 306–315, 2018.

[105] M. Athans and P. L. Falb, *Optimal Control: An introduction to the Theory and Its Applications*. New York: McGraw-Hill Book Company, 1966.

[106] H. Schättler and U. Ledzewicz, *Geometric optimal control: theory, methods and examples*, vol. 38. Springer Science & Business Media, 2012.

[107] R. E. Kalman, "Contributions to the theory of optimal control," *Boletin de la Sociedad Matematica Mexicana*, vol. 5, pp. 102–119, 1960.

[108] D. H. Jacobson, "New conditions for boundeness of the solution of a matrix riccati differential equation," *Journal of Differential Equations*, vol. 8, pp. 258–263, 1970.

[109] W. M. Getz and D. H. Jacobson, "Sufficient conditions for finite escape times in systems of quadratic differential equations," *Journal of the Instute of Mathematics and its Applications*, vol. 19, pp. 377–383, 1977.

[110] D. H. Jacobson, *Extensions of Linear-Quadratic Control, Optimization and Matrix Theory*. New York: Academic Press, 1977.

[111] D. T. Stansbery and J. R. Cloutier, "Position and attitude control of a spacecraft using the state-dependent riccati equation technique," in *Proceedings of the American Control Conference*, (Chicago), pp. 1867–1871, Jun. 2000.

[112] B. C. Chachuat, *Nonlinear and Dynamic Optimization: From Theory to Practice - IC-32: Winter Semester 2006/2007*. Polycopiés de l'EPFL, Switzerland: EPFL, 2007.

[113] D. Stefanatos, *Optimal Control of Coupled Spin Dynamics in the Presence of Relaxation*. Harvard University, 2005.

[114] M. Goldman, *Quantum description of high-resolution NMR in liquids*, vol. 15. Oxford University Press, USA, 1988.

[115] G. A. Morris and R. Freeman, "Enhancement of nuclear magnetic resonance signals by polarization transfer," *Journal of the American Chemical Society*, vol. 101, no. 3, pp. 760–762, 1979.

[116] M. Silver, R. Joseph, and D. Hoult, "Selective spin inversion in nuclear magnetic resonance and coherent optics through an exact solution of the bloch-riccati equation," *Physical Review A*, vol. 31, no. 4, p. 2753, 1985.

[117] J. Pauly, P. Le Roux, D. Nishimura, and A. Macovski, "Parameter relations for the shinnar-le roux selective excitation pulse design algorithm (nmr imaging)," *IEEE transactions on medical imaging*, vol. 10, no. 1, pp. 53–65, 1991.

[118] A. L. Hodgkin and A. F. Huxley, "A quantitative description of membrane current and its application to conduction and excitation in nerve," *The Journal of physiology*, vol. 117, no. 4, pp. 500–544, 1952.

[119] A. T. Winfree, "Biological rhythms and the behavior of populations of coupled oscillators," *Journal of theoretical biology*, vol. 16, no. 1, pp. 15–42, 1967.

[120] A. Zlotnik, Y. Chen, I. Z. Kiss, H.-A. Tanaka, and J.-S. Li, "Optimal waveform for fast entrainment of weakly forced nonlinear oscillators," *Physical review letters*, vol. 111, no. 2, p. 024102, 2013.

[121] D. Efimov, P. Sacré, and R. Sepulchre, "Controlling the phase of an oscillator: A phase response curve approach," in *Decision and Control, 2009 held jointly with the 2009 28th Chinese Control Conference. CDC/CCC 2009. Proceedings of the 48th IEEE Conference on*, pp. 7692–7697, Dec 2009.

[122] Y. Kuramoto, *Chemical oscillations, waves, and turbulence*, vol. 19. Springer Science & Business Media, 2012.

[123] E. Brown, J. Moehlis, and P. Holmes, "On the phase reduction and response dynamics of neural oscillator populations," *Neural computation*, vol. 16, no. 4, pp. 673–715, 2004.

[124] D. Efimov, "Phase resetting for a network of oscillators via phase response curve approach," *Biological cybernetics*, vol. 109, no. 1, pp. 95–108, 2015.

[125] B. Ermentrout, "Type 1 menbranes, phase resetting curves, and synchrony," *Neural Computation*, vol. 8, pp. 979–1001, Aug 1996.

[126] H. Nakao, T. Yanagita, and Y. Kawamura, "Phase-reduction approach to synchronization of spatiotemporal rhythms in reaction-diffusion systems," *Physical review X*, vol. 4, no. 2, p. 021032, 2014.

[127] M. A. Schwemmer and T. J. Lewis, "The theory of weakly coupled oscillators," in *Phase response curves in neuroscience*, pp. 3–31, Springer, 2012.

[128] H. Nakao, "Phase reduction approach to synchronization of nonlinear oscillators," *Contemporary Physics*, vol. 57, no. 2, pp. 188–214, 2016.

[129] J.-S. Li, I. Dasanayake, and J. Ruths, "Control and synchronization of neuron ensembles," *IEEE Transactions on Automatic Control*, vol. 58, no. 8, pp. 1919–1930, 2013.

[130] A. Isidori, *Nonlinear control systems*. Springer Science & Business Media, 2013.

[131] I. S. Dasanayake and J.-S. Li, "Design of charge-balanced time-optimal stimuli for spiking neuron oscillators," *Neural computation*, 2014.

[132] M. Rabinovich, A. Volkovskii, P. Lecanda, R. Huerta, H. D. I. Abarbanel, and G. Laurent, "Dynamical encoding by networks of competing neuron groups: Winnerless competition," *Phys. Rev. Lett.*, vol. 87, p. 068102, Jul 2001.

[133] W. Sun and D. L. Barbour, "Rate, not selectivity, determines neuronal population coding accuracy in auditory cortex," *PLoS biology*, vol. 15, no. 11, p. e2002459, 2017.

[134] G. Laurent, "Olfactory network dynamics and the coding of multidimensional signals," *Nature reviews neuroscience*, vol. 3, no. 11, p. 884, 2002.

[135] S. A. Shamma, "Speech processing in the auditory system i: The representation of speech sounds in the responses of the auditory nerve," *The Journal of the Acoustical Society of America*, vol. 78, no. 5, pp. 1612–1621, 1985.

[136] P. Ashwin and M. Timme, "Nonlinear dynamics: when instability makes sense," *Nature*, vol. 436, no. 7047, p. 36, 2005.

[137] G. B. Stanley, "Reading and writing the neural code," *Nature neuroscience*, vol. 16, no. 3, p. 259, 2013.

[138] T. Tuma, A. Pantazi, M. Le Gallo, A. Sebastian, and E. Eleftheriou, "Stochastic phase-change neurons," *Nature nanotechnology*, vol. 11, no. 8, p. 693, 2016.

[139] A. T. Sornborger, Z. Wang, and L. Tao, "A mechanism for graded, dynamically routable current propagation in pulse-gated synfire chains and implications for information coding," *Journal of computational neuroscience*, vol. 39, no. 2, pp. 181–195, 2015.

[140] Z. Wang, A. T. Sornborger, and L. Tao, "Graded, dynamically routable information processing with synfire-gated synfire chains," *PLoS computational biology*, vol. 12, no. 6, p. e1004979, 2016.

[141] T. Pfeil, J. Jordan, T. Tetzlaff, A. Grübl, J. Schemmel, M. Diesmann, and K. Meier, "Effect of heterogeneity on decorrelation mechanisms in spiking neural networks: A neuromorphic-hardware study," *Physical Review X*, vol. 6, no. 2, p. 021023, 2016.

[142] F. C. Hoppensteadt and E. M. Izhikevich, "Oscillatory neurocomputers with dynamic connectivity," *Physical Review Letters*, vol. 82, no. 14, p. 2983, 1999.

[143] F. C. Hoppensteadt and E. M. Izhikevich, "Synchronization of laser oscillators, associative memory, and optical neurocomputing," *Physical Review E*, vol. 62, no. 3, p. 4010, 2000.

[144] J. Moehlis, E. Shea-Brown, and H. Rabitz, "Optimal inputs for phase models of spiking neurons," *Journal of computational and nonlinear dynamics*, vol. 1, no. 4, pp. 358–367, 2006.

[145] V. Jurdjevic, *Geometric control theory*, vol. 52. Cambridge university press, 1997.

[146] S. Ihara and F. C. Schweppe, "Physically based modeling of cold load pickup," *IEEE Transactions on Power Apparatus and Systems*, vol. PAS-100, pp. 4142–4150, Sept 1981.

[147] C. Perfumo, E. Kofman, J. H. Braslavsky, and J. K. Ward, "Load management: Model-based control of aggregate power for populations of thermostatically controlled loads," *Energy Conversion and Management*, vol. 55, pp. 36 – 48, 2012.

[148] S. Bashash and H. K. Fathy, "Modeling and control insights into demand-side energy management through setpoint control of thermostatic loads," in *Proceedings of the 2011 American Control Conference*, pp. 4546–4553, June 2011.

[149] S. Kundu, N. Sinitsyn, S. Backhaus, and I. Hiskens, "Modeling and control of thermostatically controlled loads," *arXiv preprint arXiv:1101.2157*, 2011.

[150] B. Ermentrout, *Simulating, analyzing, and animating dynamical systems: a guide to XPPAUT for researchers and students*. SIAM, 2002.

[151] D. S. Callaway and I. A. Hiskens, "Achieving controllability of electric loads," *Proceedings of the IEEE*, vol. 99, pp. 184–199, Jan 2011.

[152] W. B. Bomela, I. Dasanayake, J.-S. Li, Y. Chen, and I. Z. Kiss, "Optimal phase-to-phase control of chemical oscillations through phase models," *Industrial & Engineering Chemistry Research*, 2018.

[153] I. Dasanayake and J.-S. Li, "Optimal design of minimum-power stimuli for phase models of neuron oscillators," *Physical Review E*, vol. 83, no. 6, p. 061916, 2011.

[154] W. Zhang, J. Lian, C.-Y. Chang, and K. Kalsi, "Aggregated modeling and control of air conditioning loads for demand response," *IEEE transactions on power systems*, vol. 28, no. 4, pp. 4655–4664, 2013.

[155] Bonneville Power Administration, "BPA Area Control Error (ACE) Annual Reports, Per FERC Order 784." [Online]. Available from: `https://transmission.bpa.gov/Business/Operations/ACE_FERC784/`, 2017.

[156] S. Shirasaka, W. Kurebayashi, and H. Nakao, "Phase reduction theory for hybrid nonlinear oscillators," *Physical Review E*, vol. 95, no. 1, p. 012212, 2017.

[157] A. Granada, R. Hennig, B. Ronacher, A. Kramer, and H. Herzel, "Phase response curves: elucidating the dynamics of coupled oscillators," *Methods in enzymology*, vol. 454, pp. 1–27, 2009.

[158] H.-A. Tanaka, I. Nishikawa, J. Kurths, Y. Chen, and I. Z. Kiss, "Optimal synchronization of oscillatory chemical reactions with complex pulse, square, and smooth waveforms signals maximizes tsallis entropy," *EPL (Europhysics Letters)*, vol. 111, no. 5, p. 50007, 2015.

[159] P. Barooah, A. Bušić, and S. Meyn, "Spectral decomposition of demand-side flexibility for reliable ancillary services in a smart grid," in *System Sciences (HICSS), 2015 48th Hawaii International Conference on*, pp. 2700–2709, IEEE, 2015.

[160] J. L. M. Stephan Koch and D. S. Callaway, "Modeling and control of aggregated heterogeneous thermostatically controlled loads for ancillary services," *17th Power System Computation Conference*, 2011.

[161] E. Vrettos, S. Koch, and G. Andersson, "Load frequency control by aggregations of thermally stratified electric water heaters," in *Innovative Smart Grid Technologies (ISGT Europe), 2012 3rd IEEE PES International Conference and Exhibition on*, pp. 1–8, IEEE, 2012.

[162] R. M. Delgado, "Demand-side management alternatives," *Proceedings of the IEEE*, vol. 73, pp. 1471–1488, Oct 1985.

[163] L. S. Pontryagin, *Mathematical theory of optimal processes*. Routledge, 2018.

[164] D. Stefanatos and J.-S. Li, "Constrained minimum-energy optimal control of the dissipative bloch equations," *Systems & Control Letters*, vol. 59, no. 10, pp. 601–607, 2010.

[165] I. Dasanayake and S. Li Jr, "Charge-balanced minimum-power controls for spiking neuron oscillators," *arXiv preprint arXiv:1109.3798*, 2011.

[166] W. Zhang, K. Kalsi, J. Fuller, M. Elizondo, and D. Chassin, "Aggregate model for heterogeneous thermostatically controlled loads with demand response," in *2012 IEEE Power and Energy Society General Meeting*, pp. 1–8, July 2012.

[167] T. Chen, X. Liu, and W. Lu, "Pinning complex networks by a single controller," *IEEE Transactions on Circuits and Systems I: Regular Papers*, vol. 54, no. 6, pp. 1317–1326, 2007.

[168] X. F. Wang and G. Chen, "Pinning control of scale-free dynamical networks," *Physica A: Statistical Mechanics and its Applications*, vol. 310, no. 3-4, pp. 521–531, 2002.

[169] S. Ma, Q. Lu, and S. J. Hogan, "Double hopf bifurcation for stuart–landau system with nonlinear delay feedback and delay-dependent parameters," *Advances in Complex Systems*, vol. 10, no. 04, pp. 423–448, 2007.

[170] R. Dodla, A. Sen, and G. L. Johnston, "Phase-locked patterns and amplitude death in a ring of delay-coupled limit cycle oscillators," *Physical Review E*, vol. 69, no. 5, p. 056217, 2004.

[171] S. Uchiyama, "Flow version of statistical neurodynamics for oscillator neural networks," *Physica A: Statistical Mechanics and its Applications*, vol. 391, no. 8, pp. 2807–2817, 2012.

[172] R. Karnatak, R. Ramaswamy, and A. Prasad, "Amplitude death in the absence of time delays in identical coupled oscillators," *Physical Review E*, vol. 76, no. 3, p. 035201, 2007.

[173] H. Bi, X. Hu, X. Zhang, Y. Zou, Z. Liu, and S. Guan, "Explosive oscillation death in coupled stuart-landau oscillators," *EPL (Europhysics Letters)*, vol. 108, no. 5, p. 50003, 2014.

[174] M. Wickramasinghe and I. Z. Kiss, "Spatially organized dynamical states in chemical oscillator networks: Synchronization, dynamical differentiation, and chimera patterns," *PloS one*, vol. 8, no. 11, p. e80586, 2013.

[175] R. A. Hom and C. R. Johnson, "Topics in matrix analysis," *Cambridge UP, New York*, 1991.

[176] W. chyuan Yueh, "Eigenvalues of several tridiagonal matrices," in *Applied Mathematics E-notes*, pp. 5–66, 2005.

[177] R. B. Bapat, *Graphs and Matrices*. Springer, 2010.

[178] E. W. Weisstein, *CRC concise encyclopedia of mathematics*. CRC press, 2002.

[179] E. Hartmann, "Planar circle geometries: an introduction to moebius-, laguerre-and minkowski-planes," p. 93.

[180] Y. Orouskhani, M. Jalili, and X. Yu, "Optimizing dynamical network structure for pinning control," *Scientific reports*, vol. 6, p. 24252, 2016.

[181] W. L. Brogan, *Modern control theory*. Prentice Hall, NJ, 1991.

[182] A. Hamdan and A. Elabdalla, "Geometric measures of modal controllability and observability of power system models," *Electric Power Systems Research*, vol. 15, no. 2, pp. 147–155, 1988.

[183] B. Porter and R. Crossley, *Modal Control: Theory and applications*. Taylor & Francis Group, 1972.

[184] H. K. Khalil, *Nonlinear systems*. Prentice Hall, 2002.

[185] M. Tarokh, "Measures for controllability, observability and fixed modes," *IEEE Transactions on Automatic Control*, vol. 37, no. 8, pp. 1268–1273, 1992.

[186] Y.-Y. Liu, J.-J. Slotine, and A.-L. Barabási, "Control centrality and hierarchical structure in complex networks," *Plos one*, vol. 7, no. 9, p. e44459, 2012.

[187] R. Albert and A.-L. Barabási, "Statistical mechanics of complex networks," *Reviews of modern physics*, vol. 74, no. 1, p. 47, 2002.

[188] A.-L. Barabási and R. Albert, "Emergence of scaling in random networks," *science*, vol. 286, no. 5439, pp. 509–512, 1999.

[189] P. Erdös and A. Rényi, "On the evolution of random graphs," *Publ. Math. Inst. Hung. Acad. Sci*, vol. 5, no. 17-61, p. 43, 1960.

[190] D. J. Watts and S. H. Strogatz, "Collective dynamics of 'small-world' networks," *nature*, vol. 393, no. 6684, p. 440, 1998.

[191] J. J. Molitierno, *Applications of combinatorial matrix theory to Laplacian matrices of graphs*. Chapman and Hall/CRC, 2016.

[192] KONECT, "Facebook (nips) network dataset." [Online]. Available from: `http://konect.uni-koblenz.de/networks/ego-facebook`, April 2017.

[193] J. Kunegis, "Konect: The koblenz network collection," in *Proceedings of the 22Nd International Conference on World Wide Web*, WWW '13 Companion, (New York, NY, USA), pp. 1343–1350, ACM, 2013.

[194] P. Ashwin and J. W. Swift, "The dynamics of n weakly coupled identical oscillators," *Journal of Nonlinear Science*, vol. 2, no. 1, pp. 69–108, 1992.

[195] S. J. Schiff, K. Jerger, D. H. Duong, T. Chang, M. L. Spano, W. L. Ditto, *et al.*, "Controlling chaos in the brain," *Nature*, vol. 370, no. 6491, pp. 615–620, 1994.

[196] F. C. Hoppensteadt and E. M. Izhikevich, "Synchronization of mems resonators and mechanical neurocomputing," *IEEE Transactions on Circuits and Systems I: Fundamental Theory and Applications*, vol. 48, no. 2, pp. 133–138, 2001.

[197] M. Kitsak, L. K. Gallos, S. Havlin, F. Liljeros, L. Muchnik, H. E. Stanley, and H. A. Makse, "Identification of influential spreaders in complex networks," *Nature physics*, vol. 6, no. 11, p. 888, 2010.

[198] L. Hébert-Dufresne, A. Allard, J.-G. Young, and L. J. Dubé, "Global efficiency of local immunization on complex networks," *Scientific reports*, vol. 3, p. 2171, 2013.

[199] A. Dekker, B. Phelps, B. Dijkman, T. van Der Nagel, F. van Der Veen, G. Geskes, and J. Maessen, "Epicardial left ventricular lead placement for cardiac resynchronization therapy: optimal pace site selection with pressure-volume loops," *The Journal of thoracic and cardiovascular surgery*, vol. 127, no. 6, pp. 1641–1647, 2004.

[200] J. P. Sun, E. Chinchoy, E. Donal, Z. B. Popović, G. Perlic, C. R. Asher, N. L. Greenberg, R. A. Grimm, B. L. Wilkoff, and J. D. Thomas, "Evaluation of ventricular synchrony using novel doppler echocardiographic indices in patients with heart failure receiving cardiac resynchronization therapy," *Journal of the American Society of Echocardiography*, vol. 17, no. 8, pp. 845–850, 2004.

[201] D. Postnov, D. Postnov, D. Marsh, N.-H. Holstein-Rathlou, and O. Sosnovtseva, "Dynamics of nephron-vascular network," *Bulletin of mathematical biology*, vol. 74, no. 12, pp. 2820–2841, 2012.

[202] M. Athans, "The status of optimal control theory and applications for deterministic systems," *IEEE Transactions on Automatic Control*, vol. 11, no. 3, pp. 580–596, 1966.

[203] C. Morris and H. Lecar, "Voltage oscillations in the barnacle giant muscle fiber," *Biophysical journal*, vol. 35, no. 1, pp. 193–213, 1981.

[204] I. Dasanayake and J.-S. Li, "Constrained minimum-power control of spiking neuron oscillators," in *Decision and Control and European Control Conference (CDC-ECC), 2011 50th IEEE Conference on*, pp. 3694–3699, IEEE, 2011.

Vita

Walter Botongo Bomela

Degrees

B.S. Summa Cum Laude, Electrical Engineering, December 2012
M.S. Systems Science & Mathematics, August 2018
Ph.D. Electrical Engineering, August 2018

Professional Societies

IEEE Society

Publications

W. Bomela, A. Zlotnik and J.-S. Li, "A Phase Model Approach for Thermostatically Controlled Load Demand Response." *Applied Energy* 228, (2018): 667-680.

W. Bomela, I. Dasanayake, J.-S. Li , Y. Chen and I. Z. Kiss, "Optimal Phase-to-Phase Control of Chemical Oscillations through Phase Models," *Industrial & Engineering Chemistry Research* (2018).

W. Bomela and J.-S. Li, "An Iterative Method for Computing Optimal Controls for Bilinear Quadratic Tracking Problems," In *American Control Conference (ACC), 2016*, pp. 2912-2917. IEEE 2016.

W. Bomela, J. Z. Bird and V. M. Acharya, "The Performance of a Transverse Flux Magnetic Gear," in *IEEE transactions on magnetics* 50, no. 1 (2014): 1-4.

S. Paul, W. Bomela, N. Paudel and J. Z. Bird, "3-D Eddy Current Torque Modeling." *IEEE Transactions on Magnetics* 50, no. 2 (2014).

K. K. Uppalapati, W. B. Bomela, J. Z. Bird, M. D. Calvin and J. D. Wright, "Experimental Evaluation of Low-Speed Flux-Focusing Magnetic Gearboxes," *IEEE transactions on industry applications* 50, no. 6(2014): 3637-3643.

August 2018

Engineering Dynamic Structures, Bomela, Ph.D. 2018